A new spectroscopic approach to collective excitations in solids: *pump-probe quantum state tomography*

Martina Esposito

PhD dissertation

Doctoral School of Physics
XXVIII cycle
Department of Physics
University of Trieste

Trieste, Italy
January 2016

PHD CANDIDATE: **Martina Esposito**

SUPERVISOR : **Daniele Fausti**

CO-SUPERVISOR: **Fulvio Parmigiani**

SCHOOL DIRECTOR: **Paolo Camerini**

a Lena e a Salvatore

A new spectroscopic approach to collective excitations in solids: *pump-probe quantum state tomography*

Summary

In a classical description the displacement of the atoms along the vibrational eigenmodes of a crystal can be measured with unlimited precision. Conversely, in the quantum formalism positions and momenta of the atoms can be determined simultaneously only within the boundary given by the Heisenberg uncertainty principle. For this reason, in real materials, in addition to the thermal disorder, the atomic displacements are subject to fluctuations which are intrinsic to their quantum nature. Because a crystalline solid has symmetries, these vibrations can be analyzed in terms of collective modes of motion of the atoms. These modes correspond to collective excitations called *phonons*. The aim of this thesis is to study the quantum fluctuations of the atoms involved in such collective vibrations.

The motivation of studying the quantum proprieties of phonons in crystals comes from various evidences, recently reported in the literature, suggesting that quantum fluctuations of the atoms in solids may be of relevance in determining the onset of intriguing and still not completely understood material properties, such as quantum para-electricity, charge density waves, or high temperature superconductivity.

The time evolution of phonons in crystals is usually addressed in the framework of ultrafast optical spectroscopy by means of pump-probe experiments. In these experiments the phonon dynamics is driven by an intense ultrashort laser pulse (the pump), and then the collective excitation is investigated in time domain through the interaction with a weaker pulse (the probe). Unfortunately this method typically provides information only about the average position of the atoms and an intense scientific debate is on-going about the possibility to have access also to the fluctuations of such positions measured with respect to a bound level for the *shot-noise* limit (intrinsic quantum noise limit).

In this research activity a new approach to investigate quantum fluctuations of collective atomic vibrations in crystals is proposed. It combines time resolved optical spectroscopy techniques (pump and probe experiments) and quantum optics techniques (balanced homodyne detection). The novel spectroscopic tool, *pump-probe quantum state tomography*, consists in the time domain characterization of the quantum state of probing light pulses after the interaction with the photo-excited material. The approach has been tested by investigating quantum fluctuations of the atomic positions in α-quartz, which serves as a case study for transparent materials. However, it can be in principle generalized to the study any collective excitations in crystals.

Contents

Nobody said it was easy,
No one ever said it would be so hard,
I'm going back to the start...

The Scientist, Coldplay

1 Introduction

1.1 Invitation and historical remarks

Light-matter interaction belongs to our daily experience. It is the mechanism which rules our perception of colors, our feeling of the sun on the skin in a spring day outdoor, or the effects of the sunset over the sea when the air is clear.

Figure 1.1: Sunset over the sea in Trieste, Italy.

The wonder with respect to these so familiar but every time surprising natural phenomena leads myself since I was a high school student, stimulating my curiosity about the road that from Newton's experiments about colors in the 17th century brought to the modern comprehension of the light-matter interaction in the terms of quantum mechanics. Although eight years passed from my final high school exam (where I presented a short report about nature of light) and this PhD thesis, in these years of study and research, I tried to let me guide by the same wonder of

those early days.

My PhD research activity exploits light-matter interaction for studying quantum proprieties of collective atomic vibrations in solids. In particular, quantum proprieties of atoms in matter are investigated by measuring quantum proprieties of interacting light pulses. Before going to the motivation of such a study, I would like to give here a brief historical excursus citing the salient scientific achievements that led to the present theoretical and experimental knowledge of light-matter interaction. Such steps in the history of science intrigued myself since the first stage of my studies. That's why I am happy to briefly report them here in the hope of leading the reader in the research field of this thesis.

The theory formulated by Isaac Newton in the 17th century for describing light-matter interaction claimed that light was composed of a beam of particles able, for example, to bounce back upon reflection from a mirror. Later, the necessity of describing light phenomena like interference and diffraction, incompatible with the Newton's theory, led to profound investigations about the wave-like nature of the light.

Almost two centuries of research in this field culminated in a complete description of light propagation in a mean, or in the vacuum, in terms of electromagnetic radiation. This happened through what the physicists consider one of the most elegant set of equations in science, the Maxwell's equations, formulated in their whole in 1861. The theory of the electromagnetism, developed due to the introduction of the Maxwell's equations, produced a unified interpretation of a set of phenomena which were previously considered to belong to different domains: electricity, magnetism and optics[1]. A famous sentence of Richard Fayman summarizes the huge impact of such a theory on the history of mankind: "from a long view of the history of mankind there can be little doubt that the most significant event of the 19th century will be judged as Maxwell's discovery of the laws of electrodynamics"[2].

However, at the beginning of 20th century the study of blackbody radiation spectrum, which electromagnetic theory could not explain, led Max Plank to introduce for the first time the *quantization* in the energy exchange between light and matter (1900). He considered a simple model of matter as a collection of one-dimensional charged harmonic oscillators each of them oscillating rather like a weight at the end of a spring. He knew from Maxwell how exactly these charged oscillators absorb and irradiate light and he could derive the observed radiation frequency distribution only assuming a discrete energy exchange in multiples of what he called quantum of energy[3]. It was the rise of quantum mechanics.
Later, Albert Einstein, in the *annus mirabilis* 1905, with the theory for the photoelectric effect[4], proposed the quantization of the light itself, claiming that the electromagnetic field carries energy in discrete (quantized) packets, the photons.

In the successive years a scientific revolution impacted the intellectual community, leading to the comprehension of many properties of nature at the microscopic level which cannot be described with classical physics[5]. Quantum mechanics made possible amazing scientific achievements, ranging from the invention of the first transistor (1948)[6], to the development of the first laser source[7], whose countless technological applications are at the basis of our modern society. The progresses in the comprehension of light-matter interactions at the quantum level further devel-

oped with the advent of some experimental techniques able to isolate single atoms by cooling or trapping them with laser light[8], discovery awarded with the Nobel prize in 1997. Such advancements made possible the measurement and the manipulation of single photons and single atoms without destroying their quantum properties. Such experiments (Nobel prize in 2012[9]) represent the most elementary manifestations of the quantum interaction between single atoms and photons.

In this thesis, the atoms under investigation are not isolated systems but they are arranged in lattice structures, crystalline solids, which contain a number of atoms of the order of 10^{24} (Avogadro number) per cm^3.

Although arranged in crystalline structures, atoms still manifest their quantum nature, that is responsible for many intriguing material proprieties. In particular atoms in solids can generate collective excitation, *phonons*, which manifest as quantized lattice vibrations.

In this Chapter the motivations of studying quantum properties of collective excitations in solids are reported (Section 1.2), then the typical time domain techniques for the study of collective excitations are presented (Section 1.3) and an introduction is given about how these standard techniques have been broadened out in this thesis to address quantum fluctuations (Section 1.4). Finally a reading guide is provided (Section 1.5).

1.2 Motivations

The aim of this thesis is to study the quantum proprieties of coherent vibrational modes of the atoms in crystalline solids. The displacement of the atoms along the vibrational eigenmodes of a crystal can be chaotic, due to thermal disorder, or can be characterized by a precise correlation between all the atomic positions. When all the atoms in a crystal vibrate in phase, they constitute a collective excitation commonly dubbed *coherent phonon*. The motivation of studying the quantum proprieties of phonons in crystals comes from various evidences reported in literature suggesting that quantum fluctuations of the atoms in solids may be of relevance in determining the onset of intriguing and still not completely described material properties, such as quantum para-electricity, charge density waves, or high temperature superconductivity[10–17]. In the following I am going to mention two examples selected from the literature in which lattice quantum fluctuations are shown to significantly contribute to peculiar material proprieties.

In Fig 1.2 the observations of Nosawa and co-workers[11] about fluctuations of Ti atoms in $SrTiO_3$ are shown. In this work the authors perform X-rays absorbtion spectroscopy (XAS) measurements and observe quantum fluctuations of Ti atoms along the $Ti - O$ direction in presence of UV irradiation. Their results indicates the excitation of specific phononic modes, observed only in the quantum para-electric phase. Experimentally, quantum para-electricity is associated with an anomalous behaviour of the dielectric susceptibility with respect to the typical ferroelectric comportment. In this case[11], the excitation of quantum fluctuations of some specific lattice modes by UV irradiation is shown to be directly connected

to the quantum para-electric phase.

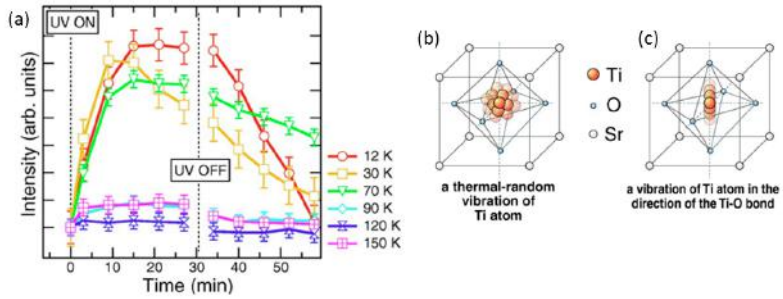

Figure 1.2: Quantum fluctuations controlled by ultraviolet irradiation in $SrTiO_3$. Figures from[11]. (a) X-rays absorbtion intensity of a specific peak in the pre-threshold Ti K-edge XAS spectra. The x axis indicates the measurement time characterized by UV irradiation started at 0 min and stopped at 30 min. The lifetime and behaviour with temperature are characteristic only of the quantum para-electric phase. (b) Schematic representation of thermal local vibrations (no UV irradiation) and (c) of vibrations excited by UV irradiation in quantum para-electric phase.

The second example regards the key role of atomic fluctuations in understating the origin of high-temperature superconductivity in copper oxide layered materials. In this framework, Newns and Tsuei demonstrated[12] that a fluctuating bound

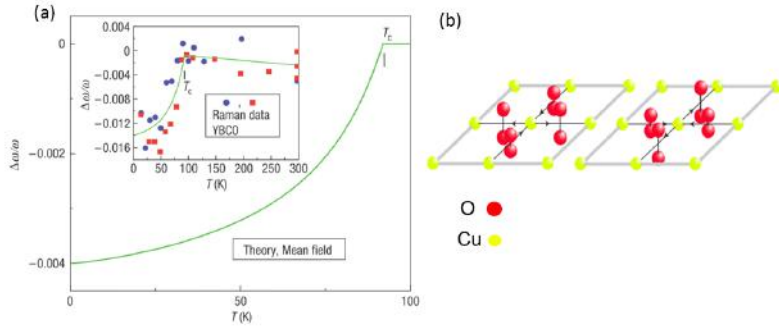

Figure 1.3: Fluctuating Cu-O-Cu bond model of high-temperature superconductivity. Figures from[12]. (a) Frequency shift of the the out-of-plain oxygen mode in cuprate superconductors derived from the fluctuating bound model. Comparison with experimental results (inset) for Raman experiments in[18]. (b) Schematic representation of the z component of the fluctuating bond field in CuO_2 planes. Cu atoms (yellow), O atoms (red).

model of high temperature superconductivity can predict many experimental observations. Their model[12] explicitly accounts for the lattice atomic fluctuations which involve the CuO_2 planes. It is characterized by a non linear coupling between the Cu-Cu bound and the in-plain and out-of-plain oxygen fluctuations. In

Fig 1.3 it is reported the result about the qualitative reproduction of the universal experimental softening of the out-of-plane oxygen-bend mode below T_C in cuprate superconductors[18–21].

The two studies reported from the literature exemplify the motivations for the investigation of the atomic collective fluctuations in solid state physics. They represent two examples in a huge range of physical settings in which the intrinsic atomic quantum fluctuations are important.

It important to note that, in addition to the the case of atomic vibrational states, the problem of the quantum fluctuations can be also generalized to excitations of different nature, like for example excitations of electronic origin[22,23].

In this framework, this thesis could be considered as a seeding work in which a new spectroscopic approach to address the quantum fluctuations of collective excitations in solids is proposed. The thesis put at test such a new approach by investigating quantum fluctuations of simple excitations, Raman active atomic vibrational modes, in simple systems, transparent materials.

In the following I am going to introduce the tools adopted here to address quantum fluctuations of lattice displacements. I will first present the typical *spectroscopic* technique for studying the time evolution of the average collective atomic vibrations in solids: ultrafast spectroscopy. Then I will introduce the novel approach developed and tested in this thesis to investigate not only the average but also the fluctuations of the atomic positions in time domain experiments.

1.3 Time domain ultrafast spectroscopy

In the research field of solid state physics, light matter-interaction is a fundamental brick since the electromagnetic radiation scattered by a material carries a huge amount of information which can be used for investigating different characteristics of the material itself. This is the basis of all spectroscopies. From a historical point of view, spectroscopy arose already after the famous experiment carried out by Isaac Newton and published in 1672 in which, refracting sunlight in a glass prism, he observed the dispersion of the colors of the rainbow, labelling this rainbow *spectrum*[24]. Solid state spectroscopy is today a wide research field that deals with the study of the interaction between matter and radiation * both at the equilibrium and out-of-the-equilibrium[25].

In equilibrium spectroscopies the external stimuli are either extremely weak or their application lasts for a time much longer than the interaction time among the

*Although, strictly speaking, the term *radiation* only deals with photons (electromagnetic radiation), it should be noted that spectroscopy, in its general meaning, also involves the interactions of other types of particles, such as neutrons, electrons, or protons, which are also used to investigate matter[24]. Even limiting the analysis to the case in which the adopted probe is the electromagnetic radiation, the research field is still vast, since in function of the energy content of the used photons, different degrees of freedom of the material can be probed. When the energy content of the electromagnetic radiation drops in what is called *optical range*, which includes the ultraviolet (UV), the visible (VIS) and the near infrared (NIR) energy regions, one speaks of optical spectroscopy.

internal degrees of freedom of the system. With the advent of ultrafast laser sources, the possibility of applying external perturbations faster than the typical relaxation times led to dramatic advances in solid state spectroscopy[26]. This achievement made possible the study of ultrafast dynamics with relatively cheap table-top lasers which can easily deliver ultrashort coherent and tunable light pulses with a typical duration ranging from a few to several hundreds of femtoseconds (10^{15} s)[27,28]. After the first experiments, awarded with the Nobel prize in 1999[29], in the last 20 years a dramatic development of the out-of-equilibrium version of most of the traditional equilibrium optical spectroscopies has been achieved[26].

In the framework of ultrafast spectroscopy, a single experiment, the so called *pump-probe* experiment, can be applied to investigate an innumerable variety of different phenomena in extremely diverse physical regimes[26]. The experiment consist in two steps: (i) the photo-excitation of the material through an intense ultrashort laser pulse (the pump) which drives the system out of equilibrium, and (ii) the time domain probing of the material through the interaction with a weaker pulse (the probe) at different instants after the pump perturbation. The intensity of the probe as a function of time is measured in order to observe how the optical proprieties of the material evolves from the excitation to the relaxation of the system. A scheme of a typical pump-probe experiment is shown in Fig 1.4.

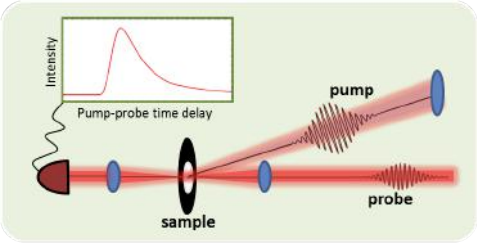

Figure 1.4: Scheme of a standard pump-probe optical experiment in transmission configuration. A photodiode measures the intensity of the transmitted probe pulses at different time delays between the pump and the probe arrivals on the sample. The intensity of the transmitted light is indicated ad the average number of photons per pulse at each time: $\langle \hat{n} \rangle (t)$.

This simple scheme can be adapted to investigate the non-equilibrium physics of solid state systems in substantially different conceptual frameworks. One of this is the study of coherent collective excitation in materials. Any kind of impulsive excitation coupled to specific collective modes, such as lattice vibrations or charge/spin order, can indeed trigger a coherent oscillation at the typical frequency of the mode and with a relaxation time that is related to its de-phasing time[26]. In this case, the pump-probe technique can be considered as a real time domain technique, since the Fourier-transform of the time domain signal provides the frequency and lifetime of the collective mode in the material.

The novel experimental approach adopted in this thesis to address quantum fluctuations in condensed matter is rooted in the framework of ultrafast spectroscopy but also exploits techniques from quantum optics. An introduction to such an approach is given in the following.

1.4 A novel approach to atomic quantum fluctuations

Although standard pump-probe technique has been largely adopted to investigate coherent vibrational modes in crystal[30], the typically measured quantity, that is the intensity of the output probe, provides information only about the average of the atomic positions during the collective excitation. It is indeed possible to follows the time evolution of the average position of the atoms, since it is linearly mapped (through the modulation of the dielectric function) into the number of probe photons scattered by the sample. Nevertheless one has no chances in this way to directly measure the quantum fluctuations of the atomic positions around their average. An intense scientific debate is indeed on-going about the possibility to measure quantum fluctuations of atomic positions in time domain with respect to a benchmark level for the *shot-noise* limit (intrinsic quantum noise limit).[31].

Here this problem is addressed starting from the consideration that in a pump-probe experiment the probing light contains much more information that just the intensity, which is measured in standard pump-probe experiments. I give here and introduction to the two experimental schemes designed and realized during my PhD research activity and that will be presented in detail in the next chapters.

- The first experimental apparatus has been designed starting from a typical pump-probe setup but adding the possibility of measuring the entire photon number quantum statistics of the scattered probing light. This experimental scheme, sketched in Fig 1.5, is based on the possibility to separately acquire each single scattered probe pulse. Working with high repetition-rate laser

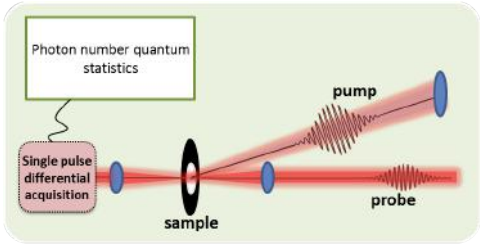

Figure 1.5: Scheme of the photon number quantum statistics experiment. For each time delay between the pump and probe, several scattered probe pulses are singularly acquired and the photon number statistics is measured.

  sources allows to have access to a wide statistics in few seconds and to be able to measure not only the average number of photons ($\langle \hat{n} \rangle (t)$), related to the average atomic positions, but also the higher photon number statistical momenta ($\langle \hat{n}^k \rangle (t)$), into which the fluctuations of the atomic positions can be mapped. In particular, by adopting a fully quantum mechanical theoretical treatment, from the fluctuations of the photon number of the scattered probe it is possible to extract information about the atomic quantum fluctuations.

- Following the same conceptual path, the second experimental apparatus includes the first one but at the same time expands its capabilities. In par-

ticular, it allows not only to investigate the photon number quantum distribution, but also to have access to the maximum information about the scattered probing light, *i. e.* its quantum state. This novel spectroscopic tool combines time resolved optical spectroscopy techniques (pump-probe experiments) and quantum optics techniques for the measurement of photon quantum states. The experimental scheme, sketched in Fig 1.6, is similar to a standard pump-probe experiment with the difference that the probe pulses, after the interaction with the system, are sent to a quantum optics experimental setup in order to study their quantum state. The method adopted for the optical quantum state reconstruction is *optical homodyne tomography*. With this experimental scheme, that we indicate as *pump-probe quantum*

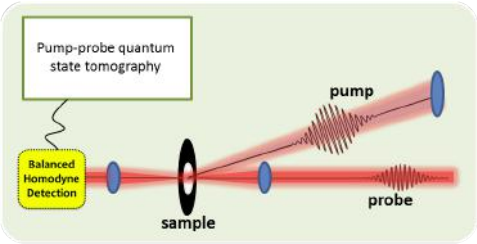

Figure 1.6: Scheme of the pump-probe quantum state tomography. For each time delay between the pump and probe, several scattered probe pulses are sent to the balance homodyne detection apparatus for the measurement of the optical quantum state at each instant.

state tomography, the quantum states of the probing light pulses are completely characterized in the time domain. The aim of this experiment is to have access to the quantum state of collective atomic vibrations in crystals through the study of the quantum states of the probing light pulses after the interaction with the material.

The proposed spectroscopic approach, which consists in the two just introduced experimental schemes, has been tested here for the study of quantum fluctuations of phonons in α-quartz which serves as a case study for transparent materials. However, it can be in principle generalized to the study of quantum proprieties of any collective excitation in solids.

1.5 Reading guide

Here I would like to contextualize the PhD research activity reported in this thesis and give some guidelines for the reading.

This research project has been carried out in the T-ReX laboratory within the Fermi project at Elettra Trieste's synchrotron facility. Some of the preliminary experiments have been performed at the LOA laboratory at ENSTA ParisTech institute in Palaiseau. The development of the technological instrumentation has been obtained in collaboration with the CAEN company. The theoretical part of

the project has been developed in close collaboration with the "open quantum systems - theory research team" at the University of Trieste. The computational part of the project saw a collaboration with the scientific computing team of the Elettra synchrotron facility. The project included the participation of several students putting into effects two master theses, one bachelor thesis and several national and international internships.

The daily comparison with all the involved persons and an intense team work constituted the motor of the project and for this reason I am convinced it is correct to adopt for the rest of the thesis a writing style with the first person plural.

A flow diagram representing the scientific purposes of the project and the different experimental approaches adopted is shown in Fig 1.7.

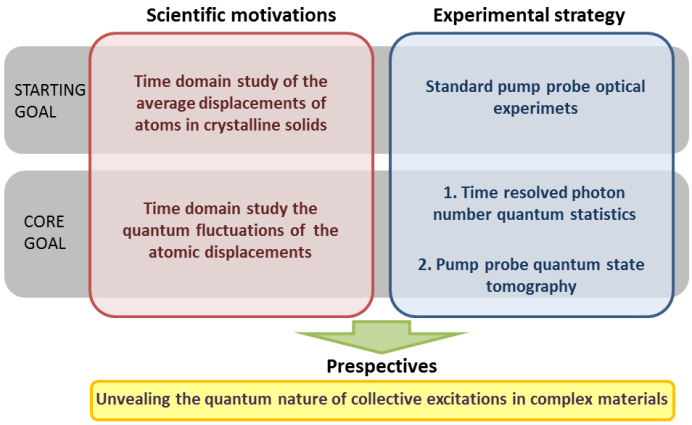

Figure 1.7: Flow diagram of the research project.

The results obtained in this three years long research activity are presented using the following scheme:

- Chapter 2 gives an introduction to the theoretical background needed for the description of photon and phonon dynamics in quantum mechanics and of their interaction. In particular, photons and phonons are described with the formalism of the quantum harmonic oscillator; the standard classical and semiclassical theoretical treatment of impulsive excitation of coherent phonons in solids are reported and finally the proposal of a fully quantum model for photon-phonon interaction in optical time domain experiments is presented.
- Chapter 3 is dedicated to the measurement of quantum states of light in pulsed regime. The optical homodyne tomography technique is described and our experimental results are reported. Our investigation about the treatment of the inefficiencies in homodyning experiments is also presented. We approached this issue both by the tomographic point of view and by the technological and experimental point of view.

- Chapter 4 reports our results about the investigation of quantum fluctuations of lattice displacements by the photon number quantum statistics approach in non-equilibrium experiments. The combination of shot-noise limited pump probe experiments and a fully quantum description of the impulsive phonon excitation in transparent materials allowed us to uncover the fluctuations in non-equilibrium lattice dynamics.
- Chapter 5 describes the pump probe quantum state tomography technique. The method has the aim to characterize, via optical homodyne tomography, the quantum state of the probing optical pulses in time domain ultrafast spectroscopy experiments. The technique has been tested by studying the dynamics of photo-excited phonons in a sample of quartz. The preliminary experimental results are reported.
- Chapter 6 reports the conclusions and the perspectives of the research project.

References

[1] C. Cohen-Tannoudji and B. Diu, F. Laloe. *Quantum Mechanics*. Wiley, Paris, 1977.

[2] Di Ari Ben-Menahem. *Historical Encyclopedia of Natural and Mathematical Sciences*. Springer, Verlag Berlin Hidelberg New York, 2009.

[3] Roy J. Glauber. Nobel lecture: One hundred years of light quanta. *Rev. Mod. Phys.*, 78:1267–1278, Nov 2006. doi: 10.1103/RevModPhys.78.1267. URL http://link.aps.org/doi/10.1103/RevModPhys.78.1267.

[4] Albert Einstein. Über einen die erzeugung und verwandlung des lichtes betreffenden heuristischen gesichtspunkt. *Annalen der Physik*, 17:6, 1905.

[5] Jhon Bell (Introduction of Alain Aspect). *Speakable and Unspeakable in Quantum Mechanics: Collected Papers on Quantum Philosophy*. Cambridge University Press (second edition), Cambridge, 2004.

[6] J. Bardeen and W. H. Brattain. The transistor, a semi-conductor triode. *Phys. Rev.*, 74:230–231, Jul 1948. doi: 10.1103/PhysRev.74.230. URL http://link.aps.org/doi/10.1103/PhysRev.74.230.

[7] T. H. Maiman. Stimulated optical radiation in ruby. *Nature*, 187:493–494, 1960.

[8] Ball Philip. Nobel prizes honour atom-trappers. *Nature*, 389:770, 1997.

[9] Ed Hinds and Rainer Blatt. Nobel 2012 physics: Manipulating individual quantum systems. *Nature*, 496:55, 2012.

[10] S. Sachdev. Quantum criticality: competing ground states in low dimensions. *Science*, 288:475–480, 2000.

[11] Iwazumi T. Nozawa, S. and H. Osawa. Direct observation of the quantum fluctuation controlled by ultraviolet irradiation in $SrTio_3$. *Phys. Rev. B*, 72: 121101, 2005.

[12] D. M. Newns and C. C. Tsuei. Fluctuating cu-o-cu bond model of high-temperature superconductivity. *Nat. Phys.*, 189:1745–2473, 2007.

[13] Cho K. Shibauchi T. Kasahara S. Mizukami Y. Katsumata R.-Tsuruhara Y. Terashima T. Ikeda H. Tanatar M. A. Kitano H. Salovich N. Giannetta R. W. Walmsley P. Carrington A. Prozorov R. Hashimoto, K. and Y. Matsuda. A sharp peak of the zero-temperature penetration depth at optimal composition in $BaFe_2(As_{1-x}P_x)_2$. *Science*, 336:1554–1557, 2012.

[14] Di Castro C. Castellani, C. and M. Grilli. Non-fermi-liquid behavior and d-wave superconductivity near the charge-density-wave quantum critical point. *Z. Phys. B: Condens. Matter*, 103:137–144, 1995.

[15] Berlinger W. Müller, K. A. and E. Tosatti. Indication for a novel phase in the quantum paraelectric regime of $SrTiO_3$. *Z. Phys. B: Condens. Matter*, 84: 277–283, 1991.

[16] Meenehan S. M. MacCabe G. S. Groblacher S. Safavi-Naeini A. H. Marsili F. Shaw M. D. Cohen, J. D. and O. Painter. Phonon counting and intensity interferometry of a nanomechanical resonator. *Nature*, 520:522–525, 2015.

[17] C. Gadermaier, A. S. Alexandrov, V. V. Kabanov, P. Kusar, T. Mertelj, X. Yao, C. Manzoni, D. Brida, G. Cerullo, and D. Mihailovic. Electron-phonon coupling in high-temperature cuprate superconductors determined from electron relaxation rates. *Phys. Rev. Lett.*, 105:257001, Dec 2010. doi: 10.1103/PhysRevLett.105.257001. URL http://link.aps.org/doi/10.1103/PhysRevLett.105.257001.

[18] K. C. Hewitt, X. K. Chen, C. Roch, J. Chrzanowski, J. C. Irwin, E. H. Altendorf, R. Liang, D. Bonn, and W. N. Hardy. Hole concentration and phonon renormalization of the $340 - cm^{-1}$ B_{1g} mode in 2% ca-doped $yba_2cu_3o_y$ (6.76&*lt*; *y*&*lt*; 7.00). *Phys. Rev. B*, 69:064514, Feb 2004. doi: 10.1103/PhysRevB.69.064514. URL http://link.aps.org/doi/10.1103/PhysRevB.69.064514.

[19] Xingjiang Zhou, M. Cardona, D. Colson, and V. Viallet. Plane oxygen vibrations and their temperature dependence in $hgba_2ca_2cu_3o_{8+\delta}$ single crystals. *Phys. Rev. B*, 55:12770–12775, May 1997. doi: 10.1103/PhysRevB.55.12770. URL http://link.aps.org/doi/10.1103/PhysRevB.55.12770.

[20] D. Reznik, B. Keimer, F. Dogan, and I. A. Aksay. q dependence of self-energy effects of the plane oxygen vibration in $yba_2cu_3o_7$. *Phys. Rev. Lett.*, 75:2396–2399, Sep 1995. doi: 10.1103/PhysRevLett.75.2396. URL http://link.aps.org/doi/10.1103/PhysRevLett.75.2396.

[21] H. Uchiyama, A. Q. R. Baron, S. Tsutsui, Y. Tanaka, W.-Z. Hu, A. Yamamoto, S. Tajima, and Y. Endoh. Softening of cu-o bond stretching phonons in tetragonal $hgba_2cuo_{4+\delta}$. *Phys. Rev. Lett.*, 92:197005, May 2004. doi: 10.1103/PhysRevLett.92.197005. URL http://link.aps.org/doi/10.1103/PhysRevLett.92.197005.

[22] Yuan Li, M. Le Tacon, M. Bakr, D. Terrade, D. Manske, R. Hackl, L. Ji, M. K. Chan, N. Barišić, X. Zhao, M. Greven, and B. Keimer. Feedback effect on high-energy magnetic fluctuations in the model high-temperature superconductor $hgba_2cuo_{4+\delta}$ observed by electronic raman scattering. *Phys. Rev. Lett.*, 108: 227003, May 2012. doi: 10.1103/PhysRevLett.108.227003. URL http://link.aps.org/doi/10.1103/PhysRevLett.108.227003.

[23] Thomas P. Devereaux and Rudi Hackl. Inelastic light scattering from correlated electrons. *Rev. Mod. Phys.*, 79:175–233, Jan 2007. doi: 10.1103/RevModPhys.79.175. URL http://link.aps.org/doi/10.1103/RevModPhys.79.175.

[24] J. Garcıa Sole, L.E. Bausa, and D. Jaque. *An Introduction to the Optical Spectroscopy of Inorganic Solids*. John Wiley and Sons Ltd, England, 2005.

[25] Hans Kuzmany. *Solid-State Spectroscopy*. Springer, Heidelberg Dordrecht London New York, 2009.

[26] Claudio Giannetti, Massimo Capone, Daniele Fausti, Michele Fabrizio, and Fulvio Parmigiani. Ultrafast optical spectroscopy of high-temperature superconductors and correlated materials: a non-equilibrium approach. 2015.

[27] R.L. Fork, B.I. Greene, and C.V. Shank. Generation of optical pulses shorter than 0.1 psec by colliding pulse mode locking. *Applied Physics Letters*, 38: 671–672, 1981.

[28] P. Kean D. Spence and W. Sibbett. 60-fsec pulse generation from a self-mode-locked ti:sapphire laser. *Opt. Lett.*, 16:42–44, 1991.

[29] Ahmed Zewail. Femtochemistry: Atomic-scale dynamics of the chemical bond using ultrafast lasers. *(Nobel Lecture), Angew. Chem., Int. Ed. Engl.*, 39:2586, 2000).

[30] R. Merlin. Generating coherent thz phonons with light pulses. *Solid State Commun.*, 102:207–220, 1997.

[31] O. V. Misochko. Nonclassical states of lattice excitations: squeezed states and entangled phonons. *Phys. Usp.*, 183:917–933, 2013.

2

Photon - Phonon interaction

The word "quantum", from the Latin for "how much", indicates a discrete and indivisible quantity of energy [1]. As photons are the quanta of the electromagnetic field, phonons are the quanta of the atomic vibrational field in matter. This thesis aims at the study of quantum fluctuations of phonons in crystals by exploiting ultrafast optical spectroscopy. The leading idea of this work is to map the fluctuations of the atomic positions into the fluctuation of the number of probing photons after the interaction with the material. In this Chapter the problem of a theoretical treatment for photon-phonon interaction in time resolved optical experiments is addressed.

2.1 Introduction

At a finite temperature the atoms that form a crystalline solid vibrate around their equilibrium positions, with an amplitude that depends on the temperature. Since in crystals the atoms are arranged in lattice with precise symmetries, these vibrations can be analyzed in terms of normal modes describing the collective motion of the atoms with specific patterns [2]. The displacement of the atoms along such vibrational eigenmodes of the crystal are characterized not only by thermal fluctuations but also by intrinsic quantum fluctuations. Indeed, even at absolute zero temperature, according to quantum mechanics, there will be zero-point vibrations [3].

In this thesis a novel approach to access the quantum fluctuations of the atomic positions in pump-probe experiments is proposed. In this kind of experiments an intense pump laser pulse drives a collective atomic excitation in the crystal and a less intense probe laser pulse interacts with the system out-of-equilibrium. We developed two experimental schemes that allow for (i) the measurement of the

photon number quantum statistics and (ii) the quantum state reconstruction of the probe pulses in a pump-probe setup. In order to predict how the fluctuations of the atomic positions in a lattice can be mapped onto the photon quantum fluctuations of the probe field, we propose a novel theoretical approach to time domain studies. This theoretical treatment describes quantum mechanically both the material and the optical fields involved in the interaction process. The model has been developed in close collaboration with the "open quantum systems - theory research team" at the University of Trieste[4].

Before going into the details of such a model it is necessary to introduce the basic tools for the quantum description of both the electromagnetic fields and the vibrational atomic fields. Both are typical examples of bosonic systems and can be modelled as quantum harmonic oscillators.

This Chapter is organized as follows,

- The theoretical background necessary for the adoption of the quantum harmonic oscillator formalism is provided (Section 2.2).
- The harmonic oscillator formalism is exploited to give an explicit description of light pulses in terms of photons and collective atomic vibrations in terms of phonons (Sections 2.3, 2.4 and 2.5).
- The photon-phonon interaction in pump probe experiments is described using two different theoretical approaches and focusing on the case of transparent materials. In particular, the first approach is the standard non-linear optical approach which, although treats both photons and phonons classically, is of fundamental importance to frame the physical context of our experiments. The second treatment consists in the standard semi-classical approach to phononic quantum states generation and describes quantum mechanically only phonons while the optical fields are treated classically (Section 2.6).
- Finally our fully quantum theoretical treatment for the description of phonon excitation and detection in transparent materials is reported (Section 2.7).

2.2 The quantum state of a physical system

"State means whatever information is required about a specific system, in addition to physical laws, in order to predict its behavior in future experiments". With this sentence Ugo Fano effectively introduces the concept of quantum state of a physical system in his review paper[5]. A brief introduction to the basic concepts necessary for the representation of a generic quantum state is now provided.

There are states, in quantum mechanics, which are characterized by the fact that the information about the system under consideration is known in the most deterministic way permitted by quantum mechanics itself[5]. Such states are called *pure states* and the information about them is encoded in a normalized vector $|\Psi\rangle$. The latter belongs to a Hilbert space $\mathcal{H}$, which contains all the possible states of that system. These vectors can be conveniently represented in one of the bases for

$\mathcal{H}$ and can therefore be expressed as a wavefunction $\Psi(t, \bar{r})$. For pure states an experiment exists, at least in principle, whose outcome is unique and predictable with certainty when performed on a system prepared in that state. A measurement of this kind is called "complete", for it provides the maximum amount possible of information about that variable of the system. In the formalism of vector states, the expectation value of an observable, identified by an Hermitian operator $\hat{O}$ acting on the Hilbert space $\mathcal{H}$ of the state, is given by

$$\langle \hat{O} \rangle = \langle \Psi | \hat{O} | \Psi \rangle = \mathrm{Tr}[\hat{O} \, |\Psi\rangle \, \langle \Psi|] \, , \tag{2.1}$$

and it suggests that a state can also be identified by the projector $|\Psi\rangle\langle\Psi|$.

However, systems also occur for which no complete experiment gives a unique outcome predictable with certainty[5]. For this reason there exist a more general description for quantum states in terms of *density matrices* acting on $\mathcal{H}$: that is by Hermitian, non-negative Hilbert-space operators of unit-trace,

$$\hat{\rho} = \sum_i \lambda_i |\Psi_i\rangle\langle\Psi_i| \tag{2.2}$$

such that

$$\sum_i \lambda_i = 1, \qquad \lambda_i > 0, \qquad \langle \Psi_i | \Psi_i \rangle = 1, \qquad \forall i. \tag{2.3}$$

The density operator formalism is necessary in order to describe *statistical ensembles* of quantum systems, which cannot be associated with a single vector in $\mathcal{H}$. A state is *pure* when $\hat{\rho}$ becomes a projector on the Hilbert-space, i.e. when there is only one coefficient λ different from zero and equal to one, otherwise it is *mixed* and describes a statistical ensemble of physical systems in states $|\Psi_i\rangle \, \langle \Psi_i|$ with weight λ_i. Note that, being (2.2) just one of the possible representations of $\hat{\rho}$, the choice of the set of $|\Psi_i\rangle$ is not unique.

The expectation value of an observable $\hat{O}$ on the state identified by $\hat{\rho}$ is given by

$$\langle \hat{O} \rangle_\rho = \mathrm{Tr}[\hat{O}\hat{\rho}] \, . \tag{2.4}$$

This last equation offers a more general definition of the density matrix, by making no reference to any particular set of pure states, as equation (2.2) instead does[6].

From the definition of the density operator in (2.2) and the Schrödinger equation

$$\frac{\partial}{\partial t} |\psi\rangle = -\frac{i}{\hbar} \hat{H} \, |\psi\rangle \, , \tag{2.5}$$

we can easily obtain the time evolution of $\hat{\rho}$

$$\begin{aligned} \frac{\partial \hat{\rho}}{\partial t} &= \sum_i \frac{\partial \, |\psi_i\rangle}{\partial t} \lambda_i \, \langle \psi_i| + \sum_i |\psi_i\rangle \, \lambda_i \frac{\partial \, \langle \psi_i|}{\partial t} \\ &= -\frac{i}{\hbar} \hat{H} \sum_i |\psi_i\rangle \, \lambda_i \, \langle \psi_i| + \frac{i}{\hbar} \sum_i |\psi_i\rangle \, \lambda_i \, \langle \psi_i| \, \hat{H} \\ &= -\frac{i}{\hbar} \left[\hat{H}, \hat{\rho}(t) \right] \end{aligned}$$

The previous relation is known as Liouville von Neumann equation[7]. In order to describe the time evolution of the density operator one can also use the matrix representation and study the time dependence of each matrix elements[8].

The task of experimentally determining the quantum state of a system consists in gathering all the information needed to perform the predictions about the future behaviour of the system (like in (2.4)). One of the techniques to retrieve the state of a system is the quantum tomography of the state, which will be discussed in more detail in Chapter 3, where the problem of the tomographic reconstruction of quantum states of light is addressed.

2.2.1 Wigner function

A useful object, which allows a direct visualization of the state of a system, is a particular transform (the Wigner transform or Weyl anti-transform) of the density matrix: the Wigner function, defined as follows

$$W_\rho(q,p) \quad = \quad \frac{1}{2\pi\hbar}\int_{\mathbb{R}} \mathrm{d}y \ \langle q+\frac{y}{2}|\ \hat{\rho}\ |q-\frac{y}{2}\rangle\ \mathrm{e}^{-i\,y\,p/\hbar}\ , \tag{2.6}$$

or symmetrically in p[9]. It is a normalized and real function in the phase-space, i.e. a space spanned by two conjugate variables, usually denoted with q and p. The Wigner function univocally characterize the quantum state, however in this respect infinite other functions satisfy this request[10]. The main advantage in representing a quantum state in terms of its Wigner function is that it behaves like a quasiprobability distribution for the state. This means that its marginal distributions, that is the integrals of the functions over the two phase-space conjugate variables, correspond to the probability densities of the state in the two variables:

$$\int_{\mathbb{R}} \mathrm{d}p\, W_\rho(q,p) \quad = \quad \langle q|\,\hat{\rho}\,|q\rangle = \big|\,\langle q|\Psi\rangle\,\big|^2, \tag{2.7}$$

$$\int_{\mathbb{R}} \mathrm{d}q\, W_\rho(q,p) \quad = \quad \langle p|\,\hat{\rho}\,|p\rangle = \big|\,\langle p|\Psi\rangle\,\big|^2, \tag{2.8}$$

where the last equality in both the expressions is valid only in the case of a pure state $\hat{\rho} = |\Psi\rangle\langle\Psi|$.
Moreover, it is possible to express the expectation values of any observable $\hat{O}$ as simple phase-space average of its Wigner transform, i.e., by taking the function

$$W_O(q,p) = \frac{1}{2\pi\hbar}\int_{\mathbb{R}} \mathrm{d}y \ \langle q+\frac{y}{2}|\ \hat{O}\ |q-\frac{y}{2}\rangle\ \mathrm{e}^{-i\,y\,p/\hbar}\ , \tag{2.9}$$

the expectation value of $\hat{O}$ will be

$$\langle\hat{O}\rangle = 2\pi\hbar\int_{\mathbb{R}} \mathrm{d}q\,\mathrm{d}p\, W_\rho(q,p)\, W_O(q,p) = \mathrm{Tr}[\hat{O}\,\hat{\rho}]. \tag{2.10}$$

This propriety derives from the so called overlap formula[11] (or trace product rule[10]) of the Wigner function, which in the case of two pure states, $\hat{\rho}_1 = |\psi_1\rangle\langle\psi_1|$ and $\hat{\rho}_2 = |\psi_2\rangle\langle\psi_2|$, reads

$$\begin{aligned} \mathrm{Tr}\left[\rho_1\rho_2\right] &= |\langle\psi_1|\psi_2\rangle|^2 \\ &= 2\pi\hbar \int_{\mathbb{R}} \mathrm{d}q \int_{\mathbb{R}} \mathrm{d}p\, W_{\rho_1}(q,p)\, W_{\rho_2}(q,p)\,. \end{aligned} \tag{2.11}$$

The latter represents the transition probability between the pure states $|\psi_1\rangle$ and $|\psi_2\rangle$. Notice that, if the two states are orthogonal their scalar product is zero. From the second line of relation (2.11) one can observe that in order to have a null integral, at least one of the two Wigner functions should assume some negative values (excluding particular cases). This possibility of assuming negative values represents one of the main differences of the Wigner function with respect to classical probability distributions[8].

The advantages of the Wigner function representation becomes evident in the treatment of the quantum harmonic oscillator.

2.3 The quantum harmonic oscillator

Both the kinds of systems which we deal with in this thesis, i.e. the modes of the electromagnetic field and the vibrational modes in condensed matter lattices, can be described as quantum harmonic oscillators.

In order to describe a system as a quantum harmonic oscillator one has to identify two variables which behaves like the conjugate position and momentum of the harmonic oscillator[6]. In the case of the vibrational field these quantities are the displacement and the linear momentum of a normal mode of the atomic lattice. In the case of the electromagnetic field, instead, they are the real and imaginary parts of the complex time-evolving electric field, also known as quadratures. In the first case the mode excitations are called **phonons**, in the second case, **photons**. Once this correspondence between the harmonic oscillator position and momentum and the associated physical quantities of the system has been identified, the procedure is a straightforward application of the standard quantization of the harmonic oscillator[12]. In the following a brief introduction to the quantum harmonic oscillator formalism is reported and some examples of typical quantum states are given.

In classical mechanics an harmonic oscillator is a system that, when displaced from its equilibrium position, experiences a restoring force which is proportional to the displacement. The classical Hamiltonian of the harmonic oscillator is

$$H = \frac{P^2}{2m} + \frac{m\omega^2}{2}Q^2, \tag{2.12}$$

where Q and P are the position and the linear momentum of an oscillator with mass m. Such a system is characterized by an oscillating motion at the specific frequency ω which identifies a so called **normal mode**. A normal mode of an generic oscillating system is a pattern of motion in which all parts of the system

move sinusoidally with the same frequency and with a fixed phase relation[13]. The concept of normal mode is very important since the most general motion of a system can be described as a superposition of its normal modes.

In quantum mechanics, given a specific mode characterized by the frequency ω, the harmonic oscillator is described starting from the bosonic creation and annihilation operators of the mode: $\hat{a}$ and $\hat{a}^\dagger$. The hamiltonian for the free oscillator is

$$\hat{H}_0 = \hbar\omega\big(\hat{a}^\dagger\hat{a} + \frac{1}{2}\big). \tag{2.13}$$

The position and momentum operators are defined as the following linear combination of $\hat{a}$ and $\hat{a}^\dagger$,

$$\hat{q} = \frac{\hat{a} + \hat{a}^\dagger}{\sqrt{2}}, \qquad \hat{p} = \frac{\hat{a} - \hat{a}^\dagger}{i\sqrt{2}}. \tag{2.14}$$

The correspondence between the just defined position and momentum operators and the position and linear momentum variables in the classical Hamiltonian in (2.12) are the following:

$$\hat{p} \to \frac{P}{\sqrt{m\hbar\omega}}, \qquad \hat{q} \to \sqrt{\frac{m\omega}{\hbar}}\, Q\ .$$

Throughout the rest of the thesis, we will use the natural units (i.e., $\hbar = 1$) and consider quantum harmonic oscillators of unity mass. With this convention, one can verify, from the bosonic commutation relations ($[\hat{a}, \hat{a}^\dagger] = 1$), that the position and momentum operators are canonically conjugated observables,

$$[\hat{q}, \hat{p}] = i, \tag{2.15}$$

and satisfy the Heisenberg uncertainty principle,

$$\Delta q \Delta p \geq \frac{1}{4}, \tag{2.16}$$

where $\Delta q = \langle \hat{q}^2 \rangle - \langle \hat{q} \rangle^2$ and $\Delta p = \langle \hat{p}^2 \rangle - \langle \hat{p} \rangle^2$ are the variances of the operators $\hat{q}$ and $\hat{p}$.

2.3.1 Examples of quantum states

The most natural states of the quantum harmonic oscillator to work with are the **Fock states** $|n\rangle$, eigenstates of the Hamiltonian $\hat{H}_0$ and therefore also of the number operator $\hat{n} = \hat{a}^\dagger\hat{a}$:

$$\hat{n}\,|n\rangle = \hat{a}^\dagger\hat{a}\,|n\rangle = n\,|n\rangle\,. \tag{2.17}$$

They are also called number states and constitute an orthonormal basis of the Hilbert space (number basis). The ground state of $\hat{H}_0$, known as **vacuum state**

$|0\rangle$, is defined by the following action of the annihilation operator,

$$\hat{a}\,|0\rangle = 0, \tag{2.18}$$

while the excited states are given by

$$|n\rangle = \frac{(\hat{a}^\dagger)^n}{\sqrt{n!}}\,|0\rangle\,. \tag{2.19}$$

The action of the creation and annihilation operators on these eigenstates of the Hamiltonian is to create of destroy a quantum of excitation in the following way:

$$\begin{aligned} \hat{a}^\dagger\,|n\rangle &= \sqrt{n+1}\,|n+1\rangle \\ \hat{a}\,|n\rangle &= \sqrt{n}\,|n-1\rangle\ . \end{aligned} \tag{2.20}$$

The Wigner function of the Fock state with $n = 1$ is shown in Fig 2.1, together

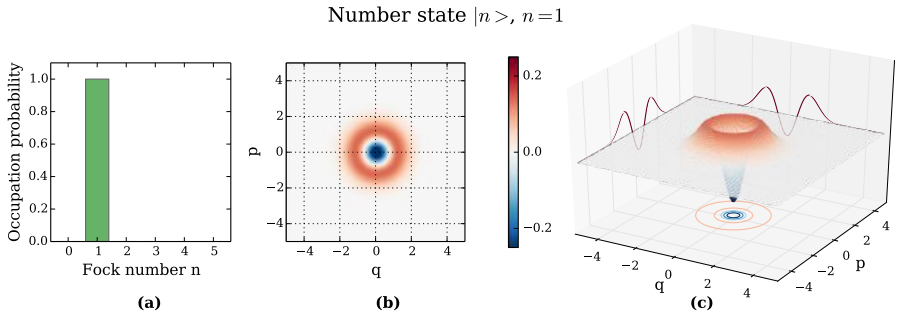

Figure 2.1: Number state $|n\rangle$ with $n = 1$. Occupation probability distribution (a). Wigner function bi-dimensional (b) and tri-dimensional (c) plot.

with its occupation probability distribution. The Fock states of the harmonic oscillator are the simpler example of states for which the Wigner function assumes also negative values. The number states describe states in which the oscillator is populated with exactly n excitations. For this states the expectation value of the position $\langle n|\,\hat{q}\,|n\rangle$ is time-independent and equals 0 whatever excited number state the oscillator is in[6]. To get a time-dependent expectation value of $\hat{q}$, a superposition of number states must be taken. Out of these non-number states of the harmonic oscillator the commonest are coherent states, which are the closest analogue to classical coherent oscillations.

Coherent states are defined as eigenstates of the annihilation operator:

$$\hat{a}\,|\alpha\rangle = \alpha\,|\alpha\rangle\,, \tag{2.21}$$

where $\alpha \in \mathbb{C}$, because $\hat{a}$ is not Hermitian. The vacuum state is a special case of coherent state, since it satisfies (2.21) with $\alpha = 0$. The Wigner function of the vacuum state and that of a coherent state with $\alpha = 2$ are shown in Fig 2.2 and Fig 2.3 respectively. An important propriety of vacuum and coherent states is

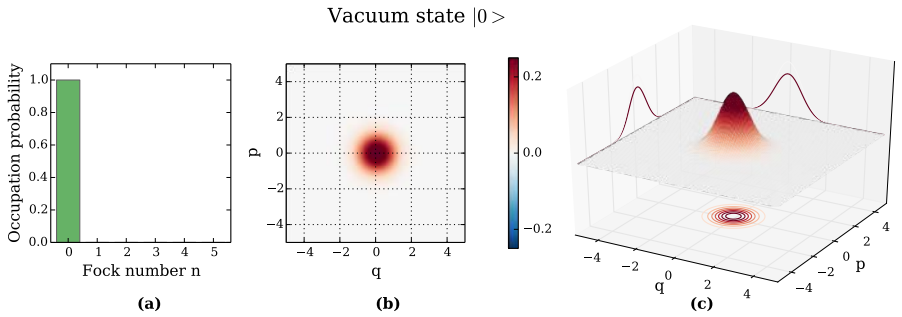

Figure 2.2: Vacuum state $|0\rangle$. Occupation probability distribution (a). Wigner function bi-dimensional (b) and tri-dimensional (c) plot.

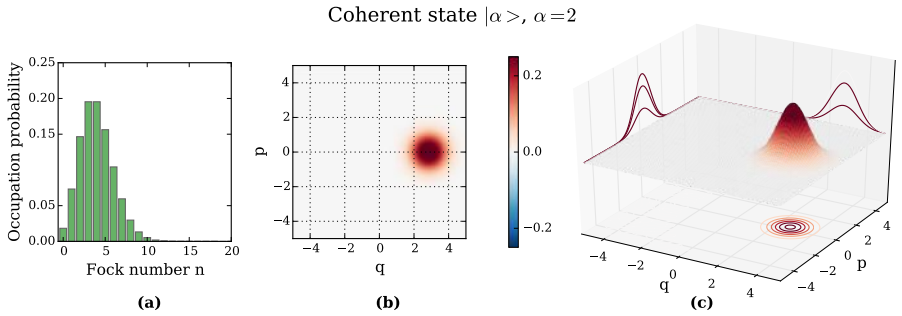

Figure 2.3: Coherent state $|\alpha\rangle$ with $\alpha = 2$. Occupation probability distribution (a). Wigner function bi-dimensional (b) and tri-dimensional (c) plot.

that a they are minimum uncertainty states, so that the equality sign in equation (2.16) holds, as the uncertainties in the two conjugate variables results to be equal ($\Delta q = \Delta p = \frac{1}{2}$). Moreover the occupation probability, i.e. the probability $p(m)$ of the state $|\alpha\rangle$ to be populated with m excitations, is given by a Poisson distribution,

$$p(m) = |\langle m|\alpha\rangle|^2 = \langle m|\alpha\rangle \langle \alpha|m\rangle = \frac{e^{-\langle \hat{n}\rangle} \langle \hat{n}\rangle^m}{m!}. \tag{2.22}$$

The expectation value of the number operator on a coherent state is $\langle \hat{n}\rangle = \langle \alpha|\hat{a}^\dagger \hat{a}|\alpha\rangle = |\alpha|^2$. A generic coherent state can be also written starting from the vacuum in the following way:

$$|\alpha\rangle = D(\alpha)\,|0\rangle\,, \tag{2.23}$$

where

$$D(\alpha) = \exp(\alpha \hat{a}^\dagger - \alpha^* \hat{a}) \tag{2.24}$$

is the *displacement operator*. The term displacement describes the action of this operator on the Wigner function of the vacuum state. Coherent states can be also written in the number basis[14] as

$$|\alpha\rangle = e^{-\frac{|\alpha|^2}{2}} \sum_{n=0}^{\infty} \frac{\alpha^n}{\sqrt{n!}} |n\rangle\,. \tag{2.25}$$

In this states the expectation value of the position $\langle \alpha|\,\hat{q}\,|\alpha\rangle$ with $\alpha \neq 0$ is time dependent and oscillates at frequency ω. The time dependence of the expectation values of $\hat{q}$ and $\hat{p}$ can be calculated starting from the coherent state's definition and the expression of $\hat{q}$ and $\hat{p}$ as a function of the mode operators. However, the Wigner phase space approach provides a more intuitive way to visualize the evolution of a state. In fact, the time evolution operator of $\hat{H}_0$ rotates the Wigner function around the origin of the plane, analogously to the classical case, in which a harmonic oscillator is described by a rotating vector in phase space[6].

The vacuum and the coherent states satisfy the equality in the uncertainty relation in (2.16) in the most simple way possible, namely with both Δq and Δp equal to 1/2. However, the Heisenberg relation does not make any request to the distribution of the observables taken singularly but only to the product of the variances of two conjugated observables. The fluctuations in one of the two can be therefore reduced (or squeezed) at the price of the increasing of the fluctuation width of its conjugate. States that display such noise properties are called **squeezed states**. The term squeezed generally refers just to the unbalance in the noise between the two observables, which can exist also for states that do not saturate the uncertainty relation, such as thermal ones. In order to specify the case in which one of the uncertainties falls below the vacuum limit (i.e. the Heisenberg relation is saturated) one generally refers to *vacuum squeezed state*. Such a state can be defined starting from the vacuum in the following way:

$$S(\xi)\,|0\rangle\,, \tag{2.26}$$

where

$$S(\xi) = \exp[\frac{1}{2}(\xi \hat{a}^{\dagger 2} - \xi^* \hat{a}^2)] \tag{2.27}$$

is the *squeezing operator* with $\xi = re^{i\psi} \in \mathbb{C}$ the squeezing parameter. An example of Wigner function associated with such a state is shown in Fig 2.4. In Fig 2.5 is shown a displaced - squeezed state.

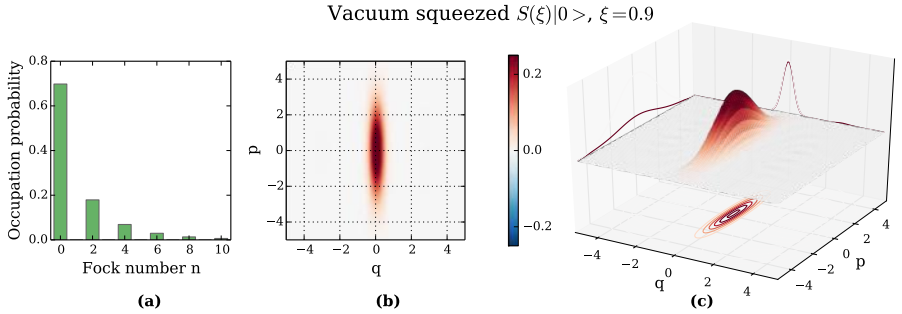

Figure 2.4: Vacuum squeezed state $S(\xi)\,|0\rangle$, with $\xi = 0.9$. Occupation probability distribution (a). Wigner function bi-dimensional (b) and tri-dimensional (c) plot.

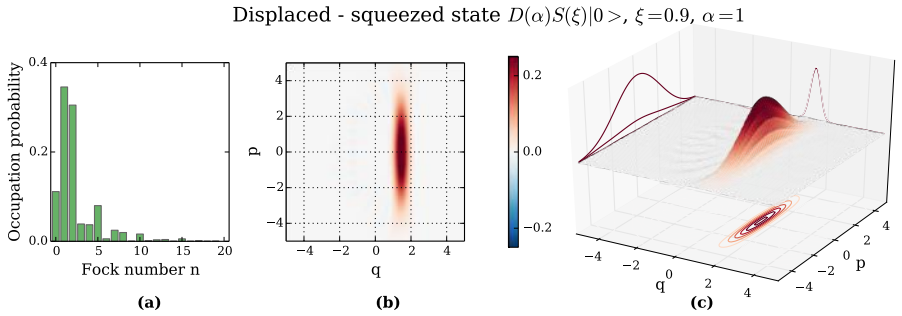

Figure 2.5: Displaced squeezed state $D(\alpha)S(\xi)\,|0\rangle$, with $\xi = 0.9$ and $\alpha = 1$. Occupation probability distribution (a). Wigner function bi-dimensional (b) and tri-dimensional (c) plot.

An other important example among the quantum harmonic oscillator states are **thermal states**. They are states of the harmonic oscillator which present a thermal boson population. This means that the mean number excitations which populates the state is given by

$$\langle \hat{n} \rangle = \frac{1}{e^{\beta\omega} - 1} \ . \tag{2.28}$$

These states describe a harmonic oscillator at equilibrium at a temperature T. The inverse temperature β is defined as $\beta = 1/k_B T$, with k_B the Boltzmann constant.

The density matrix of such a state can be written as

$$\hat{\rho}_\beta = \frac{e^{-\beta\omega\hat{a}^\dagger\hat{a}}}{\mathrm{Tr}[e^{-\beta\omega\hat{a}^\dagger\hat{a}}]} \ . \tag{2.29}$$

Indicating with N the mean number of bosons in the thermal state (equation (2.28)), the density matrix in (2.29) can be expressed as follows,

$$\hat{\rho}_\beta(N) = \frac{1}{(1+N)} \sum_{n=0}^{\infty} \left(\frac{N}{1+N}\right)^n |n\rangle\langle n| \ . \tag{2.30}$$

The thermal state Wigner function is a Gaussian function centred on the origin of the phase space, as the one of the vacuum state. An example of Wigner function of a thermal state is given in Fig 2.6. It is a Gaussian function centered in the origin of the phase space as for the vacuum state, However, one can easily notice that a thermal Wigner function is broader than a vacuum one. Moreover, in the case of the vacuum state, the number of bosons in the harmonic oscillator is zero, while for the thermal state it is given by equation 2.28. A broad quasiprobability distribution means also a larger variance, and hence, noise, in the measurement of $\hat{q}$ and $\hat{p}$. In particular, the higher the temperature, the larger the noise.

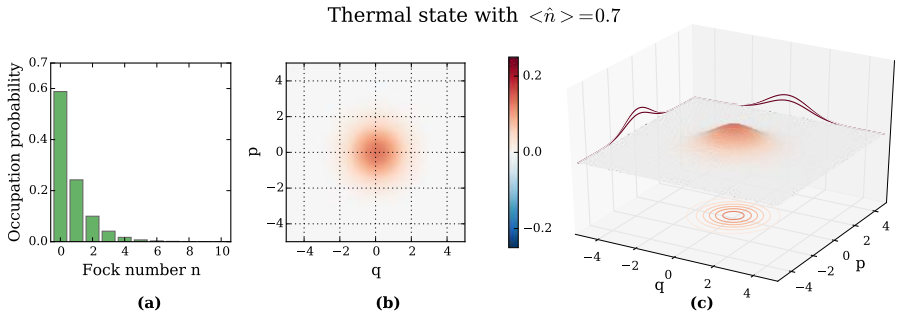

Figure 2.6: Thermal state $\hat{\rho}_\beta$, with $\langle n\rangle = 0.7$. Occupation probability distribution (a). Wigner function bi-dimensional (b) and tri-dimensional (c) plot.

Let us consider the case of the vibrational modes in crystals. There the atomic oscillations have energies such that the thermal population of the mode is usually relevant even at room temperature. In particular, being the energies of phonons very small (tens of millielectronvolts), the vibrational modes are thermally populated even at room temperature. Therefore, phonon modes at equilibrium must generally be described with thermal states. For the electromagnetic modes instead one usually works with photon energies much higher than the room temperature energy ($k_B T = 25\,\mathrm{meV}$), and thus, the thermal photon population of the mode is often negligible[6].

Acting on a thermal state with a displacement operator produces a displaced thermal state. Despite the term "thermal", such a state does not describe a system at equilibrium with its surroundings at a given temperature. As for a coherent

state, in a displaced thermal state the operators $\hat{q}$ and $\hat{p}$ have oscillating expectation values. Their variance, instead, is larger than the one for a coherent state and is determined by the original temperature of the "undisplaced" state. In the same way, squeezed thermal states can also occur, which have the phase-dependent variance characteristic of squeezed states. These states of the harmonic oscillator are all characterized by Gaussian Wigner functions and for this reason they belong to the class of the so called **Gaussian states**. The most general single mode Gaussian state can be given by:

$$\hat{\rho}_{\text{Gauss}}(\alpha, \xi, N) = D(\alpha)\, S(\xi)\, \hat{\rho}_\beta(N)\, S^\dagger(\xi)\, D^\dagger(\alpha), \tag{2.31}$$

where $D(\alpha)$ is the displacement operator defined in equation (2.24), $S(\xi)$ the squeezing operator in equation (2.27) and N the mean number of bosons in the thermal state (equation (2.30)). For example, if $\xi = 0$ and $N = 0$, the Gaussian state (2.31) is reduced to a coherent state (2.25) $\hat{\rho} = |\alpha\rangle\langle\alpha|$, which is the vacuum for $\alpha = 0$; while, for $\alpha = 0$, $N = 0$ and $\xi \neq 0$ one obtains the squeezed vacuum. The Gaussian states can be theoretically dealt with in a standard way. Indeed, it is possible to define two quantities, the first-moments vector $\hat{\mathbf{R}} = (\hat{q}, \hat{p})^T$ and the covariance matrix $\boldsymbol{\sigma}$, that fully characterize such states[15]. The covariance matrix elements are given by:

$$[\boldsymbol{\sigma}]_{kj} = \frac{1}{2}\langle\{\hat{R}_k, \hat{R}_j\}\rangle - \langle\hat{R}_j\rangle\langle\hat{R}_k\rangle\,, \tag{2.32}$$

where $\{\hat{A}, \hat{B}\} = \hat{A}\hat{B} + \hat{B}\hat{A}$ is the anticommutator between two operators and $\langle\hat{A}\rangle = \mathrm{Tr}[\hat{\rho}\hat{A}]$ the expectation value of the operator $\hat{A}$ on the state $\hat{\rho}$. The explicit expression for the covariance matrix for a generic quantum state is the following,

$$\boldsymbol{\sigma} = \begin{pmatrix} \langle\hat{q}^2\rangle - \langle\hat{q}\rangle^2 & \frac{1}{2}\langle\hat{q}\hat{p} + \hat{p}\hat{q}\rangle - \langle\hat{q}\rangle\langle\hat{p}\rangle \\ \frac{1}{2}\langle\hat{q}\hat{p} + \hat{p}\hat{q}\rangle - \langle\hat{q}\rangle\langle\hat{p}\rangle & \langle\hat{p}^2\rangle - \langle\hat{p}\rangle^2 \end{pmatrix}\,. \tag{2.33}$$

For the specific case of Gaussian states, equation (2.31), with displacement parameter $\alpha = ae^{i\phi}$, squeezing parameter $\xi = re^{i\psi}$ and thermal parameter N, the covariance matrix elements can be expressed with the following general form:

$$\sigma_{kk} = \frac{1+2N}{2}[\cosh(2r) - (-1)^k \sinh(2r)\cos\psi], \qquad (k = 1, 2)$$

$$\sigma_{12} = \sigma_{21} = \frac{1+2N}{2}\sinh(2r)\sin\psi, \tag{2.34}$$

while the first-moments vector is given by:

$$\langle\hat{\mathbf{R}}\rangle = \sqrt{2}(\Re e[\alpha], \Im m[\alpha])^T = \sqrt{2}(a\cos\phi, a\sin\phi)^T. \tag{2.35}$$

With this notation, one can easily write the Wigner function of a generic single

mode Gaussian state (2.31):

$$W_{\rho_{\text{Gauss}}}(\mathbf{X}) = \frac{\exp\{-\frac{1}{2}(\mathbf{X} - \langle\hat{\mathbf{R}}\rangle)^T \boldsymbol{\sigma}^{-1}(\mathbf{X} - \langle\hat{\mathbf{R}}\rangle)\}}{\pi\sqrt{\det[\boldsymbol{\sigma}]}}, \tag{2.36}$$

where $\mathbf{X} = (q, p)^T \in \mathbb{R}^2$.

Gaussian states are the typical phonon and photon states we deal with in our experiments. Moreover, some of the interactions of a harmonic oscillator in a Gaussian state with external degrees of freedom can be described as simple transformations within the class of gaussian states. The interactions that fall into this category are said to preserve the gaussianity of the state[6].

2.3.2 Lowest order interactions for the harmonic oscillator

In the framework of the time evolution of quantum states of the harmonic oscillator, those interactions which preserve the gaussianity of the state are associated with interaction Hamiltonians which are linear or, at most, bilinear in the mode operators $\hat{a}_k$ and $\hat{a}_k^\dagger$ [15] (the index k indicate a specific mode of the harmonic oscillator). Considering the general case in which many different modes are involved, the most general linear and bilinear interaction Hamiltonian has the form:

$$\hat{H}_{\text{int}} = \underbrace{\Big[\sum_k \lambda\, \hat{a}_k^\dagger + h.c.\Big]}_{\text{displacement}} + \underbrace{\Big[\sum_{k,l} \beta\, \hat{a}_k^\dagger \hat{a}_l + h.c.\Big]}_{\text{2 modes mixing}} + \underbrace{\Big[\sum_{k,l} \gamma\, \hat{a}_k^\dagger \hat{a}_l^\dagger + h.c.\Big]}_{\text{1 and 2 modes squeezing}}, \tag{2.37}$$

where $h.c.$ indicates the hermitian conjugate. In equation (2.37) one can easily identify three distinct components which are commented in the following.

1. The linear part contains terms like $(\hat{a}_k + \hat{a}_k^\dagger)$. Each of these terms corresponds to an evolution operator totally similar to the displacement operator defined in (2.24), which acting on the vacuum generates a coherent state in the mode k.

2. The second block contains terms of the form $(\hat{a}_k^\dagger \hat{a}_l + h.c.)$. Each of these terms describes an interaction that involves linear mixing of two modes, like for example the interaction between two optical modes due to a beam splitter.

3. Finally the last block contains terms like $[(a_k^\dagger)^2 + h.c.]$ and $[\hat{a}_k^\dagger \hat{a}_l^\dagger + h.c.]$. In this case the degenerate form gives rise to an evolution operator totally similar to the squeezing operator defined in (2.27), which acting on the vacuum generates a vacuum squeezed state in the mode k. In the non degenerate case, the associated evolution operator corresponds to the so-called two-modes squeezing operator which can be expressed as

$$S_2(\xi) = \exp[\frac{1}{2}(\xi \hat{a}_k^\dagger \hat{a}_l^\dagger - \xi^* \hat{a}_k \hat{a}_l)]. \tag{2.38}$$

These considerations are particulary relevant for investigating the interaction processes that occurs in time resolved experiments in which phononic quantum states are created.

In the following we describe first the laser pulses in terms of photons, then the collective atomic excitations in crystals in terms of phonons and finally the photon-phonon interaction problem is addressed.

2.4 Multimode laser pulses, photons

A single mode of the electromagnetic radiation, *i. e.* an electromagnetic field characterized by a precise frequency, polarization and propagation direction, can be described with the quantum harmonic oscillator formalism by adopting a suitable electromagnetic field quantization approach[16]. In particular one can demonstrate that the conjugate operators $\hat{q}$ and $\hat{p}$ defined in (2.14) are associated with the electric field operator in the following way,

$$\hat{E}_x(z,t) = E_0 \left[\cos(\omega t)\,\hat{q} + \sin(\omega t)\,\hat{p}\right] \sin(kz), \tag{2.39}$$

where E_0 has the dimensions of an electric field and we assumed here the single mode electric field to be polarized along the x-direction and to propagate along the z-direction with frequency ω and wavevector k. The position and momentum operators of the quantum harmonic oscillator are indeed associated with the real and the imaginary part of the electric field. Photons arise as the quanta of the electromagnetic energy, such that the Fock states, defined in (2.17) as eigenstates of the single mode Hamiltonian, correspond to the presence of a precisely defined number of photons[17].

The totally coherent light generated by an ideal monochromatic laser source is however not associated to a defined number of photons but it is characterized by a Poisson photon statistics. Thus, the quantum states associated with such a laser light are coherent states, introduced in (2.21).

For pulsed laser sources, as the ones used for the experiments in this thesis, the reasoning is the same with the difference that this kind of sources cannot be approximated as monochromatic, since the short duration of the pulse in time is necessarily followed by a certain broadening in frequency due to the contribution of several active modes of the laser cavity. Classically, the electric field of a mode-locked pulsed laser beam can be represented as a superposition of amplitudes:

$$E(t) = \sum_{j=-J}^{J} |\alpha_j|\, e^{i\omega_j t}\,, \qquad \omega_j = \omega_0 + \Phi_j, \tag{2.40}$$

where ω_0 is the laser central frequency and the phases Φ_j are mode-locked by the condition $\Phi_j = j\delta$ with δ a constant depending on the repetition rate of the laser. The total number of contributing modes $(2J+1)$ is given by the ratio between the laser cavity length and the pulse duration. Typically for a meter long laser cavity producing a train of 100fs pulses, there are about 10^4 contributing optical modes.

Quantized pulsed laser light is described by associating to each monochromatic component a coherent state $|\alpha_j\rangle$, that is an eigenstate of the annihilation operator $\hat{a}_j$ of photons in the mode of frequency ω_j, $\hat{a}_j |\alpha_j\rangle = \alpha_j |\alpha_j\rangle$, and to the entire pulse the tensor product

$$|\bar{\alpha}\rangle = \bigotimes_{l=-J}^{J} |\alpha_j\rangle \,, \tag{2.41}$$

where $\bar{\alpha}$ is the vector whose components are the amplitudes α_j. By means of the creation and annihilation operators $\hat{a}_j$ and $\hat{a}_j^\dagger$ each monochromatic coherent state reads

$$|\alpha_j\rangle = D(\alpha_j)\,|0\rangle \;\;, \qquad D(\alpha_j) = e^{\alpha_j \hat{a}_j^\dagger - \alpha_j^* \hat{a}_j} \;\;, \tag{2.42}$$

where $|0\rangle$ is the vacuum state and $D(\alpha)$ is the displacement operator defined in (2.24). Since the creation and annihilation operators that pertain to different modes commute, the pulsed coherent state in (2.41) can be conveniently recast as

$$|\bar{\alpha}\rangle = D(\bar{\alpha})\,|0\rangle \;\;, \qquad D(\bar{\alpha}) = e^{\hat{A}^\dagger(\bar{\alpha}) - \hat{A}(\bar{\alpha})} \;\;, \tag{2.43}$$

by mean of a displacement operator $D(\bar{\alpha})$ expressed in terms of multi-mode operators

$$\hat{A}^\dagger(\bar{\alpha}) = \sum_j \alpha_j \, \hat{a}_j^\dagger \;\;, \qquad \hat{A}(\bar{\alpha}) = \sum_j \alpha_j^* \hat{a}_j \;\;. \tag{2.44}$$

The reason for labeling the pulsed coherent state by $|\bar{\alpha}\rangle$ can now be easily understood. The state of one photon of frequency ω_j is given by $\hat{a}_j^\dagger |0\rangle = |1_j\rangle$, while a generic non-monochromatic superposition of frequencies ω_j with amplitudes α_j corresponds to the state $|1_{\bar{\alpha}}\rangle = \sum_j \alpha_j |1_j\rangle$ that results from applying the multimode operator $\hat{A}^\dagger(\bar{\alpha})$ to the vacuum state:

$$\hat{A}^\dagger(\bar{\alpha})\,|0\rangle = \sum_j \alpha_j \, \hat{a}_j^\dagger \,|0\rangle = \sum_j \alpha_j \;|1_j\rangle = |1_{\bar{\alpha}}\rangle \;\;. \tag{2.45}$$

Therefore, $\hat{A}^\dagger(\bar{\alpha})$ is the creator operator of a single photon in the (not normalized) superposition state $|1_{\bar{\alpha}}\rangle$, while $\hat{A}(\bar{\alpha})$ destroys a photon in the same state; thus, the quantum state of the pulsed laser is a coherent state associated not with a single amplitude α_j, but with the vector $\bar{\alpha}$ of all the amplitudes contributing to the pulse: in other words, we have a Poissonian distribution not with respect to the number of photons in a monochromatic wave, but to the number of photons in the superposition $|1_{\bar{\alpha}}\rangle$.
The normalized operators are defined as follows

$$\hat{A} = \frac{\hat{A}(\bar{\alpha})}{|\bar{\alpha}|} \;\;, \qquad \hat{A}^\dagger = \frac{\hat{A}(\bar{\alpha})}{|\bar{\alpha}|} \;\;, \tag{2.46}$$

where $|\bar{\alpha}|^2 = \langle 1_{\bar{\alpha}} | 1_{\bar{\alpha}} \rangle$, and satisfy the canonical commutation relations

$$\left[\hat{A}, \hat{A}^\dagger\right] = \frac{1}{|\bar{\alpha}|^2} \sum_{ij} \alpha_i^* \alpha_j \left[\hat{a}_i, \hat{a}_j^\dagger\right] = 1 \ . \tag{2.47}$$

2.5 Collective atomic excitations, phonons

The quantum harmonic oscillator formalism not only applies to electromagnetic waves, but also to collective atomic vibrations in a lattice.

The concept of "collective excitation" allows to describe a huge number of interacting particles with a relatively simple approach. As the concept of "quasi-particles" allows the description of the electronic motion in metals through the Sommerfeld-Bloch theory [18] (overcoming the problem of solving Schrödinger's equation for $\sim 10^{23}$ interacting electrons), the concept of "collective excitation" allows to easily treat a system of many particles which move coherently. Phonons are collective excitations corresponding to the coherent motion of all the atoms in a crystalline solid [2].

In crystalline solids the atoms are arranged in regular three-dimensional periodic lattices such that in $1\,\mathrm{cm}^3$ there is a number of atoms of the order of 10^{23} (Avogadro number) [2]. The lattice atomic composition and the geometry of the crystal determine the frequency and the symmetry of the normal modes of the system, *i. e.* the collective atomic vibrational modes.

Let us consider for example a simple one-dimensional crystal consisting in a linear lattice with two different types of atoms per unit cell with an harmonic interaction between nearest neighbors. This model can be considered as the prototype of a crystal with more than one atom per unit cell. A sketch of such a system is given in Fig 2.7, m_1 and m_2 are the masses of the two atomic species and K is the constant associated to the harmonic interaction. In the equilibrium configuration, we assume that the atoms of mass m_1 occupy the sublattice positions na, while the atoms of mass m_2 occupy the sublattice positions $na + d$. We denote by u_n and v_n the two variables associated to the displacement of the two atomic species from the equilibrium position.

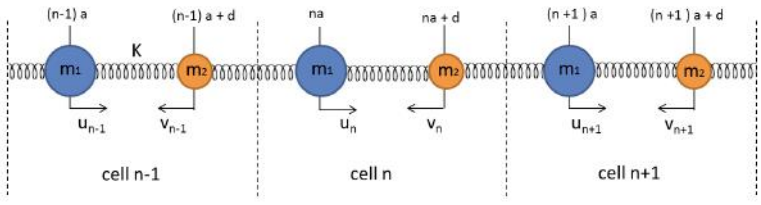

Figure 2.7: Linear chain with 2 atoms per unit cell with mass m_1 and m_2 and nearest neighbors interaction. The atoms are shown in the equilibrium positions, the displacement u_n and v_n at a given instant are indicated with arrows.

The classical equations of motion for u_n and v_n are:

$$\begin{aligned} m_1\ddot{u}_n &= -K[(v_n - u_n) + (v_n - u_{n+1})] \\ m_1\ddot{v}_n &= -K[(u_n - v_n) + (u_n - v_{n-1})], \end{aligned} \tag{2.48}$$

and the solutions are of the form,

$$\begin{aligned} u_n &= ue^{i(qna-\omega t)} \\ v_n &= ve^{i(qna-\omega t)}. \end{aligned} \tag{2.49}$$

By substituting (2.49) into (2.48) one can easily find the following relation for the frequency dispersion in the reciprocal space[19,20],

$$\omega_{\pm}^2 = K\Big(\frac{1}{m_1} + \frac{1}{m_2}\Big) \pm K\sqrt{\Big(\frac{1}{m_1} + \frac{1}{m_2}\Big)^2 - \frac{4\sin^2(qa/2)}{m_1 m_2}}\,. \tag{2.50}$$

The two resulting ω vs. q curves are referred to as the two *branches* of the phonon dispersion relation[20,21] and are shown in Fig 2.8.

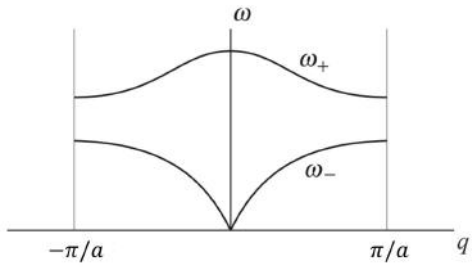

Figure 2.8: Dispersion relation for the diatomic linear chain. The upper branch is the optical branch, the lower branch is the acoustic branch[19].

Any vibrational mode of the lattice is associated with a specific branch of the dispersion relation and with a specific point in the reciprocal space. Going back to the quantum harmonic oscillator formalism, each specific vibrational mode can be described as a single mode of the harmonic oscillator (Section 2.3). Thus, the Hamiltonian for the entire harmonic lattice in the most general three dimensional case takes the form,

$$\hat{H}_{\mathrm{L}} = \sum_{\mathbf{q},\mathrm{m}} \hbar\omega_{\mathbf{q},\mathrm{m}}\big(\hat{b}^{\dagger}_{\mathbf{q}\mathrm{m}}\hat{b}_{\mathbf{q},\mathrm{m}} + \frac{1}{2}\big), \tag{2.51}$$

where $\mathbf{q}$ is the lattice quasi-momentum (in the one-dimensional case $-\pi/a < q < \pi/a$; in general $\mathbf{q}$ lies in the first Brillouin zone), and m indicates the mode index, that is the dispersion branch the phonon is associated with. In particular, the mode index will denote acoustic or optical branches and the corresponding polarization for the three dimensional case: one longitudinal, two transverse modes[19]. Note

that we indicated with $\hat{b}^{\dagger}_{\mathbf{q},\mathrm{m}}$ and $\hat{b}_{\mathbf{q},\mathrm{m}}$ the creation and a annihilation operators of the quantum harmonic oscillator associated with each single phononic mode. Thus, the general boson commutation relations are:

$$\left[\hat{b}_{\mathbf{q}',\mathrm{m}'}\,,\,\hat{b}^{\dagger}_{\mathbf{q},\mathrm{m}}\right] = \delta_{\mathbf{q}\mathbf{q}'}\delta_{mm'}\ . \tag{2.52}$$

In the quantum formalism, a generic atomic displacement from the equilibrium position $\mathbf{R}_n$ will assume the following form,

$$\hat{u}_n \propto \hat{Q}^{\mathrm{m}}_{\mathbf{q}}\, e^{i\mathbf{q}\cdot\mathbf{R}_n}\ , \tag{2.53}$$

where $\hat{Q}^{\mathrm{m}}_{\mathbf{q}}$ is the single mode amplitude operator[22],

$$\hat{Q}^{\mathrm{m}}_{\mathbf{q}} = \hat{b}_{\mathbf{q},\mathrm{m}} + \hat{b}^{\dagger}_{-\mathbf{q},\mathrm{m}}\ . \tag{2.54}$$

Notice that the operator in (2.53) contains essential information on the lattice dynamics and is the phonon analog of the electric field in the photon case[22].

In the following, collective atomic modes in crystals are addressed in the framework of ultrafast spectroscopy. We first report the typically adopted semi-classical treatments for phononic excitations in time domain experiments, and we finally present our fully quantum mechanical model for impulsive phonon excitation in transparent materials.

2.6 Impulsive excitation and detection of phonon states

The possibility to impulsively generate phononic quantum states has been largely investigated from both the experimental and the theoretical point of view[22–38].

The physical mechanism for the generation of collective vibrational modes via the interaction with ultrashort optical laser pulses depends mostly on the optical proprieties of the material under investigation. The main distinction is from transparent and opaque materials. In the first case, the phonon excitation happens through a direct coupling between the electromagnetic field and the atomic dipoles in the material[39]. In the second case, an important role is instead played by the electronic carries: they are photo-excited by the impulsive electromagnetic field and the consequent change in the electronic energy distribution mediates the phononic excitation, giving rise in this case to an indirect coupling between the electromagnetic field and the excited vibrational field[40].

In this thesis we focus on the case of transparent materials. The project strategy is indeed to test our novel experimental approach for the case of well characterized systems, in which the photon-phonon interaction can be modelled in the simplest way. For this reason we study here atomic quantum fluctuations of phonons in transparent materials with the future prospective to generalize the method also to more complex absorbing systems.

This section concerns the standard theoretical descriptions of impulsive phonon states generation in transparent materials via pump-probe experiments. It is di-

vided in two parts.

- Firstly, both the excitation and the detection process are described using the formalism of non linear optics in which the light is treated as a classical field and the material response is modelled through the non-linear susceptibility tensors. Although this is a totally classical description, it allows to clarify the basic aspects which are addressed in our fully quantum treatment.
- Secondly we present the standard semiclassical approach to quantum phonon states generation. In this case the phononic field is treated quantum mechanically while the light is treated classically. This means that this method have no access to the quantum proprieties of the light scattered by the material.

In this thesis we use an experimental approach to investigate the quantum nature of light in a pump-probe experiment. In this section, it will be evident that the classical and semiclassical presented models would be not completely descriptive of our experiments. This is the motivation that brought us to develop a fully quantum model for impulsive phonon generation and detection in pump probe experiments. This model is presented in the last section of the Chapter.

2.6.1 Impulsive Stimulated Raman scattering

In transparent materials, the phonon excitation by ultrafast optical spectroscopy is a non-resonant process in which the energy of the light is not enough to allow real electronic transitions. The mechanism which excites the phonons is the Impulsive Stimulated Raman Scattering (ISRS) which is a non linear process and belongs to the wide category of Raman scattering processes. The term Raman scattering is historically associated with the inelastic scattering of light by optical phonons in solids and molecular vibrations[41]. In a typical Raman scattering process an electromagnetic field impinges on the sample stimulating a vibrational mode such that the energy difference between the incident and the scattered optical field matches the energy of the activated lattice vibrational mode. The energy and momentum conservation relations in the quantum mechanical treatment are,

$$\hbar\omega_i = \hbar\omega_s \pm \hbar\Omega \,, \tag{2.55}$$

$$\hbar\mathbf{k}_i = \hbar\mathbf{k}_s \pm \hbar\mathbf{q} \,, \tag{2.56}$$

where the indices i and s indicate the incident and the scattered optical field, while Ω and $\mathbf{q}$ are the frequency and quasi-momentum of the phonon[42]. If a phononic mode is generated (sing +) the process is called Stokes, while if it is absorbed (sing -) the process is called anti-Stokes. A scheme of the conservation relations in a Stoke Raman scattering process is reported in Fig 2.9.

ISRS is a particular case of Raman scattering in which the excitation mechanism of the collective lattice vibrations is due to a non linear interaction with three ultrashort laser pulses. In general, the response of a medium to the interaction with an electromagnetic field consists in a polarization density due to the redistribution of the inner electric dipoles. If the optical perturbation is weak, the polarization is assumed to depend linearly on the electric field of the interacting

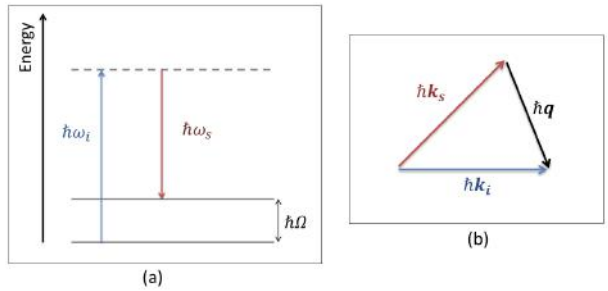

Figure 2.9: Stokes Raman scattering scheme. Energy (a) and momentum (b) conservation relations.

electromagnetic wave, $\mathbf{P} = \epsilon_0 \chi \mathbf{E}$, where ϵ_0 is the vacuum dielectric constant and χ is the electric susceptibility of the material. However, if the electromagnetic field is intense enough, also non-linear contributions to the polarization of the system must be considered[43],

$$\mathbf{P}^{\mathrm{NL}} = \mathbf{P}^{(1)} + \mathbf{P}^{(2)} + \mathbf{P}^{(3)} + ...$$

The non linear response of the medium depends also on the direction in which the optical fields are applied. In particular, the Cartesian components of the non-linear polarization are given by

$$\begin{aligned} P_i^{\mathrm{NL}}(\omega) = \epsilon_0 \Big\{ & \sum_j \chi_{ij}^{(1)} \left[E_1(\omega_1)\right]_j \\ & + \sum_{jkl} \chi_{ijk}^{(2)} \left[E_1(\omega_1)\right]_j \left[E_2(\omega_2)\right]_k \\ & + \sum_{jkl} \chi_{ijkl}^{(3)} \left[E_1(\omega_1)\right]_j \left[E_2(\omega_2)\right]_k \left[E_3(\omega_3)\right]_l + ... \Big\}, \end{aligned} \tag{2.57}$$

where the nth order susceptibility $\chi^{(n)}$ is a $(n+1)$-rank tensor and the indexes i, j, k, l can vary between the Cartesian axes x, y, z. Usually it is convenient to define these axes so that they coincide with the principal symmetry axes of the crystal.

In particular, ISRS is a non linear processes due to the induced polarization of the third order, which is the lowest non linear order in centrosymmetric crystals. In detail, the third order susceptibility tensor $\chi^{(3)}$ connects the induced polarization $P^{(3)}$ to three incoming fields, $E_1(\omega_1)$, $E_2(\omega_2)$ and $E_3(\omega_3)$[44], and the interaction results in a (fourth) scattered beam, called emitted field ($E_{\mathrm{EF}}(\omega)$). The latter contains the information on the excitation driven in the system.

Since four optical field are involved, the general phenomenon is called *four-wave mixing*[43] (a simplified scheme is shown in Fig 2.10) and ISRS is one the processes that belong to this category. In conventional two pulses (pump and probe)

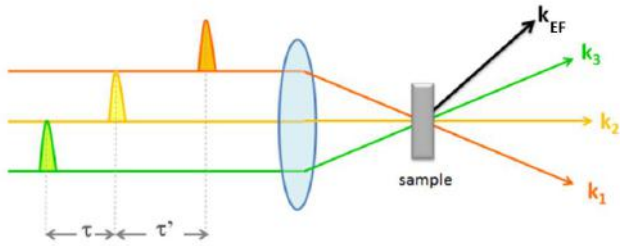

Figure 2.10: Simplified scheme of a four wave mixing process. Three optical pulses interact with the material, in the most general case at different times, and the emitted field is produced.

experiments, the fields $E_2(\omega_2)$ and $E_3(\omega_3)$ are two different frequency components of the pump laser pulse. In particular, all photon pairs such that $\omega_3 - \omega_2 = \Omega$, where Ω is the frequency of the Raman active vibrational mode, contribute to ISRS[45]. In Fig 2.11 this configuration is sketched. Since the pulse duration is

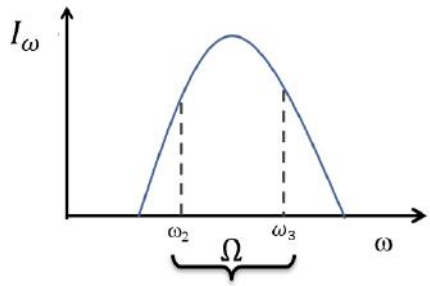

Figure 2.11: Pump pulse frequency envelope. Example of a pair of frequency components which contribute to ISRS.

less than the vibrational period, the spectral bandwidth of the pulse necessarily exceeds the vibrational frequency so that many frequency components are available to play the roles of ω_1 and ω_2[46]. Finally, interaction of the probe field $E_1(\omega_1)$ with the photo-excited material induces an emitted field, $E_{\mathrm{EF}}(\omega)$ which depends on the pump-probe delay and carries information about the specific Raman mode excited in the crystal.

2.6.2 Semiclassical models for phonon quantum states generation

Several semiclassical models describe the possibility of generating "classical" (coherent states) and non classical vibrational states, like squeezed states, by photo-excitation. In particular, for transparent materials, the most commonly used approach is to adopt Raman tensor models where the interaction between photons and phonons is not mediated by dipole allowed electronic transitions. In this conditions, interactions linear in the phonon operators allow for the generation of coherent vibrational states, while high order interactions are required for the generation of non classical states like squeezed states. The first theoretical works in this direction have been developed in the 1990s by Hu and Nori[22,25,28,39]. Here we report the basic procedure adopted in these semiclassical models.

Generally, the Hamiltonian for the coupling of a dipole (which in our case is the solid's polarization) is in the following form:

$$\hat{H} = -P_\mu \, E_\mu \ , \tag{2.58}$$

where we indicated with P_μ the polarization induced by the electric field E_μ. In the specific case of stimulated Raman scattering, as we reported previously, we deal with a non-linear polarization of the third order:

$$P_\mu^{(3)} = \epsilon_0 \, \chi^{(3)}_{\mu,\alpha\beta\gamma} \, E_\alpha E_\beta E_\gamma, \tag{2.59}$$

where $\chi^{(3)}$ is the 3-rd order susceptibility and ϵ_0 the vacuum dielectric constant. The interaction Hamiltonian is therefore

$$\hat{H} = \epsilon_0 \, \chi^{(3)}_{\mu,\alpha\beta\gamma} \, E_\alpha E_\beta E_\gamma E_\mu. \tag{2.60}$$

We can now expand the susceptibility $\chi^{(3)}_{\mu,\alpha\beta\gamma}$ in powers of the atomic displacement amplitude $\hat{Q}^{\mathrm{m}}_{\mathbf{q}}$ defined in (2.54). If we focus on a specific phononic dispersion branch m we can drop the branch superscript,

$$\hat{Q}_{\mathbf{q}} = \hat{b}_{\mathbf{q}} + \hat{b}^\dagger_{-\mathbf{q}}. \tag{2.61}$$

Let us now analyze separately the first and the second order contribution in $\hat{Q}_{\mathbf{q}}$.

- Taking the first order term, the Hamiltonian has the form

  $$\hat{H}_1 \propto \hat{Q}_{\mathbf{q}} \, E_\alpha E_\beta E_\gamma E_\mu \tag{2.62}$$

  where only the mode at momentum $\mathbf{q} = 0$ is involved. We can write the hamiltonian in (2.62) using the generic expression,

  $$\hat{H}_1 = \lambda(t) \, \hat{b}^\dagger_{\mathbf{q}} + \lambda^*(t) \, \hat{b}_{\mathbf{q}}, \tag{2.63}$$

  where $\lambda(t)$ contains the electric fields and other proportionality terms. It can be shown that in the limit of impulsive interaction, that is the case in

which the time dependence can be written as

$$\lambda(t) = l\,\delta(t)\ , \tag{2.64}$$

the time evolution operator associated with $\hat{H}_1$ becomes

$$\hat{U}_1(t) = \underbrace{\exp\Big[\Lambda(t)\,\hat{b}^\dagger_{\mathbf{q}} - \Lambda^*(t)\,\hat{b}_{\mathbf{q}}\Big]}, \qquad \Lambda(t) = -i\,lt\ . \tag{2.65}$$

One can easily notice that the highlighted block has the form of the displacement operator $D[\Lambda(t)]$ (defined in (2.24)) with the displacement parameter $\Lambda(t)$. Thus, *starting from the vacuum state, the interaction Hamiltonian in the first order in the atomic displacement generates a coherent phonon state.*

- Considering now the second-order terms of the susceptibility expansion in $\hat{Q}$ we obtain,

$$\hat{H}_2 \propto \hat{Q}_{\mathbf{q}}\,\hat{Q}_{-\mathbf{q}}\,E_\alpha E_\beta E_\gamma E_\mu\ , \tag{2.66}$$

where we took only the modes at momenta $+\mathbf{q}$ and $-\mathbf{q}$ to contribute. Equation (2.66) can be written in a more compact way as

$$\hat{H}_2 = Z(t)\,\hat{Q}_{\mathbf{q}}\hat{Q}_{-\mathbf{q}}, \tag{2.67}$$

where Z(t) contains the electric fields and the proportionality terms. Therefore, the bilinear interaction Hamiltonian of the modes $+\mathbf{q}$ and $-\mathbf{q}$ becomes

$$\begin{aligned}\hat{H}_2 &= Z(t)\left(\hat{b}_{\mathbf{q}} + \hat{b}^\dagger_{-\mathbf{q}}\right)\left(\hat{b}_{-\mathbf{q}} + \hat{b}^\dagger_{\mathbf{q}}\right)\\ &= Z(t)\left(\hat{b}^\dagger_{\mathbf{q}}\hat{b}_{\mathbf{q}} + \hat{b}^\dagger_{-\mathbf{q}}\hat{b}_{-\mathbf{q}} + 1\right) + \underbrace{Z(t)\left(\hat{b}^\dagger_{\mathbf{q}}\hat{b}^\dagger_{-\mathbf{q}} + \hat{b}_{\mathbf{q}}\hat{b}_{-\mathbf{q}}\right)}.\end{aligned} \tag{2.68}$$

In this case, the underlined term is of the kind needed to produce the a phonon squeezed state (Section 2.3.2). Going, again, to the impulsive case, i.e. the situation in which

$$Z(t) = z\,\delta(t), \tag{2.69}$$

the evolution operator $\hat{U}_2(t)$ is[28]

$$\hat{U}_2(t) = \exp\Big[-izt\,(\hat{b}^\dagger_{\mathbf{q}}\hat{b}_{\mathbf{q}} + \hat{b}^\dagger_{-\mathbf{q}}\hat{b}_{-\mathbf{q}})\Big]\underbrace{\exp\Big[\frac{1}{2}\big(\xi\,\hat{b}^\dagger_{\mathbf{q}}\hat{b}^\dagger_{-\mathbf{q}} - \xi^*\,\hat{b}_{\mathbf{q}}\hat{b}_{-\mathbf{q}}\big)\Big]}_{\hat{S}_2(\xi)}\ . \tag{2.70}$$

Therefore, impulsive second-order Raman scattering produces a two-mode squeezed state due to the squeezing operator $\hat{S}_2[\xi(t)]$ with a squeezing parameter

$$\xi(t) = 2ize^{-iz}\,t.$$

Summarizing, in this kind of semiclassical models, the optical fields are treated classically and incorporated in the parameter associated to the impulsive interaction ($\delta(t)$), while the vibrational field are treated quantum mechanically. This

allows to predict the generation of non classical phonon states when second order Raman processes are in play.

One should note that also for absorbing material several models of vibrational quantum states generation have been proposed. In materials with allowed dipole transitions, as in presence of excitons, different models based on electron-phonon coupling Hamiltonians exist[33,34]. Even these models mainly adopt semiclassical approaches where the optical fields are described classically[47], and therefore are unable to reproduce the quantum proprieties of the probe optical field that can be measured with the kind of experiment presented in this thesis. Morover such semiclassical approaches describes only the phonon generation and not the detection. These motivations stimulated us to develop a fully quantum mechanical model for ISRS description in pump probe experiments.

2.7 A fully quantum treatment

Here we report about our fully quantum model. It is based on the semiclassical approach but it allows also the quantum description of the optical fields involved in the ISRS process.

The key aspect of our model is to study both generation and detection of phonon states using a fully quantum formalism through an effective photon-phonon interaction, which is descriptive of pump-probe experiments in transparent systems[4]. Here we adopt the general convention, in which the operators $\hat{a}^\dagger$ and $\hat{a}$ refer to the modes of the electromagnetic field, while $\hat{b}^\dagger$ and $\hat{b}$ refer to the vibrational ones.

Both the pump process and the probe process are described by photon-phonon interaction Hamiltonian which is treated here in the simplified form

$$\begin{aligned}\mathcal{H} = \sum_{j,j'=-J}^{J} \Big[& \; g^1_{j,j'}\,\mu_{\mathrm{d}}\big(\hat{a}^\dagger_{xj}\,\hat{a}_{yj'}\,\hat{b}^\dagger + \hat{a}_{xj}\,\hat{a}^\dagger_{yj'}\,\hat{b}\big) \\ & + \; g^2_{j,j'}\,\mu_{\mathrm{s}}\big(\hat{a}^\dagger_{xj}\,\hat{a}_{yj'}\,(\hat{b}^\dagger)^2 + \hat{a}_{xj}\,\hat{a}^\dagger_{yj'}\,\hat{b}^2\big)\Big]\,, \end{aligned} \tag{2.71}$$

where μ_{d} and μ_{s} are coupling constants, $2J+1$ is the total number of modes within a mode-locked optical pulse, and the functions $g^\ell_{j,j'}$ take into account the relations between the frequencies of the involved fields,

$$g^\ell_{j,j'} = \begin{cases} 1 & \text{if } j' = j + \frac{\ell\Omega}{\delta} \\ 0 & \text{elsewhere,} \end{cases} \qquad \ell = 1, 2\ .$$

The Hamiltonian includes two photon modes, indicated with the subscript x and y, and one phonon mode at $\mathbf{q} = 0$. The two photon modes will model, in the pumping process, the two pump fields, and in the probing process, the probe and the emitted field. It should be noted that while the linear term involves only the creation of a phonon in a single mode at null momentum $\mathbf{q}$, the quartic term are in principle not limited to $\mathbf{q} = 0$ and one should integrate over the entire

optical phonon dispersion including processes where the momentum conservation is guaranteed by the creation of optical phonons with opposite momenta[48,49]. In our effective Hamiltonian we include only a single phonon mode at $\mathbf{q} = 0$. This assumption is made in view of the fact that, in the performed experiments, the probing process is limited to the linear regime so that phonons at $\mathbf{q} \neq 0$ will not affect the probe quantum fluctuations.

The proposed effective fully quantum mechanical approach to ISRS is descriptive of all the experimental phases: the pump process, the subsequent dissipative, irreversible phonon dynamics and the probe process, all of them treated by quantum dynamical maps[4]. Here we describe all the phases step by step.

Pump process

Before being hit by the pump laser beam the state of the relevant phonon mode at frequency Ω is appropriately taken to be a thermal state at inverse temperature β

$$\hat{\rho}_\beta = \left(1 - \mathrm{e}^{-\beta\Omega}\right) \mathrm{e}^{-\beta\Omega\,\hat{b}^\dagger\hat{b}} \ . \tag{2.72}$$

The pump laser beam is instead described by photons in a multi-mode coherent state $|\bar{\nu}\rangle\langle\bar{\nu}|$.

The Hamiltonian in (2.71) generates an impulsive change of the initial photon-phonon state $|\bar{\nu}\rangle\langle\bar{\nu}| \otimes \hat{\rho}_\beta$ given by

$$\hat{\rho}^{\bar{\nu}} = \mathcal{U}\left(|\bar{\nu}\rangle\langle\bar{\nu}| \otimes \hat{\rho}_\beta\right)\mathcal{U}^\dagger = |\bar{\nu}\rangle\langle\bar{\nu}| \otimes \mathcal{U}_{\bar{\nu}}\,\hat{\rho}_\beta\,\mathcal{U}_{\bar{\nu}}^\dagger \ , \tag{2.73}$$

where, because of the high intensity of the pump laser beam, we have adopted the mean field approximation and substituted the photon annihilation and creation operators by the scalar amplitudes ν and ν^* and replaced $\mathcal{U}$ with

$$\mathcal{U}_{\bar{\nu}} = \exp\{-i[c_1\,\hat{b}^\dagger + c_1^*\,\hat{b} + c_2\,(\hat{b}^\dagger)^2 + c_2^*\,\hat{b}^2]\} \tag{2.74}$$

$$c_1 = \mu_{\mathrm{d}} \sum_{j,j'=-J}^{J} g^1_{j,j'}\,\nu^*_{xj}\,\nu_{yj'} \tag{2.75}$$

$$c_2 = \mu_{\mathrm{s}} \sum_{j,j'=-J}^{J} g^2_{j,j'}\,\nu^*_{xj}\,\nu_{yj'} \ . \tag{2.76}$$

The pump thus prepares the relevant phonon degree of freedom in a state $\hat{\rho}^{\bar{\nu}}_{\mathrm{II}}$ which is obtained from $\hat{\rho}^{\bar{\nu}}$ by tracing over the photon degrees of freedom:

$$\hat{\rho}^{\bar{\nu}}_{\mathrm{II}} = \mathrm{Tr}_{\mathrm{I}}(\,\hat{\rho}^{\bar{\nu}}) = \mathcal{U}_{\bar{\nu}}\,\hat{\rho}_\beta\,\mathcal{U}_{\bar{\nu}}^\dagger \ , \tag{2.77}$$

where II and I refer to the phonon and photon system, respectively.

As it has been shown in the previous section, the linear contribution in the phonon operators is responsible for the displacement of $\hat{b}$ and $\hat{b}^\dagger$, while the quadratic one accounts for their multiplication by hyperbolic functions and thus for the pos-

sible squeezing of the corresponding phonon quantum state[16]:

$$\mathcal{U}_{\bar{\nu}}^{\dagger}\begin{pmatrix}\hat{b}\\ \hat{b}^{\dagger}\end{pmatrix}\mathcal{U}_{\bar{\nu}}=\mathbf{S}\begin{pmatrix}\hat{b}\\ \hat{b}^{\dagger}\end{pmatrix}+\frac{1}{2|c_2|^2}(\mathbf{S}-1)\begin{pmatrix}c_1^{*}c_2\\ c_1c_2^{*}\end{pmatrix} \tag{2.78}$$

$$\mathbf{S}=\begin{pmatrix}\cosh(2|c_2|) & -\mathrm{e}^{i(\phi+\frac{\pi}{2})}\sinh(2|c_2|)\\ -\mathrm{e}^{-i(\phi+\frac{\pi}{2})}\sinh(2|c_2|) & \cosh(2|c_2|)\end{pmatrix}, \tag{2.79}$$

where $c_2 = |c_2|\mathrm{e}^{i\phi}$. In order to write the squeezing matrix $\mathbf{S}$ in the standard formalism[16], we can define for convenience a complex squeezing parameter

$$\xi = r\mathrm{e}^{i\psi}, \tag{2.80}$$

where

$$r = 2|c_2| = 2\,|\mu_{\mathrm{s}}|\sum_{j,j'=-J}^{J} g_{j,j'}^{2}\,\nu_{xj}^{*}\,\nu_{yj'}, \qquad \text{and} \qquad \psi=\phi+\frac{\pi}{2}. \tag{2.81}$$

Notice that the squeezing parameter amplitude r depends linearly on the intensity of the pump pulse and on the squeezing coupling constant μ_{s} which weights the non linear term in the interaction Hamiltonian and models the material properties involved in the process.

The variance of the quadrature operator $\hat{B}=\frac{\hat{b}+\hat{b}^{\dagger}}{\sqrt{2}}$ with respect to the state $\hat{\rho}_{\mathrm{II}}^{\bar{\nu}}$ is given by

$$\begin{aligned}\Delta^2_{\hat{\rho}_{\mathrm{II}}^{\bar{\nu}}}\hat{B} &= \mathrm{Tr}_{\mathrm{II}}\left(\hat{\rho}_{\mathrm{II}}^{\bar{\nu}}\hat{B}^2\right)-\left(\mathrm{Tr}_{\mathrm{II}}\left(\hat{\rho}_{\mathrm{II}}^{\bar{\nu}}\hat{B}\right)\right)^2\\ &= \frac{1}{2}\coth\left(\frac{\beta\Omega}{2}\right)\left[\cosh(2r)-\sinh(2r)\cos\psi\right]\ .\end{aligned} \tag{2.82}$$

Then, for $\psi = 0$ and r large enough, one can make $\Delta^2_{\hat{\rho}_{\mathrm{II}}^{\bar{\nu}}}\hat{B}$ smaller than $1/2$ which is the shot noise variance of $\hat{B}$ with respect to the vacuum state $|0\rangle$ such that $\hat{b}|0\rangle = 0$.

Notice that up to this point the model is similar to the semiclassical ones, since, considering the high intensity of the pump fields, they has been treated classically. We indeed replace $\hat{a}$ with ν and $\hat{a}^{\dagger}$ with ν^{*} for both pump modes involved in equation (2.71).

Phonon dynamics

The photoexcited phonon state $\hat{\rho}_{\mathrm{II}}^{\bar{\nu}}$ then undergoes a dissipative dynamics that effectively takes into account the interaction of the phonons with their environment until, after a delay time τ, the target is hit by the probe laser beam. The phonon dynamics is considered to be that of an open quantum system in weak interaction with a large heat bath that will eventually drive the time-evolving phonon density matrix $\hat{\rho}_{\mathrm{II}}^{\bar{\nu}}(t) = \hat{\rho}_{\mathrm{b}}(t)$ to a thermal state $\hat{\rho}_{\beta'}$ at temperature T' larger than that of the pre-pump phonon state: $\beta' \leq \beta$. Such a relaxation process is described by a master

equation[7,50] for the phonon density matrix $\hat{\rho}_{\rm b}(t)$ of the form $\partial_t\hat{\rho}_{\rm b}(t) = \mathbb{L}[\hat{\rho}_{\rm b}(t)]$, where the generator of the time evolution is given by

$$\begin{aligned}\mathbb{L}[\hat{\rho}_{\rm b}(t)] &= -i\Big[\Omega\,\hat{b}^\dagger\hat{b}\,,\,\hat{\rho}_{\rm b}(t)\Big] \\ &+ \lambda\,(1+n')\left(\hat{b}\,\hat{\rho}_{\rm b}(t)\,\hat{b}^\dagger - \frac{1}{2}\Big\{\hat{b}^\dagger\hat{b}\,,\,\hat{\rho}_{\rm b}(t)\Big\}\right) \\ &+ \lambda\,n'\left(\hat{b}^\dagger\,\hat{\rho}_{\rm b}(t)\,\hat{b} - \frac{1}{2}\Big\{\hat{b}\hat{b}^\dagger\,,\,\hat{\rho}_{\rm b}(t)\Big\}\right), \end{aligned} \tag{2.83}$$

where $n' = \dfrac{1}{{\rm e}^{\beta'\Omega}-1}$ ($> n = \frac{1}{{\rm e}^{\beta\Omega}-1}$), while λ is a coupling constant sufficiently small so that the non-negligible presence of the environment can nonetheless be accounted for, in the so-called weak-coupling limit regime[50], by a master equation of the above type.

The first term of $\mathbb{L}$ generates the rotation in time of the phonon mode phase at its own eigenfrequency. The second two contributions consist of a so-called noise term $\hat{b}\,\hat{\rho}_{\rm b}(t)\,\hat{b}^\dagger$, respectively $\hat{b}^\dagger\,\hat{\rho}_{\rm b}(t)\,\hat{b}$ that has the property of transforming pure states into mixed states and of a dissipative term $-\frac{1}{2}\Big\{\hat{b}^\dagger\hat{b}\,,\,\hat{\rho}_{\rm b}(t)\Big\}$, respectively $-\frac{1}{2}\Big\{\hat{b}\hat{b}^\dagger\,,\,\hat{\rho}_{\rm b}(t)\Big\}$. These terms counterbalance the noise by keeping the trace of the time-evolving state $\hat{\rho}_{\rm b}(t)$, and thus the overall probability, constant in time. The anti-commutators can be incorporated into the Hamiltonian as anti-Hermitian contributions responsible for exponential time relaxation. The structure of $\mathbb{L}$ is such that the generated time-evolution maps, formally $\gamma_t = \exp(t\mathbb{L})$, compose as a forward-in-time semigroup: $\gamma_t\circ\gamma_s = \gamma_s\circ\gamma_t = \gamma_{t+s}$ for all $s,t\geq 0$. Moreover, $\hat{\rho}_{\rm b}(t) = \gamma_t[\hat{\rho}_{\rm b}]$ can be explicitly computed for any initial phonon state $\hat{\rho}_{\rm b}$; all initial states are eventually driven to a unique invariant state satisfying $\mathbb{L}[\hat{\rho}_{\rm b}] = 0$ that is given by the thermal state $\hat{\rho}_{\beta'}$.

Probe process

Finally, the probe process is again described by the Hamiltonian in equation (2.71). However, the corresponding impulsive unitary operator $\mathcal{U} = \exp(-i\mathcal{H})$ now acts on a photon-phonon state of the form $|\bar{\alpha}\rangle\langle\bar{\alpha}|\otimes\hat{\rho}^{\bar{\nu}}_{\rm II}(\tau)$. Here, $|\bar{\alpha}\rangle\langle\bar{\alpha}|$ is the multi-mode coherent state associated with the probe laser beam which contains x and y modes and is much less intense than the pump one, while $\hat{\rho}^{\bar{\nu}}_{\rm II}(\tau)$ is the phonon state dissipatively evolved up to the delay time τ between pump and probe. Differently from the pump process, the lower probe intensity allows one to neglect in $\mathcal{H}$ the quartic terms responsible for the squeezing effects. Moreover, we can apply the mean field approximation only to the field operators in the x mode which is associated to the unscattered probe, since this probe component is much more intense than the mode y, which is scattered by the phonon (emitted field). Then, by replacing $\hat{a}_{xj}$ and $\hat{a}^\dagger_{xj}$ by α_{xj} and α^*_{xj} the probe process is described by

$$\mathcal{U}_{\bar{\alpha}'} = \exp\{-i\|\bar{\alpha}'\|\big(\hat{A}(\bar{\alpha}')\,\hat{b}^\dagger + \hat{A}^\dagger(\bar{\alpha}')\,\hat{b}\big)\}\,, \tag{2.84}$$

where $\hat{A}(\bar{\alpha}')$ is the collective photon annihilation operator

$$\hat{A}(\bar{\alpha}') = \frac{1}{\|\bar{\alpha}'\|} \sum_{j=-J}^{J} (\alpha'_j)^* \, \hat{a}_{yj} \ , \quad \alpha'_j = \mu_{\rm d} \sum_{j'=-J}^{J} g^1_{j',j} \, \alpha_{xj} \ . \tag{2.85}$$

Then, the probe process affects an initial state $|\bar{\alpha}_y\rangle \langle\bar{\alpha}_y| \otimes \hat{\rho}^{\bar{\nu}}_{\rm II}(\tau)$, where $|\bar{\alpha}_y\rangle = |\alpha_{y\,-J}\rangle \otimes \cdots \otimes |\alpha_{y\,J}\rangle$ is the coherent state involving only the y polarization components such that $\hat{a}_{yj} |\bar{\alpha}_y\rangle = \alpha_{yj} |\bar{\alpha}_y\rangle$.
Notice that, unlike in (2.73), $\mathcal{U}_{\bar{\alpha}'}$ acts on the photon-phonon state as a whole and transforms it into

$$\mathcal{U}_{\bar{\alpha}'} \ |\bar{\alpha}_y\rangle \langle\bar{\alpha}_y| \otimes \hat{\rho}^{\nu}_{\rm II}(\tau) \mathcal{U}^{\dagger}_{\bar{\alpha}'} \ . \tag{2.86}$$

This allows for the quantum features of the phonon state and of its dynamics to be transcribed onto the emitted photon state

$$\hat{\rho}_{\rm I}(\tau) = {\rm Tr}_{\rm II} \left(\mathcal{U}_{\bar{\alpha}'} \ |\bar{\alpha}_y\rangle \langle\bar{\alpha}_y| \otimes \hat{\rho}^{\nu}_{\rm II}(\tau) \mathcal{U}^{\dagger}_{\bar{\alpha}'} \right) \ . \tag{2.87}$$

Unlike in the semi-classical theoretical approaches to pump and probe experiments attempted so far, one can here confront the experimental data not only with the scattered probe beam intensity, namely with the mean photon number $\langle \hat{N}_y \rangle_\tau$, where $\hat{N}_y = \hat{A}^\dagger(\bar{\alpha}')\hat{A}(\bar{\alpha}')$ and

$$\langle \hat{N}_y \rangle_\tau = {\rm Tr} \left(\hat{N}_y \, \hat{\rho}_{\rm I}(\tau) \right) \ , \tag{2.88}$$

but also for example with its variance $\Delta^2_\tau \hat{N}_y = \langle \hat{N}^2_y \rangle_\tau - \langle \hat{N}_y \rangle^2_\tau$, and in principle with any observable of the emitted optical field.

We adopted such a model to describe the photon number statistics experiments reported in Chapter 4.

References

[1] A. Messiah. *Quantum mechanics*. Dover pubbilactions, Mineola, New York, 1999.

[2] E. Kaxiras. *Atomic and electronic structure of solids*. Cambridge University Press, Cambridge, 2003.

[3] J. Patterson and Bailey B. *Solid state physics*. Springer, 2007.

[4] K. Titimbo. Creation and detection of squeezed phonons in pump and probe experiments: a fully quantum treatment, 2015.

[5] U. Fano. Description of states in quantum mechanics by density matrix and operator techniques. *Reviews of Modern Physics*, 29(1):74, 1957. Sec. 6.

[6] F. Randi. Pulsed homodyne detection for quantum state reconstruction applied to ultrafast non-equilibrium spectroscopy, 2013. URL https://sites.google.com/site/danielefausti/educational-materials.

[7] H. P. Breuer and F. Petruccione. *The Theory of Open Quantum Systems*. Oxford University Press, New York, 2002.

[8] F. Giusti. Quantum state tomography applied to time resolved spectroscopy, 2014. URL https://sites.google.com/site/danielefausti/educational-materials.

[9] Miguel A. Alonso. Wigner functions in optics: describing beams as ray bundles and pulses as particle ensembles. *Adv. Opt. Photon.*, 3(4):272–365, Dec 2011. doi: 10.1364/AOP.3.000272. URL http://aop.osa.org/abstract.cfm?URI=aop-3-4-272.

[10] Wolfgang P. Schleich. *Quantum Optics in Phase Space*. Wiley-VCH, 2001.

[11] Ulf Leonhardt. *Measuring the Quantum State of Light*. CAMBRIDGE STUDIES IN MODERN OPTICS, 1997.

[12] C. Cohen-Tannoudji and F. Laloe B. Diu. *Quantum Mechanics*. Wiley, Paris, 1977.

[13] Normal mode. URL https://en.wikipedia.org/wiki/Normal_mode.

[14] Ulf Leonhardt. *Quantum Optics*. CAMBRIDGE UNIVERSITY PRESS, 2010.

[15] Stefano Olivares. Quantum optics in the phase space - a tutorial on gaussian states. *Eur. Phys. J. Special Topics*, 203:3–24, 2012.

[16] Scully and Zubairy. *Quantum Optics*. Cambrige University Press, 1997.

[17] Roy J. Glauber. Coherent and incoherent states of the radiation field. *Phys. Rev.*, 131:2766–2788, Sep 1963. doi: 10.1103/PhysRev.131.2766. URL http://link.aps.org/doi/10.1103/PhysRev.131.2766.

[18] S. Sachdev. Quantum criticality: competing ground states in low dimensions. *Science*, 288:475–480, 2000.

[19] Khomskii D. I. *Basic aspects of the qunatum theory of solids*. Cambridge University Press, 2010.

[20] Grosso and Pastori Parravicini. *Solid state physics*. Accademic Press, 2000.

[21] Ashcroft and Mermin. *Solid state physics*. Cengale Learning, Belmont, 1976.

[22] Huedong Xu and Franco Nori. Quantum phonon optics: coherent and squeezed atomic displacements. *Phys. Rev. B*, 53:2419–2424, 1996.

[23] M. Artoni and Joseph L. Birman. Non-classical states in solids and detection. *Optics Communications*, 104(4–6):319 – 324, 1994. ISSN 0030-4018. doi: http://dx.doi.org/10.1016/0030-4018(94)90563-0. URL http://www.sciencedirect.com/science/article/pii/0030401894905630.

[24] Sharmishtha Ghoshal and Ashok Chatterjee. Nonclassical behaviour of phonons in a polariton system. *Physics Letters A*, 223(3):195 – 203, 1996. ISSN 0375-9601. doi: http://dx.doi.org/10.1016/S0375-9601(96)89418-7. URL http://www.sciencedirect.com/science/article/pii/S0375960196894187.

[25] Huedong Xu and Franco Nori. Squeezed phonon states: Modulating quantum fluctuations of atomic displacements. *Phys. Rev. Lett.*, 76:2294–2297, 1996.

[26] Rojo A. Sood A. Whitaker J. Garrett, G. and R. Merlin. Vacuum squeezing of solids: macroscopic quantum states driven by light pulses. *Science*, 275:1638–1640, 1997.

[27] Whitaker J. Sood A. Garrett, G. and R. Merlin. Ultrafast optical excitation of a combined coherent-squeezed phonon field in $SrTiO_3$. *Opt. Express*, 1:385–389, 1997.

[28] Huedong Xu and Franco Nori. Phonon squeezed states: quantum noise reduction in solids. *Physica B*, 263-264:16–29, 1999.

[29] A. M. Lindenberg, I. Kang, S. L. Johnson, T. Missalla, P. A. Heimann, Z. Chang, J. Larsson, P. H. Bucksbaum, H. C. Kapteyn, H. A. Padmore,

R. W. Lee, J. S. Wark, and R. W. Falcone. Time-resolved x-ray diffraction from coherent phonons during a laser-induced phase transition. *Phys. Rev. Lett.*, 84:111–114, Jan 2000. doi: 10.1103/PhysRevLett.84.111. URL http://link.aps.org/doi/10.1103/PhysRevLett.84.111.

[30] Sakai K. Misochko, O. V. and S. Nakashima. Phase-dependent noise in femtosecond pump-probe experiments on Bi and GaAs. *Phys. Rev. B*, 61: 11225–11228, 2000.

[31] Dekorsy T. Bartels, A. and H. Kurz. Impulsive excitation of phonon-pair combination states by second-order raman scattering. *Phys. Rev. Lett.*, 84: 2981–2984, 2000.

[32] A. Hussain and S. R. Andrews. Absence of phase-dependent noise in time-domain reflectivity studies of impulsively excited phonons. *Phys. Rev. B*, 81: 224304, 2010.

[33] Daniels J. M. Reiter D. E. Kuhn T. Vagov A. Sauer, S. and V. M. Axt. Lattice fluctuations at a double phonon frequency with and without squeezing: an exactly solvable model of an optically excited quantum dot. *Phys. Rev. Lett.*, 105:157401, 2010.

[34] Wigger D. Axt V. M. Reiter, D. E. and T. Kuhn. Generation and dynamics of phononic cat states after optical excitation of a quantum dot. *Phys. Rev. B*, 88:195327, 2011.

[35] Hu J. Misochko, O. V. and K. G. Nakamura. Controlling phonon squeezing and correlation via one- and two-phonon interference. *Phys. Lett. A*, 375:4141, 2011.

[36] Misochko O. V. Hu, J. and K. G. Nakamura. Direct observation of two-phonon bound states in znte. *Phys. Rev. B*, 84:224304, 2011.

[37] O. V. Misochko. Nonclassical states of lattice excitations: squeezed states and entangled phonons. *Phys. Usp.*, 183:917–933, 2013.

[38] Seletskiy D. V. Moskalenko A. S. Schmidt J. F. Krauspe P. Eckart S. Eggert S. Burkard G. Riek, C. and Leitenstorfer A. Direct sampling of electric-field vacuum fluctuations. *Science*, 350:420–423, 2015.

[39] Xuedong Hu and Franco Nori. Phonon squeezed states generated by second-order raman scattering. *Phys. Rev. Lett.*, 79:4605–4608, Dec 1997. doi: 10.1103/PhysRevLett.79.4605. URL http://link.aps.org/doi/10.1103/PhysRevLett.79.4605.

[40] H. J. Zeiger, J. Vidal, T. K. Cheng, E. P. Ippen, G. Dresselhaus, and M. S. Dresselhaus. Theory for displacive excitation of coherent phonons. *Phys. Rev. B*, 45:768–778, Jan 1992. doi: 10.1103/PhysRevB.45.768. URL http://link.aps.org/doi/10.1103/PhysRevB.45.768.

[41] R. Merlin. *Raman Scattering in Materisals Science*. Springer, Berlin, 2000.

[42] Hans Kuzmany. *Solid-state spectroscopy*. Springer, Heidelberg, 2009.

[43] Fox M. *Optical proprieties of Solids*. Oxford University press, 2010.

[44] Etchepare, GRILLON, CHAMBARET, HAMONIAUX, and ORSZAG. Polarization selectivity in time-resolved transient phase grating. *Optic. Comm.*, 63, 1987.

[45] Kuhl J. Stevens, T. E. and R. Merlin. Coherent phonon generation and the two stimulated raman tensors. *Phys. Rev. B*, 65:144304, 2002.

[46] Dhar, Rogers, and Nelson. Time-resolved vibrational spectroscopy in the impulsive limit. *Chem. Rev.*, 94:157, 1994.

[47] S. Mukamel. *Principles of Nonlinear Optical Spectroscopy*. Oxford University Press, 1995.

[48] Grimm H. Dorner, B. and H. Rzany. Phonon dispersion branches in α quartz. *J. Phys. C: Solid State Phys.*, 13.

[49] J. F. Scott. Evidence of coupling between one- and two-phonon excitations in quartz. *Phys. Rev. Lett.*, 21:907–910, 1968.

[50] R. Alicki and K. Lendi. *Quantum Dynamical Semigroups and Applications, Lect. Notes Phys. 717*. Springer-Verlag, Berlin, 2007.

3

Measuring quantum states of light

The quantum state is what one knows about a physical system[1]. Light is the first physical system of which scientists experimentally measured the quantum state[2]. Light has indeed a notable propriety: it exhibits quantum features at room temperature and for this reason it is relatively easy to prepare, measure and manipulate quantum states of light. Nowadays Quantum Optics is one of the most promising platform for new technologies ranging from information processing to communications, driving forward the quantum information revolution[3]. Estimating the quantum state of optical fields is the basic tool of this research field. The main experimental goal of this thesis is to measure the quantum states of light pulses after the interaction with a photo-excited material. In this Chapter the problem of the quantum state estimation of optical pulses in addressed.

3.1 Introduction

In Classical Mechanics, one can always fully recover the state of a system by a set of multiple measurements on it. In Quantum Mechanics this is not always possible, due to fundamental limitations imposed by the very nature of the theory. In fact, the Heisenberg uncertainty principle forbids to perform an arbitrary sequence of measurements on a single system without inducing on it modifications of some sort. Moreover, the no-cloning theorem asserts that it is not possible to create a perfect copy of the system without already knowing its state in advance. Thus, in general, there is no way to infer the quantum state of a single system doing measurements on it. Nevertheless, it is possible to estimate the unknown quantum state of a physical system when many identical copies of it are available in the same state: in this way independent measurements can be performed on each copy. *Quantum*

state estimation typically consists in several measurements performed on identically prepared copies of the system, each time modifying the measurement apparatus so that different sets of data, associated with different observables of the system, can be acquired[4]. Then, the data are combined using tomographic algorithms to finally get the state of the system. The problem of quantum state determination through repeated measurements on identical copies of a quantum system dates back to the early days of Quantum Mechanics, it was studied for the first time in 1957 by Fano[5], who recognized the need of measuring more than two non commuting observables to achieve such goal. He called *quorum* a set of observables whose measurements is sufficient to provide a complete determination of the state of the system. However, Quantum Optics opened a new era for state reconstruction[6]. The first experimental demonstration of a quantum state reconstruction was done in the domain of Quantum Optics by Smithey et al. in 1993[2], on the basis of the theoretical work of Vogel and Risken (1989)[7]. This 1993 paper introduced the term *tomography* into Quantum Optics and its general scheme is still used today for investigating quantum properties of continuous variable states of light[1]. Nowadays, quantum tomography is applied to a variety of quantum systems[4,8] and constitutes a standard tool especially in the experimental implementation of Quantum Information protocols[9]. Quantum state reconstruction methods turn out to be of paramount importance for quantum information, for they can reveal the presence of quantum coherence and entanglement, not possible in a classical setting[10].

Here we focus on the problem of turning noisy data sets in reconstructed quantum states. The problem of noisy data inversion for quantum homodyne tomography has been and is largely addressed in the scientific debate[11–22]. We treated this issue with two different but parallel roads. The first is addressed in this Chapter and consists in using reconstruction algorithms suitable for treating very noisy data obtained with low efficient commercial detection systems. The second approach is reported in the Appendix A of the thesis, in that case we address the same problem of detection inefficiencies from the experimental and technological point of view through the design and realization of a high efficient detection system working in reduced noise conditions. This Chapter is organized as follows,

- We firstly trace a general description of homodyne detection, the experimental technique for the measurement of quantum states of light involving continuous variable, that is continuous degrees of freedom like field amplitude and phase (Section 3.2).
- Secondly we introduce the Wigner function reconstruction problem, the tomographic procedure that, starting from the experimentally obtained balanced homodyne detection data, retrieves the quantum state of the electromagnetic field under investigation (Section 3.3).
- Finally our contributions to the field are reported: a theoretical-experimental research about optical Gaussian states reconstruction with low homodyne detection efficiency (Section 3.4) and a study on the possibility of reconstructing purely quantum interferences in the same low efficiency conditions using simulated noisy data (Section 3.5)

Our results about the design and realization of a low noise homodyne detection apparatus are instead reported in the Appendix A of the thesis.

3.2 Balanced homodyne detection

Balanced homodyne detection is an experimental method that is used for the reconstruction of quantum states of monochromatic light. In this framework, the quantum state is characterized by feeding to appropriate tomographic techniques the results of repeated measurement of the optical field quadratures x_Φ for different phases $\Phi \in [0, \pi]$[2,7,8]. The quadratures of the electromagnetic field have been defined in the previous Chapter, in the quantum harmonic oscillator section. They are continuum-spectrum observables and constitute a *quorum*, whose measurement provides a complete information about the quantum state of a single mode of the electromagnetic field. Denoting by $\hat{a}$ and $\hat{a}^\dagger$ the single mode annihilation and creation operators, the quadrature operator is defined as,

$$\hat{x}_\Phi = \frac{\hat{a}e^{-i\Phi} + \hat{a}^\dagger e^{i\Phi}}{\sqrt{2}} \ . \tag{3.1}$$

Balanced homodyne detection allows for the measurement of such observables. The schematic diagram of a balanced homodyne detector is reported in Fig (3.1). The photon state under investigation, the *signal*, is mixed with a strong coherent

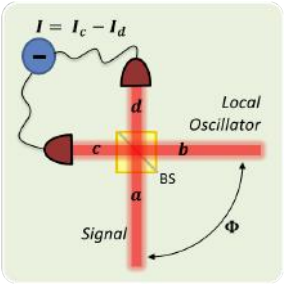

Figure 3.1: Schematic diagram of a balanced homodyne detector. The signal under investigation (in the mode a) interferes with the local oscillator (in the mode (b) on a $50/50$ beam splitter (BS). The phase difference between the two input optical modes is indicated with Φ. The intensities of the output modes, c and d, are detected with two photodiodes and the difference between the two photocurrents is measured.

reference state, the local oscillator (LO), by a $50/50$ beam splitter BS, whence the attribute *balanced*. The relative phase between the *signal* and the LO is indicated with Φ. The BS outputs are collected by two photodiodes and the difference photocurrent I (homodyne photocurrent) is measured. It can be proven that, under appropriate experimental conditions, the homodyne photocurrent is proportional to the *signal* quadrature defined in (3.1)[9]. We report now the guidelines of this demonstration[23].

The *signal* mode a is in the state $\hat{\rho}$ under investigation, it interferes with the second mode b (LO) excited in a coherent state $|z\rangle$ with $z \in \mathbb{C}$. A beam splitter is an optical device composed of a dielectric plate that produces the mixing of the two incident optical modes a and b. In general, a beam splitter is described by a unitary evolution operator:

$$U_{BS}(\kappa) = \exp(\kappa \hat{a}^\dagger \hat{b} - \kappa^* \hat{a} \hat{b}^\dagger), \tag{3.2}$$

where $\kappa = |\kappa| e^{i\chi} \in \mathbb{C}$ is proportional to the interaction time and to the linear susceptibility of the medium. The Heisenberg evolution of the modes a and b under the action of U_{BS} is:

$$U_{BS}^\dagger(\kappa) \begin{pmatrix} \hat{a} \\ \hat{b} \end{pmatrix} U_{BS}(\kappa) = \mathbf{B}(\kappa) \begin{pmatrix} \hat{a} \\ \hat{b} \end{pmatrix} \tag{3.3}$$

where

$$\mathbf{B}(\kappa) = \begin{pmatrix} \cos|\kappa| & e^{i\chi} \sin|\kappa| \\ -e^{i\chi} \sin|\kappa| & \cos|\kappa| \end{pmatrix}. \tag{3.4}$$

In particular, for a 50/50 BS, the parameters of the evolution operator in (3.2) are $\chi = 0$ and $|\kappa| = \pi/4$, so the action of a 50/50 BS on the incident modes a and b is the following:

$$\begin{cases} \hat{a} & \longrightarrow \hat{c} = (\hat{a} + \hat{b})/\sqrt{2} \\ \hat{b} & \longrightarrow \hat{d} = (\hat{b} - \hat{a})/(\sqrt{2}) \end{cases}, \tag{3.5}$$

where $\hat{c}$ and $\hat{d}$ are the output mode operators. After the BS, the two modes are detected by two identical photodiodes, the two photocurrents are measured and subtracted. The photocurrents I_c and I_d are the measured values of the the photon number observables $\hat{n}_c = \hat{c}^\dagger \hat{c}$ and $\hat{n}_d = \hat{d}^\dagger \hat{d}$. The difference photocurrent $\hat{I}$ can be expressed as

$$\hat{I} = \hat{n}_c - \hat{n}_d = \hat{c}^\dagger \hat{c} - \hat{d}^\dagger \hat{d}, \tag{3.6}$$

which, using the transformations in (3.5), becomes

$$\hat{I} = \hat{a}^\dagger \hat{b} + \hat{b}^\dagger \hat{a}. \tag{3.7}$$

The phase difference between the LO and the *signal* can be experimentally controlled changing the length of the LO optical path; this means that the LO modes are subjected to the following phase shift:

$$\begin{array}{lll} \hat{b} & \rightarrow & \hat{b}\, e^{i\Phi} \\ \hat{b}^\dagger & \rightarrow & \hat{b}^\dagger\, e^{-i\Phi}, \end{array} \tag{3.8}$$

and the homodyne photocurrent operator can be defined as

$$\hat{I}_\Phi = \hat{a}^\dagger \hat{b}\, e^{i\Phi} + \hat{b}^\dagger \hat{a}\, e^{-i\Phi}. \tag{3.9}$$

Now the natural question is: how, measuring the homodyne photocurrent $\hat{I}_\Phi$, can

one obtain a value for the quadrature $\hat{x}_\Phi$ for a fixed phase shift Φ of the LO mode? The answer comes from the fact that the expectation value of the homodyne photocurrent $\hat{I}_\Phi$ on the total input state $\hat{\rho}\otimes|z\rangle\langle z|$ is proportional to the expectation value of the field quadrature $\hat{x}_\Phi$ defined in (3.1):

$$\begin{aligned}
\langle \hat{I}_\Phi \rangle &= \mathrm{Tr}\left[\hat{\rho}\otimes|z\rangle\langle z|\,\hat{I}_\Phi\right] = \mathrm{Tr}\left[\hat{\rho}\otimes|z\rangle\langle z|\,(\hat{a}^\dagger\hat{b}\,e^{i\Phi}+\hat{b}^\dagger\hat{a}\,e^{-i\Phi})\right] \\
&= \mathrm{Tr}\left[\hat{\rho}\otimes|z\rangle\langle z|\,(\hat{a}^\dagger\hat{b}\,e^{i\Phi})\right] + h.c. = \left(\mathrm{Tr}[\hat{\rho}\,\hat{a}^\dagger]\cdot\mathrm{Tr}[|z\rangle\langle z|\hat{b}\,e^{i\Phi}]\right) + h.c. \\
&= \left(\mathrm{Tr}[\hat{\rho}\,\hat{a}^\dagger]\cdot\langle z|\hat{b}\,e^{i\Phi}|z\rangle\right) + h.c. = \left(\mathrm{Tr}[\hat{\rho}\,\hat{a}^\dagger]\cdot z\,e^{i\Phi}\right) + h.c. \\
&= \mathrm{Tr}\left[\hat{\rho}\,(\hat{a}^\dagger\,z\,e^{i\Phi}+\hat{a}\,z^*\,e^{-i\Phi})\right] = |z|\,\mathrm{Tr}\left[\hat{\rho}\,\underbrace{(\hat{a}^\dagger e^{i\Phi}+\hat{a}e^{-i\Phi})}_{\sqrt{2}\hat{x}_\Phi}\right] \\
&= \sqrt{2}\,|z|\,\langle\hat{x}_\Phi\rangle\,, \qquad (3.10)
\end{aligned}$$

where $\mathrm{Tr}\,[\hat{\rho}\otimes|z\rangle\langle z|I_\Phi]$ is the expectation value of the photocurrent $\hat{I}_\Phi$ on the total input state $\hat{\rho}\otimes|z\rangle\,\langle z|$, and we redefined $\Phi\to\Phi+\theta$ where θ is the phase of z ($z=|z|e^{i\theta}$). Balanced homodyne detection thus measures the field quadratures $\hat{x}_\Phi$ calibrating the measured $\hat{I}_\Phi$ by a factor $(\sqrt{2}\,|z|)$. Redefining the homodyne photocurrent $\hat{I}_\Phi$ including the calibration factor, its expectation value coincides now with the quadratures's one:

$$\hat{I}_\Phi = \frac{\hat{a}^\dagger\hat{b}\,e^{i\Phi}+\hat{b}^\dagger\hat{a}\,e^{-i\Phi}}{\sqrt{2}\,|z|}. \qquad (3.11)$$

The reference phase Φ is provided by the LO phase shift and can be experimentally controlled, providing the access to the outcome statistics of the measured homodyne photocurrent $\hat{I}_\Phi$ for different values of $\Phi\in[0,\pi]$. The scheme of a typical experimental apparatus for balanced homodyne detection is show in Fig 3.2.

We stress that in order to ensure that the output statistics of $\hat{I}_\Phi$ coincides with the one of the quadrature $\hat{x}_\Phi$, it is not sufficient that their expectation values coincide. Having the same expectation values does not guarantee indeed to have two identical observables. In particular, two specific conditions must be verified. The first originates from the observation that the operator $\hat{I}_\Phi$ has a discrete spectrum while $\hat{x}_\Phi$ is a continuum-spectrum observable. This problem can be overcome if the local oscillator is in a strong semiclassical state (high intensity coherent state) such that to be treated classically, its quantum fluctuations can be neglected and $\hat{b}\to z$. In this case $\hat{I}_\Phi$ approaches to have a continuum eigenvalues spectrum. The second condition deals with the fact that the expectation values of the statistical momenta of order larger than one are different from the quadratures ones. Indeed,

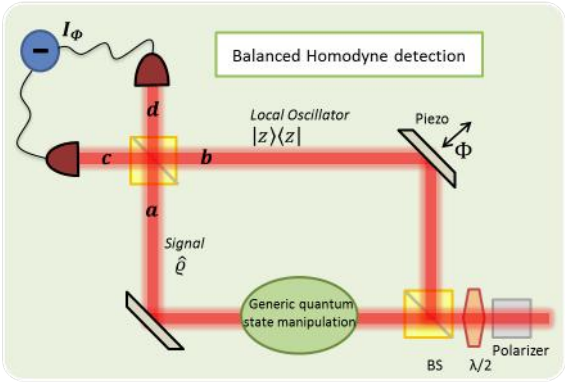

Figure 3.2: Scheme of balanced homodyne detection experimental apparatus. Mach-Zehnder interferometer. The phase difference Φ between the signal and the local oscillator is controlled by changing the length of the local oscillator optical path through a movable mirror mounted on a piezo-electric translator.

for the second order momentum, one finds

$$\begin{aligned}\langle \hat{I}^2_\Phi \rangle &= \frac{1}{2|z|^2}\mathrm{Tr}[\hat{\rho}\otimes|z\rangle\langle z|\,(\hat{a}^\dagger\hat{b}\,e^{i\Phi}+\hat{b}^\dagger\hat{a}\,e^{-i\Phi})^2] \\ &= \mathrm{Tr}[\hat{\rho}\otimes|z\rangle\langle z|\,(\hat{x}^2_\Phi+\frac{\hat{a}^\dagger\hat{a}}{2\,|z|^2})] \\ &= \langle\hat{x}^2_\Phi\rangle+\langle\frac{\hat{a}^\dagger\hat{a}}{2\,|z|^2}\rangle\,. \end{aligned} \tag{3.12}$$

This result can be generalized[9] to all the statistical momenta of the homodyne photocurrent:

$$\begin{aligned}&\langle\hat{I}_\Phi\rangle=\langle\hat{x}_\Phi\rangle\,, \qquad \langle\hat{I}^2_\Phi\rangle=\langle\hat{x}^2_\Phi\rangle+\langle\tfrac{\hat{a}^\dagger\hat{a}}{2\,|z|^2}\rangle\,, \\ &\ldots \qquad \langle\hat{I}^n_\Phi\rangle=\langle\,\hat{x}^{2n-2}_\Phi\,(x^2_\Phi+\tfrac{\hat{a}^\dagger\hat{a}}{2|z|^2})\,\rangle\,. \end{aligned} \tag{3.13}$$

One can notice that they tend to the quadrature momenta only if $\langle\hat{a}^\dagger\hat{a}\rangle \ll |z|^2$. In conclusion balanced homodyne detection achieves the measurement of the optical field quadrature only in the high intensity local oscillator regime, defined by the two following conditions:

$$\begin{aligned} &i) \quad |z| \gg 1 \\ &ii) \quad |z|^2 \gg \langle\hat{a}^\dagger\hat{a}\rangle\,. \end{aligned} \tag{3.14}$$

The first condition guarantees the continuous spectrum of the homodyne photocurrent $\hat{I}_\Phi$. The second neglects extra terms in the photocurrents statistical momenta. In this regime the probability distribution of the output photocurrent $\hat{I}_\Phi$ approaches the probability distribution $p(x,\Phi)=\langle x_\Phi|\rho|x_\Phi\rangle$ of the quadrature $\hat{x}_\Phi$ for the *signal* mode a at a given phase Φ. In the following subsection this

derivation is generalized to the case of pulsed light, which can not be describes as a single mode optical field.

3.2.1 The pulsed regime: a multimode treatment

The balanced homodyne detection of single mode photon states of monochromatic light need to be generalized when laser pulsed light is used[24–31]. In this case, the optical pulses are equally prepared multi-mode coherent quantum states. For each single pulse a quadrature measurement is performed. In such regime, the single mode balanced homodyne detection description can still be used if the single mode field operators are replaced by suitable multi-mode annihilation and creation operators. For this reason we present here a theoretical treatment for pulsed homodyne detection which demonstrates that the single mode balanced homodyne detection treatment can still be adopted in case of laser pulses, provided that appropriate concerns are considered. Homodyne detection in pulsed regime requires a formal generalization of its theoretical description with respect to the one-mode regime[31] since the *LO* and the *signal* at the beam splitter are not monochromatic. We introduced the formalism for the description of multimode quantum states of light in Section 2.4. By means of that formalism we can now extend the state-tomography techniques to the case in which the *signal* and the *LO* are pulsed.

In the monochromatic case, when the *signal* mode a interferes with the *LO* mode b on the beam splitter, the photo-current operator is $\hat{I} = \hat{a}^\dagger \hat{b} + \hat{b}^\dagger \hat{a}$[9].
If more frequencies ω_j are present both in the *LO* and in the *signal*, each one of the corresponding mode operators will be subjected to the beam splitting transformation and the detectors will ideally register photons of all involved frequencies. Then, the photo-current operator becomes $\hat{I} = \sum_j \hat{a}_j^\dagger \hat{b}_j + \hat{b}_j^\dagger \hat{a}_j$.

If the *LO* is in a pulsed coherent state $|\bar{z}\rangle = e^{\hat{B}^\dagger(\bar{z}) - \hat{B}(\bar{z})} |0\rangle$, with generalized creation and annihilation operators $\hat{B}^\dagger(\bar{z}) = \sum_j z_j \hat{b}_j^\dagger$ and $\hat{B}(\bar{z}) = \sum_j z_j^* \hat{b}_j$, the phase difference Φ between the *LO* and the *signal* is changed by the action of the piezoelectric translator placed in the *LO* arm on all the *LO* modes:

$$\hat{b}_j \to \hat{b}_j \, e^{i\Phi} \ , \qquad \hat{b}_j^\dagger \to \hat{b}_j^\dagger \, e^{-i\Phi} \ . \tag{3.15}$$

The photo-current operator which is measured by the pulsed homodyne setup is thus given by

$$\hat{I}_\Phi = \sum_j \left(\hat{a}_j^\dagger \, \hat{b}_j \ e^{i\Phi} \ + \ \hat{a}_j \, \hat{b}_j^\dagger \, e^{-i\Phi} \right) \ . \tag{3.16}$$

Let us consider $\hat{\rho}$ the quantum state (density matrix) of the *signal* field and $|\bar{z}\rangle \langle \bar{z}|$ the projector onto the (coherent) state of the incoming pulse. Then, using that $\hat{b}_j |\bar{z}\rangle = z_j |\bar{z}\rangle$ and the definition of the multimode field operators in (2.44), the expectation value $I_\Phi = \mathrm{Tr}\left[\rho \otimes |\bar{z}\rangle \langle \bar{z}| \ \hat{I}_\Phi\right]$ of the photo-current is calculated as

follows:

$$\begin{aligned} I_\Phi &= \sum_j \left(\mathrm{Tr}\left[\hat{\rho}\,\hat{a}_j^\dagger\right] \cdot \langle \bar{z}|\hat{b}_j|\bar{z}\rangle \; e^{i\Phi} + h.c. \right) \\ &= \sum_j \left(\mathrm{Tr}\left[\hat{\rho}\,(\hat{a}_j^\dagger \, z_j \, e^{i\Phi} + \hat{a}_j \, z_j^* \, e^{-i\Phi})\right] \right) \\ &= \mathrm{Tr}\left[\hat{\rho}\,\left(\hat{A}^\dagger(\bar{z})\, e^{i\Phi} + \hat{A}(\bar{z})\, e^{-i\Phi}\right)\right] \; . \end{aligned} \tag{3.17}$$

Using (2.46) and comparing these results in the standard treatment of homodyne detection for the single-mode case, one realizes that in the pulsed regime one measures a quantity I_Φ,

$$I_\Phi = \sqrt{2}\,|\bar{z}|\,\mathrm{Tr}\left[\hat{\rho}\,\hat{X}_\Phi\right] \; , \tag{3.18}$$

proportional to a quadrature which generalizes that in (3.1):

$$\hat{X}_\Phi = \frac{\hat{A}^\dagger\, e^{i\Phi} + \hat{A}\, e^{-i\Phi}}{\sqrt{2}} \; . \tag{3.19}$$

For this reason, we will refer to the simpler case of a single mode homodyne detection, with the proviso that whenever a quadrature is used, it actually refers to its expression (equation (3.19)) in the pulsed regime. In particular, the measured data can be used to reconstruct the expectation values of all *signal* observables that can be expressed as functions of the operators $\hat{A}$ and $\hat{A}^\dagger$. For instance, the mean value of the second statistical momentum photo-current operator with respect to the LO pulsed coherent state $|\bar{z}\rangle\langle\bar{z}|$ is

$$\langle \bar{z}|\; \hat{I}_\Phi^2 \,|\bar{z}\rangle = 2\,|\bar{z}|^2\, \hat{X}_\Phi^2 \; + \sum_j \hat{a}_j^\dagger \hat{a}_j \; , \tag{3.20}$$

and differs from the pulsed quadrature second moment $\hat{X}_\Phi^2$ by the number of photons in the pulsed *signal* which has to be taken much smaller than the intensity $|\bar{z}|^2$ of the pulsed LO. A similar suppression by $|\bar{z}|^{-2}$ occurs for the correction terms appearing in higher momenta so that the distribution of the outcomes of the homodyne photocurrent is equal to that of the corresponding field quadratures. As a final remark, notice that, in the case of only one frequency mode, the above treatment reduces to the single mode one.

3.3 Optical homodyne tomography

The main goal of quantum state estimation is to answer to the following question: given the experimental outcomes of the measurement of a set of observables, which was the quantum state of the investigated system? This *inversion problem* is the core of quantum state tomography. We focus here on quantum state tomography of light in continuous variable. In particular, the tomographic procedure for light quantum state estimation from balanced homodyne detection experimental data is

known as *optical homodyne tomography*[1]. Repeated homodyne measurements on identically prepared light modes in the state $\hat{\rho}$ provide an experimental histogram which approaches the probability distribution of the quadrature outcome at a fixed phase:

$$p_\rho(x,\phi) = \mathrm{Tr}[\hat{\rho}\,|x_\Phi\rangle\,\langle x_\Phi|] = \langle x_\Phi|\hat{\rho}|x_\Phi\rangle\,. \tag{3.21}$$

This is the probability of having outcome x when measuring $\hat{x}_\Phi$. Once obtained such histograms for different phases $\Phi \in [0, 2\pi]$, the actual *optical homodyne tomography* is the mathematical procedure that from such set of experimental data leads to a complete characterization of the quantum state by reconstructing its density matrix $\hat{\rho}$ or equivalently its Wigner function W_ρ. The Wigner function (treated in detail in the previous Chapter) is a convenient representation of the optical quantum state in the phase space since its marginals exactly correspond to the quadratures probability distributions in (3.21).

The mathematical approaches to the problem of *optical homodyne tomography* are divided in two categories, (i) the *inverse linear transform techniques* and (ii) the *statistical inference techniques*[1]. The first category is based of the philosophy of determining the state $\hat{\rho}$ by directly inverting the linear relation in (3.21) through back-projection algorithms[32] usually adopted also in medical tomography. The second category is instead based on looking for the most probable density matrix that will generate the observed data my means of non linear algorithms like *maximum likelihood estimation*[14] and *Bayesian mean estimation*[6]. The two approaches have been very nicely summarized with two corresponding questions to address: (i) "What quantum state is determined by that measurement?"and (ii) "What quantum states seem to be most likely for that measurement?"[4].

In this thesis we focused of the first approach, that is in retrieving the quantum state of optical fields under investigation from an inverse linear transformation of the (3.21). In particular we adopted specific quantum statistical methods based on minimax and adaptive estimation of the Wigner function from homodyne data with efficiency $\eta < 1$[21,22].

The scientific discussion about how to process homodyne data with low efficiency is of crucial importance. The debate, started about twenty years ago, is still vivid in the last few years and it is focused on the research of better and better approaches for treating noisy data. In particular, an intense discussion developed about the existence or not of a lower homodyne efficiency bound ($\eta = 0.5$), under which quantum state reconstruction is not achievable[11–22,31]. In this framework, it has been mathematically demonstrated that the algorithms of minimax and adaptive estimation of the Wigner function allow the tomographic reconstruction of quantum states of light for any homodyne detection efficiency keeping out the possibility of any efficiency lower limit[21,22], nevertheless in the same papers no empirical applications to the case of $\eta > 0.5$ have been shown. We used such mathematical algorithms to practically verify that the presence of very low homodyne detection efficiency (< 0.5) does not prevent the tomographic reconstruction of quantum states of light. We tested the cited algorithms[21,22] for $\eta < 0.5$, empirically demonstrating that such rigorous bound for loss compensation in homodyne tomography does not exist. We also studied in details the role of the parameters of

the algorithm in relation to the number of collected data. Specifically we applied the minimax and adaptive technique both to real experiments and to simulated ones, demonstrating its applicability for reconstructing Gaussian and non-Gaussian states provided that a sufficiently large number of data is collected. These results are presented in the following sections, here we report the principe of operation of the adopted mathematical algorithms.

3.3.1 Minimax and adaptive estimation of the Wigner function

Let us consider a quantum state $\hat{\rho}$, it can be completely characterised by the associated Wigner function $W_\rho(q,p)$ on the phase-space $(q,p) \in \mathbb{R}^2$; namely, by the non-positive definite quasiprobability density

$$W_\rho(q,p) = \frac{1}{(2\pi)^2} \int_{\mathbb{R}^2} \mathrm{d}u\mathrm{d}v \, \mathrm{e}^{i(uq+vp)} \, \mathrm{Tr}\left[\hat{\rho}\, \mathrm{e}^{-i(u\hat{q}+v\hat{p})}\right] , \tag{3.22}$$

where $\hat{q}$ and $\hat{p}$ are the position and momentum operators of the quantum harmonic oscillator which describes a single mode of the electromagnetic radiation. They obey the commutation relations $[\hat{q}\,,\hat{p}] = i$, $\hbar = 1$. The quadrature probability distribution in (3.21) can be conveniently related to the Wigner function by passing to polar coordinates $u = \xi\cos\phi$, $v = \xi\sin\phi$, such that $0 \le \phi \le \pi$ and $-\infty \le \xi \le +\infty$:

$$\begin{aligned} W_\rho(q,p) &= \int_0^\pi \mathrm{d}\phi \int_{-\infty}^{+\infty} \mathrm{d}\xi \frac{|\xi|}{(2\pi)^2} \, \mathrm{e}^{i\xi(q\cos\phi + p\sin\phi)} \, \mathrm{Tr}\left[\hat{\rho}\, \mathrm{e}^{-i\xi(\hat{q}\cos\phi+\hat{p}\sin\phi)}\right] \\ &= \int_0^\pi \mathrm{d}\phi \int_{-\infty}^{+\infty} \mathrm{d}\xi \frac{|\xi|}{(2\pi)^2} \int_{-\infty}^{+\infty} \mathrm{d}x \, \mathrm{e}^{i\xi(q\cos\phi+p\sin\phi-x)} \, p_\rho(x,\phi) \\ &= \int_0^\pi \mathrm{d}\phi \int_{-\infty}^{+\infty} \mathrm{d}\xi \frac{|\xi|}{(2\pi)^2} \int_{-\infty}^{+\infty} \mathrm{d}x \, \mathrm{e}^{i\xi(q\cos\phi+p\sin\phi)} \, F[p_\rho(x,\phi)](\xi), \end{aligned} \tag{3.23}$$

where $F[p_\rho(x,\phi)](\xi)$ denotes the Fourier transform with respect to x of the probability distribution:

$$F[p_\rho(x,\phi)](\xi) = \int_{-\infty}^{+\infty} \mathrm{d}x \, \mathrm{e}^{-ix\xi} \, p_\rho(x,\phi) \ . \tag{3.24}$$

In homodyne detection experiments, the collected data consist of n pairs of quadrature amplitudes and phases (X_ℓ, Φ_ℓ). These can be considered as independent, identically distributed stochastic variables. Since they are distributed according to $p_\rho(x,\phi)$ in (3.21), one could reconstruct the Wigner function by substituting the integration with a sum over the pairs for a sufficiently large number of data. However, the measured values x are typically not the eigenvalues of $\hat{x}_\phi$, rather those of

$$\hat{x}_\phi^\eta = \sqrt{\eta}\hat{x}_\phi + \sqrt{\frac{1-\eta}{2}}y \ , \ 0 \le \eta \le 1 \ , \tag{3.25}$$

where y is a normally distributed random variable describing the possible noise that may affect the homodyne detection data and η parametrizes the detection efficiency that increases from 0 to 100% with η increasing from 0 to 1[21]. We consider the noise Gaussian and independent from the statistical properties of the quantum state, that is y is considered as independent from $\hat{x}_\phi$. It thus follows that the eigenvalues of $\hat{x}_\phi^\eta$ are distributed accordingly to the following convolution:

$$p_\rho^\eta(x,\phi) = \int_{-\infty}^{+\infty} \mathrm{d}u \, \frac{\mathrm{e}^{-u^2/(1-\eta)}}{\sqrt{\pi(1-\eta)}} \, \frac{p_\rho\left(\frac{x-u}{\sqrt{\eta}},\phi\right)}{\sqrt{\eta}} \ . \tag{3.26}$$

Its Fourier transform is connected with that of $p_\rho(x,\phi)$ according to

$$F[p_\rho(\,x\,,\phi)](\xi) = \mathrm{e}^{\gamma\xi^2} \, F[p_\rho^\eta(\,x\,,\phi)](\xi/\sqrt{\eta}) \ , \quad \gamma = \frac{1-\eta}{4\eta} \ . \tag{3.27}$$

By inserting $F[p_\rho(\,x\,,\phi)](\xi)$ into (3.24), one can finally write the Wigner function in terms of the noisy probability distribution $p_\rho^\eta(x,\phi)$:

$$W_\rho(q,p) = \int_0^\pi \mathrm{d}\phi \int_{-\infty}^{+\infty} \mathrm{d}\xi \, \frac{|\xi|}{(2\pi)^2} \int_{-\infty}^{+\infty} \mathrm{d}x \, \mathrm{e}^{i\xi(q\cos\phi + p\sin\phi - x/\sqrt{\eta})} \, \mathrm{e}^{\gamma\xi^2} \, p_\rho(x,\phi) \ . \tag{3.28}$$

Then the Wigner function is reconstructed from a given set of n measured homodyne pairs (X_ℓ, Φ_ℓ) by means of an estimator of the form[21]

$$W_{h,n}^{\eta,r}(q,p) = W_{h,n}^\eta(q,p) \, \chi_r(q,p) \ , \tag{3.29}$$

where

$$W_{h,n}^\eta(q,p) = \frac{1}{n} \sum_{\ell=1}^{n} K_h^\eta \left([(q,p),\Phi_\ell] - \frac{X_\ell}{\sqrt{\eta}} \right) \ , \tag{3.30}$$

and

$$K_h^\eta \left([(q,p),\Phi_\ell] - \frac{X_\ell}{\sqrt{\eta}} \right) = \int_{-1/h}^{1/h} \mathrm{d}\xi \, \frac{|\xi|}{4\pi} \, \mathrm{e}^{i\xi(q\cos\Phi_\ell + p\sin\Phi_\ell - X_\ell/\sqrt{\eta})} \, \mathrm{e}^{\gamma\xi^2} \ . \tag{3.31}$$

The expression in (3.29) is an approximation of the Wigner function in (3.28) by a sum over n homodyne pairs (X_ℓ, Φ_ℓ). The parameter h serves to control the divergent factor $\exp(\gamma\xi^2)$, while r, through the characteristic function $\chi_r(q,p)$ of a circle $C_r(0)$ of radius r around the origin, restricts the reconstruction to the points (q,p) such that $q^2+p^2 \leq r^2$. Both parameters have to be chosen in order to minimise the reconstruction error which is conveniently measured by the L^2-distance between the true Wigner function and the reconstructed one, $\|W_\rho - W_{h,n}^{\eta,r}\|_2$ [22,33]. Since such a distance is a function of the data through $W_{h,n}^{\eta,r}$, the L^2-norm has to

be averaged over different sets, M, of quadrature data:

$$\Delta^{\eta,r}_{h,n}(\hat{\rho}) = E\left[\|W_\rho - W^{\eta,r}_{h,n}\|_2^2\right] \equiv E\left[\int_{\mathbb{R}^2} \mathrm{d}q\mathrm{d}p \left|W_\rho(q,p) - W^{\eta,r}_{h,n}(q,p)\right|^2\right] , \quad (3.32)$$

where E denotes the average over the M data samples. Each sample consists of n quadrature pairs (X_ℓ, Φ_ℓ) corresponding to measured values of x_ϕ with $\phi \in [0, \pi]$.

An optimal dependence of the parameters r and h upon the number of data, n, is obtained by minimizing an upper limit to $\Delta^{\eta,r}_{h,n}(\hat{\rho})$. The minimum value of such upper limit determines the optimal values of r and h.

In order to further optimize the expressions for the parameters h and r as functions of the number of data n an auxiliary parameter $\beta > 0$ is considered. This was introduced to characterise the localisation properties on $\mathbb{R}^2$ of the Fourier transforms of the Wigner functions of the following class of density matrices[22]:

$$\mathcal{A}_{\beta,s,L} = \left\{\rho : \int_{\mathbb{R}^2} \mathrm{d}q\mathrm{d}p \, |F[W_\rho](q,p)|^2 \, \mathrm{e}^{2\beta(w_1^2+w_2^2)^{s/2}} \leq (2\pi)^2 L\right\} . \quad (3.33)$$

We studied in details the role of the free parameter β in section 3.5. There it appears explicitly in the optimal functional dependence of the parameters r and h on the number of data n.

In the following we focus on the application of the minimax and adaptive algorithm to the reconstruction of quantum states of light in low efficiency conditions $\eta < 0.5$. We first consider Gaussian states, we prove, by both numerical and real experiments, that an effective discrimination of different Gaussian quantum states, in particular coherent and squeezed states, can be achieved. Then we consider non Gaussian states, in particular a linear superposition of two coherent states, demonstrating that, starting from simulated noisy homodyne data, quantum interferences can be actually retrieved in very low efficiency conditions. In last case we focused on the role of the parameter β on the reconstruction errors[33].

3.4 Gaussian states tomography with low homodyne efficiency

Pulsed homodyne quantum tomography usually requires a high detection efficiency, along with ad-hoc designed apparatus[34], limiting its applicability in Quantum Optics. However, new methods capable of discriminating between different quantum state of light, which demand lower detection capabilities typical of commercially available components, would facilitate the experimental realization of such apparatuses.

Here I report our recent results[31] which demonstrate that the presence of low detection efficiency ($< 50\%$) does not prevent the tomographic reconstruction of quantum states of light, specifically, of Gaussian type. This results are obtained by applying the so-called minimax adaptive reconstruction of the Wigner function[21,22] (presented in the previous section) to pulsed homodyne detection. In

particular, we prove, by both numerical and real experiments, that an effective discrimination of different Gaussian quantum states can be achieved. This would make possible to apply quantum homodyne detection to study different physical systems where high noise conditions are unavoidable, such as out of equilibrium light matter dynamics[35].

We developed a time-domain homodyne detection apparatus working with coherent ultra-short light pulses, built using commercial detectors and operating in a regime of large electronic noise. By treating the shot-to-electronic-noise ratio (about 2 dB) as a detector inefficiency[20,32], we obtain an overall detection efficiency of about 30%. We show that, even in these low efficiency conditions, it is still possible to discriminate coherent and squeezed photon states with high accuracy.

3.4.1 Experiments

The laser source is a mode-locked Ti:Sapphire oscillator with 80 MHz repetition rate which generates a train of 100 fs pulses at a wavelength of 800 nm. This source is pumped by a solid state laser which produces 18W of monochromatic continuous wave radiation at 532 nm (*Verdi V-18*). The oscillator has an output average power of 800 mW, of which only few mW are used for our experiment. A block representation of the laser system used in our experiment is given in Fig 3.3.

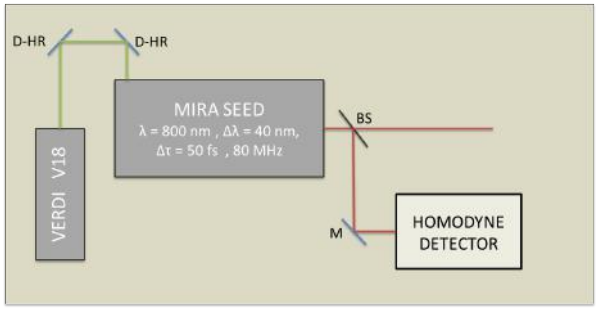

Figure 3.3: Block diagram of the laser sources system used in the experiment.

The experimental core of balanced homodyne detector is a Mach-Zehender interferometer. Fig 3.4 shows the experimental set-up. A beam splitter divides the incoming beam in two, the signal and the local oscillator, which then interfere in a second beam splitter (NPBS in Fig 3.4). The outputs of the second beam splitter are detected and subtracted by a commercial balanced amplified differential photodetector. Two 100 *mm* lenses focus the beam splitter output beams onto the entrances of the photodetector. The phase difference Φ between the two arms of the interferometer can be controlled by moving a mirror (M_2 in Fig 3.4) set up on a piezoelectric translator in the local oscillator arm (PZT in Fig 3.4). The latter is a piezo linear stage (*PI P622-ZCD*) with a travel range of 250 μm and a 1 nm

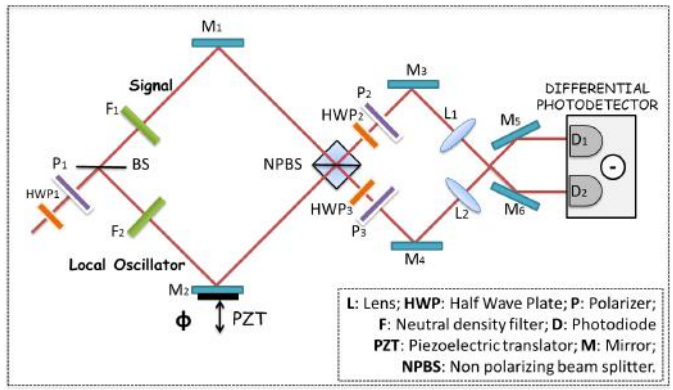

Figure 3.4: Scheme of the opto-mechanical setup for the balanced homodyne detection.

nominal resolution, connected to a piezo Servo-Controller (*PI E625*). A software controls and reads the piezo stage position along the motion axis. The total laser power can be varied by means of a half wave plate followed by a polarizer at the beginning of the system. Other two pairs of half wave plates and polarizers are put at the outputs of the second beam splitter, which is a (50/50) non polarizing cube beam splitter (NPBS). In this case, they are used to compensate the different efficiency of the photodiodes in the differential detector. The detection-acquisition system, sketched in Fig 3.5, consists of a commercial balanced amplified differential

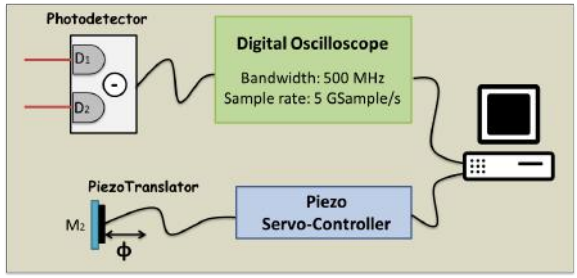

Figure 3.5: Block diagram of the acquisition system

photodetector (*Thorlabs PDB430A*) with a high bandwidth (from DC to 350 MHz) which is able to measure the difference between the photocurrents generated by the two beams in input. The latter is made up of two Si/PIN photodiodes with nominal quantum efficiency $\eta_{pd} = 0.85$ at 800 nm wavelength and linear response up to 0.6 mW LO power. The detector subtraction efficiency is quantified by the common mode rejection ratio (CMRR), defined as the ratio between the detector output power when both photodiodes are illuminated and the power when one of the two is screened[29]. For the present experiment CMRR$>$ 36 dB. The homodyne photocurrent is recorded by a digital oscilloscope (*Tektronix TDS3000B*) with a bandwidth of 500 MHz and a sampling rate of 5 GSamples/s. The digitized output

is numerically integrated over time intervals corresponding to the duration of the pulse. The integrated voltage for each pulse is associated with a single quadrature measurement. In Fig 3.6 a picture of the experimental opto-mechanical set up is shown.

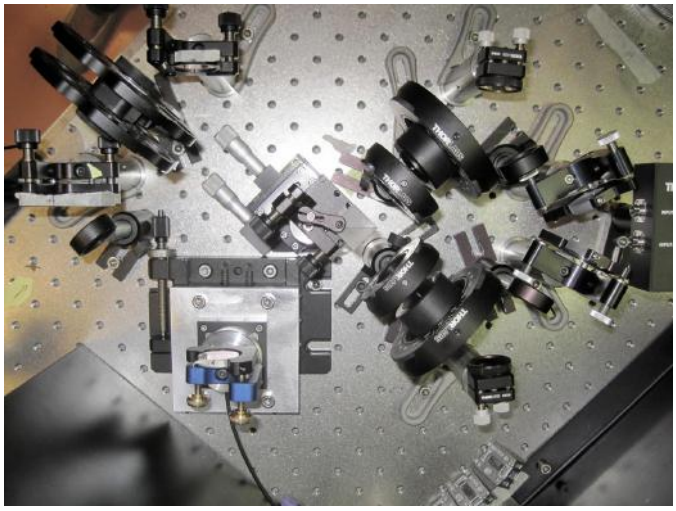

Figure 3.6: Experimental opto-mechanical set up

In the *shot noise regime* with the *signal* beam blocked, *i.e.* with the *signal* in the vacuum state, the homodyne detector noise variance is expected to change linearly with the LO power on the top of a constant offset representing the electronic noise[36]. Fig 3.7 shows the detector noise variance of 8×10^3 pulses, for different values of the LO power. The noise variance grows linearly up to 0.6 mW LO power, instead at higher powers the photodiodes non-linear effects are significant. To have the maximum shot-to-electronic noise ratio (≈ 2 dB) achievable in the linear regime, the experiments have been performed at 0.6 mW LO power. Conversely, when the

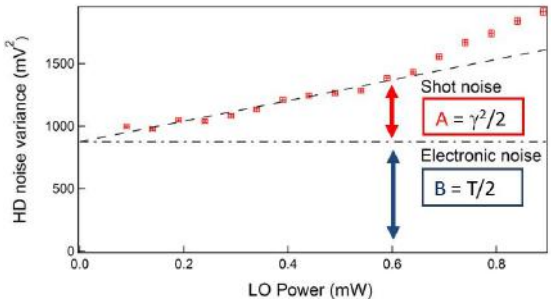

Figure 3.7: Detector noise variance versus *LO* power in absence of signal (vacuum state). Shot noise contribution (dashed curve); electronic noise background (dashed-dotted curve).

signal beam is not blocked, it can be attenuated with respect to the LO by neutral density filter (F_1 in Fig 3.4).

In the absence of electronic noise, the voltage V corresponding to the homodyne photocurrent, namely the experimentally accessible quantity, is proportional to the quadrature operator x_Φ, $V = \gamma\, x_\Phi$, with an appropriate constant γ. The electronic noise can be generically described by a classical stochastic process δ, that can be assumed to be Gaussian distributed, with zero average and variance $T/2$. The value of δ must be experimentally measured. Under these conditions the electronic noise is independent from the quadrature and it contributes to the homodyne voltage as,

$$V = \gamma\, x_\Phi + \delta\ . \tag{3.34}$$

A homodyne trace is obtained by collecting a set of homodyne voltage values V_ℓ, corresponding to different phase values Φ_ℓ, associated with a large number n of piezo positions.

In the case of the vacuum state (absence of *signal*), these considerations are outlined in Fig 3.7. The total vacuum homodyne variance for the chosen LO power is indeed composed of two independent contributions. An intrinsic contribution ($A = \gamma^2/2$) is actually the shot noise, while an extrinsic contribution ($B = T/2$) is due to the electronic noise. The electronic noise can be treated as an optical loss channel[20] with an equivalent transmission efficiency given by

$$\eta_{eq} = \frac{A}{A+B} = \frac{\gamma^2}{\gamma'^2}\ , \tag{3.35}$$

where $\gamma' = \sqrt{\gamma^2 + T}$. Here we estimate $\eta_{eq} = 0.37$. Thus the total apparatus efficiency is $\eta = \eta_{eq}\,\eta_{pd} = 0.31$.

Considering that the variances of independent stochastic variables are additive, γ' can be determined by using the vacuum state as reference and by assuming the variance of the quadrature operator in the vacuum to be 1/2,

$$\gamma' = \sqrt{2\,\langle V^2\rangle_0}\ , \tag{3.36}$$

where $\langle V^2\rangle_0$ is the experimental voltage variance for the vacuum state. To consistently apply the quantum state reconstruction to the collected experimental homodyne data, it is convenient to rescale the raw data V_ℓ by the constant γ',

$$X_\ell = V_\ell/\gamma'\ , \tag{3.37}$$

so that the new, calibrated quantities X_ℓ have variance 1/2. Fig 3.8 shows the case of two optical coherent states with different mean photon numbers, each homodyne trace consisting of $n = 8 \times 10^4$ experimental data. The data were collected using two different optical density for the signal attenuator (F_1 in Fig 3.4). Clearly even with a very low mean photon number signal (Fig 3.8 (b)), the phase modulation of the homodyne trace is detectable. These experimental homodyne data are used for the Wigner function reconstruction.

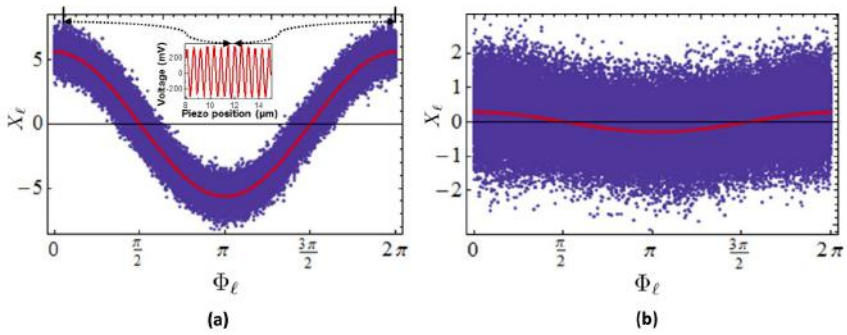

Figure 3.8: Calibrated homodyne traces of two optical coherent states. Each trace is acquired using a different optical density OD of the filter F_1. (a) $OD = 4.5$; (b) $OD = 7$. In the inset of (a) we show the interference figure obtained by measuring the mean value of four integrated pulses versus the piezo position. The homodyne traces are measured in the piezo range corresponding to the central optical cycle of the interference figure.

3.4.2 The Wigner function reconstruction

The experimental data are analyzed using the technique of minimax estimation of the Wigner function presented in section 3.3.1. For each experiment, the n homodyne data pairs (X_ℓ, Φ_ℓ) are used in the equations (3.31) in order to estimate the Wigner function in (3.30) for each point of the phase space. We put here the truncation parameter h equal to the optimal adaptive value obtained in[21], $h = h_{adap}$, with

$$h_{adap} = \left(\frac{2\eta \log n}{1-\eta} - \sqrt{\frac{2\eta \log n}{1-\eta}} \right)^{-1/2} . \tag{3.38}$$

Notice that the optimally adapted cutoff depends both on the detector efficiency η and the number n of collected data. When the efficiency becomes small, in order to have a good estimator of the Wigner function, a larger number n of data is needed. However, we stress that no inferior bound on η exists that prevents the convergence of the algorithm.

Once the Wigner function is reconstructed, the expectation value of any observable $\hat{O}$ of the system can be estimated as follows,

$$E^h_{\hat{O}} = \int_{\mathbb{R}^2} dq\, dp\; O(q,p)\, W^\eta_{h,n}(q,p) = \frac{1}{n} \sum_{\ell=1}^{n} R^{h,\eta}_{\hat{O}}(X_\ell, \Phi_\ell) \;, \tag{3.39}$$

where the corresponding kernel function is given by

$$R^{h,\eta}_{\hat{O}}(X_\ell, \Phi_\ell) = \int_{\mathbb{R}^2} dq\, dp\; O(q,p)\, K^{h,\eta}_{X_\ell,\Phi_\ell}(q,p) \;. \tag{3.40}$$

For testing the effectiveness of reconstruction approach under our experimental conditions, we first analyze sets of numerically generated data that simulate the quadratures of a known pure quantum state $|\psi\rangle$. By knowing in advance the quantum state, it is possible to verify whether the minimax technique allows a proper reconstruction. The generation of the fictitious data starts by using the quadrature probability distribution with $\eta = 1$ associated with a quantum state, and afterwards in adding to each numerically generated state quadrature a Gaussian noise which exactly simulates the electronic noise associated with the efficiency, *i.e.* $\eta = 0.31$, of our set-up. The analysis of the simulated data proceeds, as for experimental data, through a calibration using the vacuum noise as reference. In particular, we perform two numerical experiments. The first with a coherent state $|\psi\rangle = D(\alpha)\,|0\rangle$ and another one with a displaced-squeezed state $|\psi\rangle = D(\alpha)S(\xi)\,|0\rangle$, where

$$D(\alpha) = e^{\alpha\hat{a}^\dagger - \alpha^*\hat{a}}\ , \qquad S(\xi) = e^{1/2(\xi\hat{a}^{\dagger 2} - \xi^*\hat{a}^2)}\ , \tag{3.41}$$

are the displacement and squeezing operators, respectively. Each data set consists of $n = 8 \times 10^4$ quadrature measurements X_ℓ with the relative phase Φ_ℓ ranging in the interval $[0, 2\pi]$. Following the algorithm sketched in the previous section, we reconstruct the Wigner function of the two quantum states. They are shown in Fig 3.9 (a) and (b) for the coherent and the squeezed state respectively. To remove

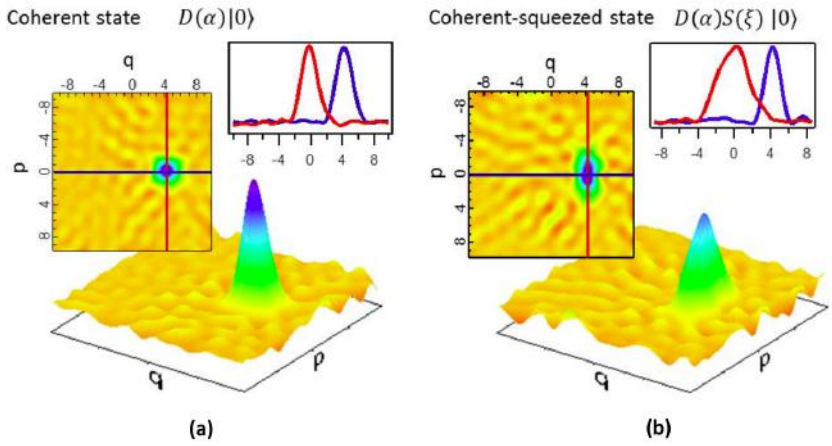

Figure 3.9: Reconstructed Wigner function from simulated data using the adaptive minimax estimation. Reconstruction from $n = 8 \times 10^4$ quadratures of (a) a coherent state ($\alpha = 3$) and (b) a displaced-squeezed state ($\alpha = 3$, $\xi = 0.8$). The used detector efficiency is in both cases $\eta = 0.31$. The insets show representative two-dimensional cuts of the reconstructed Wigner function.

the artifacts resulting by the numerical integration, the reported Wigner functions have been filtered by an image processing algorithm (low pass Gaussian convolution filtering). The blue and red curves are bidimensional cuts of the Wigner functions in correspondence of the expectation value of the position and momentum operator,

respectively. The fidelity of the Wigner function reconstruction has been calculated as follows,

$$f = \int_{\mathbb{R}^2} dq\, dp\; 2\pi\; W_e(q,p)\, W_r(q,p)\;, \tag{3.42}$$

where $W_e(q,p)$ is the exact Wigner function and $W_r(q,p)$ is the reconstructed one. We obtained a fidelity of 0.97 and 0.92 for the coherent and the squeezed state respectively. The results prove that the squeezed and coherent states can be discriminated under high noise conditions. Indeed, the features of the reconstructed Wigner functions clearly reflect the different nature of the two quantum states.
From the reconstructed Wigner function, it is possible to compute the expectation values of relevant observables with respect to the coherent and the displaced-squeezed state. In particular, the number operator $\hat{n} = \hat{a}^\dagger \hat{a}$ and the position $\hat{q}$ and momentum $\hat{p}$ operators. For $\hat{q}$ and $\hat{p}$ it also possible to derive the variances, $\sigma^2[\hat{q}]$ and $\sigma^2[\hat{p}]$, and to estimate the squeezing parameter,

$$\xi = \frac{1}{4} \ln\left(\sigma^2_{\hat{p}} / \sigma^2_{\hat{q}}\right)\;. \tag{3.43}$$

The results are summarized in Table 3.1. For the errors evaluation we have used the standard expression for the mean average error relative to a data set (X_ℓ, Φ_ℓ) (recall the definitions in (3.39) and (3.40)),

$$\epsilon_{\hat{O}} = \sqrt{\frac{\sum_{i=1}^{n} \left[R^{h,\eta}_{\hat{O}}(X_\ell;\Phi_\ell) - E_{\hat{O}}\right]^2}{n(n-1)}}\;. \tag{3.44}$$

Table 3.1: Estimate of different expectation values from simulated data. Estimate for $n = 8\times10^4$ simulated quadratures associated to the coherent state ($\alpha = 3$) and the displaced-squeezed state ($\alpha = 3$, $\xi = 0.8$).

$\hat{O}$	$\langle\hat{O}\rangle_{D(\alpha)\|0\rangle}$	$E^h_{\hat{O}}$	$\langle\hat{O}\rangle_{D(\alpha)S(\xi)\|0\rangle}$	$E^h_{\hat{O}}$
$\hat{n}$	9	9 ± 1	9.89	9.9 ± 0.8
$\hat{q}$	4.24	4.2 ± 0.5	4.24	4.3 ± 0.3
$\hat{p}$	0	0.00 ± 0.06	0	0.0 ± 0.2
$\sigma^2_{\hat{q}}$	0.5	0.4 ± 0.2	0.1	0.1 ± 0.2
$\sigma^2_{\hat{p}}$	0.5	0.5 ± 0.2	2.48	2.3 ± 0.4
ξ	0	0.0 ± 0.1	0.8	0.78 ± 0.02

The averages computed using the Wigner function estimated from the data set fully agree with those analytically calculated from the known quantum states. In particular, even the estimated value of the squeezing parameter agrees with the

expected one. This reveals that the minimax reconstruction method is effective in discriminating different quantum states even under low efficiency conditions.

The real data in Fig 3.8 can now be treated in the same way. In this case, the collected homodyne traces are two coherent states with very different mean photon number. The first step in the reconstruction procedure and determination of relevant observables is to use the estimator in (3.30) to obtain the Wigner functions associated with the two states. The results are shown in Fig 3.10; as in the previous numerical experiments, in order to minimize artifacts related to the numerical integration in (3.31), a low pass Gaussian filter has been applied to the raw images. With these results, one can then estimate the mean values of relevant observables,

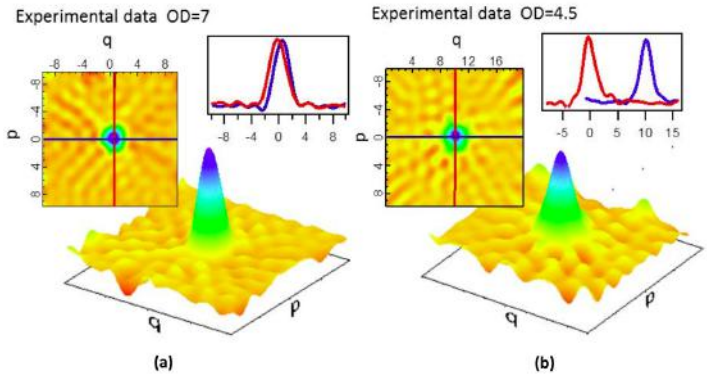

Figure 3.10: Reconstructed Wigner function from experimental data using the adaptive minimax estimation. Reconstruction from $n = 8 \times 10^4$ quadratures of attenuated laser states with (a) $OD = 4.5$ and (b) $OD = 7$. The insets show representative two-dimensional cuts of the reconstructed Wigner function.

as number, position and momentum operators together with the squeezing parameter, obtained from the computation of the variances of position and momentum. The results are summarized in Table 3.2. The obtained expectation values for the number operator explicitly exhibit the three order of magnitude difference between the two states. Furthermore, these results show that the analyzed experimental states are indeed minimum uncertainty states, with vanishing squeezing parameter.

These results demonstrate the effectiveness of the minimax statistical techniques in the reconstruction of Gaussian quantum states of light in presence of large electronic noise.

These methods allow to circumvent convergence problems that arise when using pattern function methods in estimating observable averages with low detection efficiency, namely $\eta < 50\%$[12–19,37]. Nevertheless, it is interesting to investigate the possible relations between these two approaches, by replacing the cutoff truncation in the integration with respect to ξ in 3.31 with a suitable Gaussian regularization. In particular we consider the following alternate kernel functions instead of

Table 3.2: Estimate of different expectation values form experimental data. Estimate for the experimental coherent states with optical density $OD = 4.5$ and $OD = 7$, respectively.

$\hat{O}$	$E^h_{\hat{O}}$ $(OD = 4.5)$	$E^h_{\hat{O}}$ $(OD = 7)$
$\hat{n}$	51 ± 7	0.2 ± 0.3
$\hat{q}$	10 ± 1	0.7 ± 0.2
$\hat{p}$	0.1 ± 0.2	0.0 ± 0.2
$\sigma^2_{\hat{q}}$	0.7 ± 0.3	0.5 ± 0.2
$\sigma^2_{\hat{p}}$	0.6 ± 0.3	0.5 ± 0.3
ξ	0.0 ± 0.2	0.0 ± 0.2

$R^{h,\eta}_{\hat{O}}(X_\ell, \Phi_\ell)$,

$$R^{\varepsilon}_{\hat{O}}(X_\ell, \Phi_\ell) = \int_{\mathbb{R}^2} dq\, dp\, \hat{O}(q,p)\, e^{-\varepsilon(q^2+p^2)} \int_{-\infty}^{+\infty} d\xi \frac{|\xi|}{4\pi} e^{-\imath\xi(q\cos\Phi_\ell + p\sin\Phi_\ell - \frac{X_\ell}{\sqrt{\eta}})}\, e^{\xi^2 \frac{1-\eta}{4\eta}}\ , \tag{3.45}$$

where ε is a positive regularization parameter. In principle, this allows for a more direct estimate of the expectation values of any observable, provided $0 < \varepsilon < \eta/(1-\eta)$. For instance, in the case of position, momentum and number operators, one finds:

$$R^{\varepsilon}_{\hat{q}}(X_\ell, \Phi_\ell) = \int_{-\infty}^{+\infty} d\xi \frac{\cos\Phi_\ell}{8\varepsilon^2}\, \xi\, |\xi| \sin\Big(\frac{\xi\, X_\ell}{\sqrt{\eta}}\Big)\, e^{-\xi^2 \frac{\eta-\varepsilon(1-\eta)}{4\eta\varepsilon}}\ , \tag{3.46}$$

$$R^{\varepsilon}_{\hat{p}}(X_\ell, \Phi_\ell) = \int_{-\infty}^{+\infty} d\xi \frac{\sin\Phi_\ell}{8\varepsilon^2}\, \xi\, |\xi|\, \sin\Big(\frac{\xi\, X_\ell}{\sqrt{\eta}}\Big)\, e^{-\xi^2 \frac{\eta-\varepsilon(1-\eta)}{4\eta\varepsilon}}\ , \tag{3.47}$$

$$R^{\varepsilon}_{\hat{n}}(X_\ell, \Phi_\ell) = \int_{-\infty}^{+\infty} d\xi \frac{1}{32\varepsilon^3}\, |\xi|\, \cos\Big(\frac{\xi\, X_\ell}{\sqrt{\eta}}\Big)\, e^{-\xi^2 \frac{\eta-\varepsilon(1-\eta)}{4\eta\varepsilon}} [4\varepsilon(1-\varepsilon) - \xi^2]\ . \tag{3.48}$$

Notice that these quantities converge to functions $R^0_{\hat{O}}(X_\ell, \Phi_\ell)$ in the limit $\varepsilon \to 0$:

$$R^0_{\hat{q}}(X_\ell, \Phi_\ell) = \frac{2}{\sqrt{\eta}} X_\ell \cos\Phi_\ell\ , \tag{3.49}$$

$$R^0_{\hat{p}}(X_\ell, \Phi_\ell) = \frac{2}{\sqrt{\eta}} X_\ell \sin\Phi_\ell\ , \tag{3.50}$$

$$R^0_{\hat{n}}(X_\ell, \Phi_\ell) = \Big(\frac{X_\ell}{\sqrt{\eta}}\Big)^2 - \frac{1}{2\eta}\ . \tag{3.51}$$

These expressions coincide with the so-called kernel functions of the standard pattern function based tomographic techniques[37]. Unfortunately, the limit $\varepsilon \to 0$ can not be taken in the case of more general observables with higher powers of $\hat{q}$ and

$\hat{p}$ since the integrals diverge as powers of $1/\varepsilon$. This fact may be related to the mentioned convergence problems of the standard pattern function method. It is important to note that the estimation of the mean values of $\hat{q}$, $\hat{p}$ and $\hat{n}$ through the use of the limit kernel functions (3.49)-(3.51) is not sufficient to completely characterize any quantum states, like coherent and squeezed states.

In conclusion, we reported the characterization of a time domain balanced homodyne detection apparatus operating in presence of large electronic noise corresponding to an overall detection efficiency $\eta = 0.31$. We used the detector combined with tomographic reconstruction techniques for discriminating between different quantum states of light. A minimax adaptive reconstruction of the Wigner function has been adopted. This approach allows us to circumvent possible convergence problems arising from low detector efficiency in the standard pattern function based quantum tomography. The effectiveness of such a method has been verified in two ways. At first, we calculated the Wigner function for simulated data of coherent and squeezed states and, then, for real experimental homodyne data of coherent states with different mean photon numbers. In all cases it is proved that it is possible to efficiently reconstruct the associated Wigner function, asserting the Gaussian character of the quantum states, and evaluating their relevant parameters. The present study demonstrates that even low efficient ($\sim 30\%$) homodyne detectors can be usefully employed to study the nature of quantum states of light provided that non-standard statistical tools as the minimax methods are used to reconstruct their Wigner functions. These results may be important whenever quantum optics techniques are employed to investigate the dynamics of out of equilibrium states and the presence of quantum coherence in condensed matter.

We stress that the experimental detection-acquisition system presented here has been developed at the beginning of this PhD project by using commercial available components. The latter are characterized by a low efficiency detection that we compensated with suitable data processing algorithms. In the course of the PhD project we improved the detection-acquisition system by designing and realizing a custom highly efficient differential detector. The latter is reported in the Appendix A of the thesis.

3.5 Quantum interference reconstruction with low homodyne efficiency

In the previous section we considered the issue of reconstructing Gaussian states. We here show that even non Gaussian states can be efficiently reconstructed in noisy conditions. In particular, we report our results about quantum interferences reconstruction in low homodyne efficiency conditions[33].

We address again the problem of the existence or not of a lower homodyne efficiency bound ($\eta = 0.5$), under which quantum state reconstruction is not achievable[12–22,31]. While in the previous section we considered the specific case of quantum Gaussian states (characterized by Wigner functions of Gaussian type), here we focus on the reconstruction of purely quantum proprieties like quantum interference effects that typically spoil positivity of the Wigner function. These effects

have been claimed not to be accessible by homodyne reconstruction in presence of efficiency lower than 0.5 [13,17]. However, in [21] it is theoretically shown that $\eta < 1/2$ only requires increasingly larger data sets for achieving small reconstruction errors. To the best of our knowledge, this claim was not put to test in those studies as the values of η in the considered numerical experiments were close to 1.

In order to pave the way for quantum state reconstruction in high noise conditions, we consider here values $\eta < 0.5$ and reconstruct the Wigner function of the following superposition of coherent states

$$|\Psi_\alpha\rangle = \frac{|\alpha\rangle + |-\alpha\rangle}{\sqrt{2\left(1+\mathrm{e}^{-2|\alpha|^2}\right)}}\ , \qquad |\alpha\rangle = \mathrm{e}^{-|\alpha|^2/2}\,\mathrm{e}^{\alpha\, a^\dagger}\ |0\rangle\ , \tag{3.52}$$

with α any complex number $\alpha_1 + i\alpha_2 \in \mathbb{C}$. Such a state is usually called "Schrödinger's cat" state. The Wigner function corresponding to the pure state $\hat{\rho}_\alpha = |\Psi_\alpha\rangle\langle\Psi_\alpha|$ is shown in Fig 3.11 for $\alpha \in \mathbb{R}$. The analytic expressions for the Wigner function

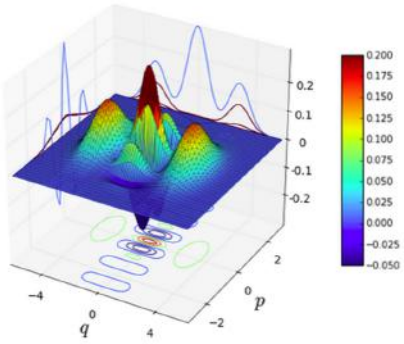

Figure 3.11: Wigner function of a "Schrödinger's cat" state. The represented Wigner function corresponds to the pure state $\hat{\rho}_\alpha = |\Psi_\alpha\rangle\langle\Psi_\alpha|$ ($\alpha_1 = 3/\sqrt{2}$; $\alpha_2 = 0$)

and its Fourier transform are the following,

$$W_\alpha(q,p) = \frac{1}{2\pi\left(1+\mathrm{e}^{-2|\alpha|^2}\right)}\left(\mathrm{e}^{-(q-\sqrt{2}\alpha_1)^2-(p-\sqrt{2}\alpha_2)^2} + \mathrm{e}^{-(q+\sqrt{2}\alpha_1)^2-(p+\sqrt{2}\alpha_2)^2} + 2\,\mathrm{e}^{-q^2-p^2}\cos\left(2\sqrt{2}(q\alpha_2+p\alpha_1)\right)\right)\ , \tag{3.53}$$

$$F[W_\alpha](w_1,w_2) = \frac{1}{2\left(1+\mathrm{e}^{-2|\alpha|^2}\right)}\left(\mathrm{e}^{-\frac{(w_1+2\sqrt{2}\alpha_2)^2+(w_2-2\sqrt{2}\alpha_1)^2)}{4}} + \mathrm{e}^{-\frac{(w_1-2\sqrt{2}\alpha_2)^2+(w_2+2\sqrt{2}\alpha_1)^2)}{4}} + 2\,\mathrm{e}^{-\frac{w_1^2+w_2^2}{4}}\cos\left(\sqrt{2}(w_1\alpha_1+w_2\alpha_2)\right)\right)\ . \tag{3.54}$$

For a generic Wigner function $W_\rho(q,p)$ one computes the quadrature probability

density $p_\rho(x,\phi)$ in (3.21) by means of the so-called Radon transform:

$$\langle x|\hat{\rho}|x\rangle = \int_{\mathbb{R}} \mathrm{d}p\, W_\rho(x\cos\phi - p\sin\phi, x\sin\phi + p\cos\phi)\ . \tag{3.55}$$

It follows that the probability density $p_\rho(x,\phi)$ and the noise-affected probability density $p^\eta_\rho(x,\phi)$ in (3.26) are given by:

$$\begin{aligned} p_\alpha(x,\phi) \quad = \quad & \frac{1}{2\sqrt{\pi}\left(1+\mathrm{e}^{-2|\alpha|^2}\right)}\left(\mathrm{e}^{-(x-\sqrt{2}\alpha(\phi))^2} + \mathrm{e}^{-(x+2\sqrt{2}\alpha(\phi))^2}\right. \\ & \left. + \mathrm{e}^{-x^2-2\alpha^2(-\phi)}\, 2\cos\left(2\sqrt{2}x\beta(-\phi)\right)\right)\ ; \end{aligned} \tag{3.56}$$

$$\begin{aligned} p^\eta_\alpha(x,\phi) \quad = \quad & \frac{1}{2\sqrt{\pi}\left(1+\mathrm{e}^{-2|\alpha|^2}\right)}\left(\mathrm{e}^{-(x-\sqrt{2\eta}\alpha(\phi))^2} + \mathrm{e}^{-(x-\sqrt{2\eta}\alpha(\phi))^2}\right. \\ & \left. + 2\,\mathrm{e}^{-x^2-2|\alpha|^2+2\eta|\beta(-\phi)|^2}\,\cos\left(2\sqrt{2\eta}x\beta(-\phi)\right)\right)\ , \end{aligned} \tag{3.57}$$

where

$$\alpha(\phi) = \alpha_1\cos\phi + \alpha_2\sin\phi\ , \qquad \beta(\phi) = \alpha_2\cos\phi - \alpha_1\sin\phi\ .$$

Once known the expression for the noisy-affected probability distribution, we generated $M = 10$ samples of $n = 16\times 10^6$ quadrature data (X_ℓ, Φ_ℓ) distributed according to the (3.57), namely by considering an efficiency ($\eta = 0.45$). Starting from each set of simulated quadrature data we reconstructed the associated Wigner function by means of (3.29) and (3.31). In this case we adopted a deeper analysis for the choice of optimal value of the parameter h and r in (3.29) and (3.31). We provided a derivation of the L^2-errors and of the optimal dependence of h and r on the number of data n and on a parameter β that takes into account the fast decay of both the Wigner function and its Fourier transform for large values of their arguments. The following upper bound to the mean square error in (3.32) is derived:

$$\Delta^{\eta,r}_{h,n}(\hat{\rho}_\alpha) \le \Delta\ , \qquad \Delta = \frac{r^2}{n\,h}\,\mathrm{e}^{2\gamma/h^2}\,\Delta_1(\gamma) + \mathrm{e}^{-\beta r^2}\,\Delta_2(\beta) + \mathrm{e}^{-\beta/h^2}\,\Delta_3(\beta)\ , \tag{3.58}$$

with $0<\beta<1/4$ and γ as given in (3.27). The quantities $\Delta_{1,2,3}$ do not depend on h, r and n and will be discussed in detail afterwards. The key point of this analysis is that by taking the derivatives with respect to r and h, one finds that the upper bound to the mean square deviation is minimised, for large n, by choosing

$$r = \frac{1}{h} = \sqrt{\frac{\log n}{\beta + 2\gamma}}\ . \tag{3.59}$$

The complete derivation of this result and the discussion about the rose of the extra parameter β is reported in Appendix A. We now report the results of the Wigner function reconstruction using the condition in (3.59) for the free parameters.

The averaged reconstructed Wigner functions $E\left[W_{h,n}^{\eta,r}(q,p)\right]$ for $\eta = 0.45$ over $M = 10$ simulated experimental data set are shown in Fig 3.12 for two different values of the parameter β. The mean square error of the reconstructed Wigner

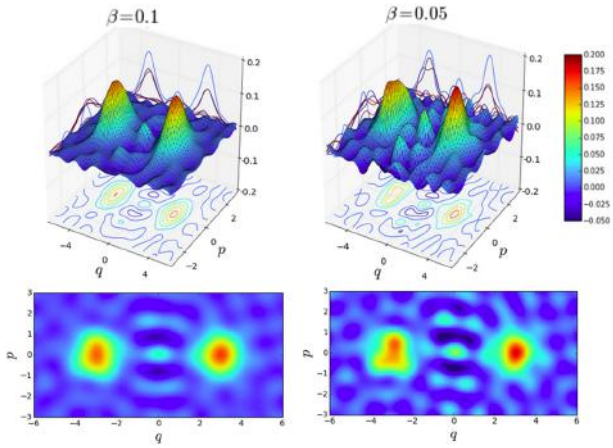

Figure 3.12: Averaged reconstructed Wigner functions. $E\left[W_{h,n}^{\eta,r}(q,p)\right]$ over $M = 10$ samples of $n = 16 \times 10^6$ noisy quadrature data (efficiency $\eta = 0.45$). Two different values of β are considered.

functions has been computed as in (3.32) and compared with the mathematically predicted upper bounds Δ. The dependence of the upper bound reconstruction error from the parameter β is discussed afterwards. In the following table 3.3, we compare the reconstruction errors $\Delta_{h,n}^{\eta,r}(\hat{\rho})$ with their upper bound Δ for two significant values of β. One can notice the interference features clearly appear

β	$\Delta_{h,n}^{\eta,r}(\hat{\rho})$	Δ
0.05	0.081	2.39
0.1	0.076	26.07

Table 3.3: Calculated reconstruction errors. $\Delta_{h,n}^{\eta,r}(\hat{\rho})$ for $M = 10$ samples of noisy quadrature data ($\eta = 0.45$) for two different values of β. Comparison with the mathematical prediction of the upper bound Δ.

in the reconstructed Wigner function also for efficiencies lower than 50% and the reconstruction errors are compatible with the theoretical predictions. In the next subsection, we make a quantitative study of the visibility of the interference effects.

3.5.1 Witnessing the interference terms

The interference effects in the state $|\Psi_\alpha\rangle$ can be witnessed by an observable $\hat{O}_\alpha$ of the form

$$\hat{O}_\alpha = \frac{|\alpha\rangle\langle -\alpha| \, + \, |-\alpha\rangle\langle\alpha|}{2\left(1+\mathrm{e}^{-2|\alpha|^2}\right)} \, . \tag{3.60}$$

With respect to an incoherent mixture of the two coherent states,

$$\hat{\rho}_{\alpha\lambda} = \lambda\,|\alpha\rangle\langle\alpha| \, + \, (1-\lambda)\,|-\alpha\rangle\langle -\alpha| \, , \qquad 0 \leq \lambda \leq 1 \, , \tag{3.61}$$

its mean value is given by

$$\mathrm{Tr}\Big(\hat{\rho}_{\alpha\lambda}\,\hat{O}_\alpha\Big) = \frac{\mathrm{e}^{-2|\alpha|^2}}{1+\mathrm{e}^{-2|\alpha|^2}} \, . \tag{3.62}$$

Therefore, from (2.9) it follows that the phase-space function $O_\alpha(q,p)$ associated to $\hat{O}_\alpha$ is

$$O_\alpha(q,p) = \frac{\mathrm{e}^{-q^2-p^2}\,\cos\left(2\sqrt{2}(q\alpha_2+p\alpha_1)\right)}{\sqrt{\pi}\left(1+\mathrm{e}^{-2|\alpha|^2}\right)} \, , \qquad \alpha = \alpha_1 + i\alpha_2. \tag{3.63}$$

Let us denote by $W^{\alpha}_{j,rec}(q,p)$, the estimated Wigner function $W^{\eta,r}_{h,n}(q,p)$ in (3.29) for the $j-th$ set of collected quadrature data. It yields a reconstructed mean value

$$< \hat{O}_\alpha >_{j,rec} = \int_{\mathbb{R}^2} \mathrm{d}q\,\mathrm{d}p\, O_\alpha(q,p)\, W^{\alpha}_{j,rec}(q,p) \, , \tag{3.64}$$

of which one can compute mean, $\mathrm{Av}(< \hat{O}_\alpha >_{rec})$, and standard deviation, $\mathrm{Sd}(< \hat{O}_\alpha >_{rec})$, with respect to the M sets of collected data:

$$\mathrm{Av}(< \hat{O}_\alpha >_{rec}) = \frac{1}{M}\sum_{j=1}^{M} < \hat{O}_\alpha >_{j,rec} \, , \tag{3.65}$$

$$\mathrm{Sd}(< \hat{O}_\alpha >_{rec}) = \sqrt{\frac{1}{M}\sum_{j=1}^{M}\left(\Big(< \hat{O}_\alpha >_{j,rec}\Big)^2 - \Big(\mathrm{Av}(< \hat{O}_\alpha >_{rec}\Big)^2\right)} \, . \tag{3.66}$$

We computed $\mathrm{Av}(< \hat{O}_\alpha >_{rec})$ and $\mathrm{Sd}(< \hat{O}_\alpha >_{rec})$ with $M = 10$ simulated sets of noisy data with $\eta = 0.45$ for two different numbers of simulated quadrature data (see the caption in Fig 3.13). We repeated the procedure for different values of the parameter β. The results are presented in Fig. 3.13, where the error bars represent the computed $\mathrm{Sd}(< \hat{O}_\alpha >_{rec})$.

In order to be compatible with the interference term present in $|\Psi_\alpha\rangle$, the reconstructed Wigner functions should yield an average incompatible with the incoherent

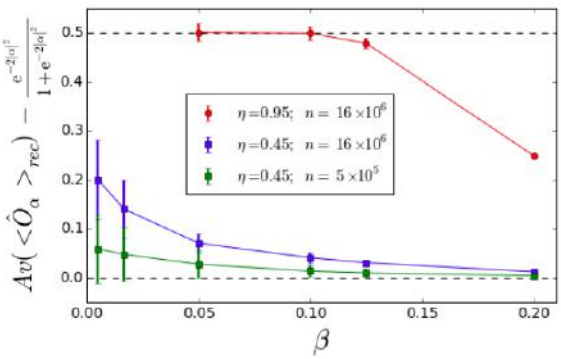

Figure 3.13: Study of the visibility of the reconstructed interference features. $\mathrm{Av}(<\hat{O}_\alpha>_{rec}) - \frac{e^{-2|\alpha|^2}}{1+e^{-2|\alpha|^2}}$ as a function of β. The error bars represent $\mathrm{Sd}\ (\ <\hat{O}_\alpha>_{rec}\ )$. For each β, $M = 10$ set of n noisy quadrature data have been considered. The square markers refer to $\eta = 0.45$ ($n = 16\times10^6$ blue marker and $n = 5\times10^5$ green markers) while the round ones refer to $\eta = 0.95$ ($n = 16\times10^6$). The error bars for $\eta = 0.95$ have been multiplied by 20 in order to make them more visible.

mean value in (3.62), namely such that

$$\left|\mathrm{Av}(<\hat{O}_\alpha>_{rec}) - \frac{e^{-2|\alpha|^2}}{1+e^{-2|\alpha|^2}}\right| > \mathrm{Sd}(<\hat{O}_\alpha>_{rec})\ . \tag{3.67}$$

We thus see that the condition in (3.67) is verified for $\eta = 0.45$, that is the reconstructed Wigner functions are not compatible with incoherent superpositions of coherent states, if enough data are considered. We also notice that the same behavior is valid for the high efficiency $\eta = 0.95$.

The dependence of the errors on β can be understood as follows: when β decreases the integration interval in (3.31) becomes larger and approaches the exact interval $[-\infty, +\infty]$. Nevertheless this occurs at the price of increasing the reconstruction error. This can be noted both in Fig 3.13 (larger error bars) and in Fig 3.12 (increasingly noisy effects in the reconstructed Wigner function). This problem can be overcome with a larger number of data samples M, that would reduce the reconstruction noise and compensate the effect of decreasing β.

In conclusion we have numerically shown that quantum interference effects can be reconstructed by means of homodyne tomography also in low efficiency conditions. In particular, we simulated quadrature data affected by high electronic noise associated with a detection efficiency lower than 50% and, based on the tomographic techniques developed in[21], we reconstructed the Wigner function of a linear superposition of two coherent states. Then, taking into account the decay properties of the Wigner function and its Fourier transform, we have checked that the reconstruction errors conform with the theoretical error bounds computed via L^2 norms. In order to clearly exhibit the interference effects, both qualitatively in the graphic reconstruction of the Wigner function, and quantitatively in the

variance of an interference witness, larger sets of homodyne data are necessary as the detection efficiency gets smaller.

The mathematical derivation for the optimal free parameters values is reported in Appendix B of the thesis.

References

[1] Lvovsky and Raymer. Continuous-variable optical quantum-state tomography. *REVIEWS OF MODERN PHYSICS*, 81(1):299, January-March 2009.

[2] D. T. Smithey, M. Beck, M. G. Raymer, and A. Faridani. Measurement of the wigner distribution and the density matrix of a light mode using optical homodyne tomography: Application to squeezed states and the vacuum. *Phys. Rev. A*, 70:1244, 1993.

[3] I. A. Walmsley. Quantum optics: Science and technology in a new light. *Science*, 348:525–530, 2015.

[4] M. Paris and J. Řeháček. *Quantum States Estimation*. Lecture notes in Physics vol 649 Springer, Berlin, 2004.

[5] U. Fano. Description of states in quantum mechanics by density matrix and operator techniques. *Reviews of Modern Physics*, 29(1):74, 1957. Sec. 6.

[6] Robin Blume-Kohout. Optimal, reliable estimation of quantum states. *New Journal of Physics*, 12(4):043034, 2010. URL http://stacks.iop.org/1367-2630/12/i=4/a=043034.

[7] K. Vogel and H. Risken. Determination of quasiprobability distributions in terms of probability distributions for the rotated quadrature phase. *Phys. Rev. A*, 40:2847, 1989.

[8] Welsch, Vogel, and Opatrny. Homodyne detection and quantum state reconstruction. *Progress in Optics*, 39:63–211, 1999.

[9] S. Olivares A. Ferraro and M.G.A. Paris. *Gaussian states in quantum information*. Bibiopolis, Napoli, 2005.

[10] M.A. Nielsen and I.L. Chuang. *Quantum Computation and Quantum Information*. Cambridge University Press, Cambridge, 2010.

[11] U. Leonhardt and H. Paul. High-accuracy optical homodyne detection with low-efficiency detectors: "preamplification" from antisqueezing. *Phys. Rev. Lett.*, 72:4086–4089, Jun 1994. doi: 10.1103/PhysRevLett.72.4086. URL http://link.aps.org/doi/10.1103/PhysRevLett.72.4086.

[12] U. Herzog T. Kiss and U. Leonhardt. Compensation of losses in photodetection and in quantum-state measurements. *Phys. Rev. A*, 52:2433, 1995.

[13] G. M. D'Ariano, U. Leonhardt, and H. Paul. Homodyne detection of the density matrix of the radiation field. *Phys. Rev. A*, 52:R1801–R1804, Sep 1995. doi: 10.1103/PhysRevA.52.R1801. URL http://link.aps.org/doi/10.1103/PhysRevA.52.R1801.

[14] Z. Hradil. Quantum-state estimation. *Phys. Rev. A*, 55:R1561–R1564, Mar 1997. doi: 10.1103/PhysRevA.55.R1561. URL http://link.aps.org/doi/10.1103/PhysRevA.55.R1561.

[15] U. Herzog. Loss-error compensation in quantum-state measurements and the solution of the time-reversed damping equation. *Phys. Rev. A*, 53:1245, 1996.

[16] Giacomo M. D'Ariano and Matteo G. A. Paris. Adaptive quantum homodyne tomography. *Phys. Rev. A*, 60:518–528, Jul 1999. doi: 10.1103/PhysRevA.60.518. URL http://link.aps.org/doi/10.1103/PhysRevA.60.518.

[17] G.M. D'Ariano and C. Macchiavello. Loss-error compensation in quantum-state measurements. *Phys. Rev. A*, 57:3131, 1998.

[18] U. Herzog T. Kiss and U. Leonhardt. Reply to "loss-error compensation in quantum-state measurements. *Phys. Rev. A*, 57:3134, 1998.

[19] T. Richter. Realistic pattern functions for optical homodyne tomography and determination of specific expectation values. *Phys. Rev. A*, 61:063819, 2000.

[20] Appel, Hoffman, Figueroa, and Lvovsky. Electronic noise in optical homodyne tomography. *Physical Review A*, 75(3):035802, 2007.

[21] M. Guta C. Butucea and L. Artiles. Minimax and adaptive estimation of the wigner function in quantum homodyne tomography with noisy data. *Ann. Stat.*, 35:465, 2007.

[22] C. Butucea J.-M. Aubry and K. Meziani. State estimation in quantum homodyne tomography with noisy data. *Inv. Problems*, 25:015003, 2009.

[23] M. Esposito. Design and experimental realization of a pulsed homodyne detector for optical quantum states characterization, 2012. URL https://sites.google.com/site/danielefausti/educational-materials.

[24] Hansen, Aichele, Hettich, Lodahl, Lvovsky, Mlynek, and Schiller. An ultrasensitive pulsed balanced homodyne detector: Application to time-domain quantum measurements. *OPTICS LETTERS*, 26(21):1714, November 2001.

[25] Zavatta, Bellini, Ramazza, Marin, and Arecchi. Time-domain analysis of quantum states of light: noise characterization and homodyne tomography. *J. Opt. Soc. Am. B*, 19(5):1189, May 2002.

[26] R. Kumar, E. Barrios, A. MacRae, E. Cairns, E.H. Huntington, and A.I. Lvovsky. Versatile wideband balanced detector for quantum optical homodyne

tomography. *Optics Communications*, 285(24):5259 – 5267, 2012. ISSN 0030-4018. doi: http://dx.doi.org/10.1016/j.optcom.2012.07.103. URL http://www.sciencedirect.com/science/article/pii/S0030401812008255.

[27] Haderka, Michálek, Urbášek, and Ježek. Fast time-domain balanced homodyne detection of light. *Applied Optics*, 48(15):2884–2889, 2009.

[28] Cooper, Soller, and Smith. High-stability time-domain balanced homodyne detector for ultrafast optical pulse applications. *J. Mod. Opt.*, 60:611, 2013.

[29] Chi, Qi, Zhu, Qian, Lo, Youn, Lvovsky, and Tian. A balanced homodyne detector for high-rate gaussian-modulated coherent-state quantum key distribution. *New Journal of Physics*, 13:013003, 2011. Section 4.5.

[30] Okubo, Hirano, Zhang, and Hirano. Pulse-resolved measurement of quadrature phase amplitudes of squeezed pulse trains at a repetition rate of 76 mhz. *Opt. Lett.*, 33:1458–1460, 2008.

[31] M. Esposito, F. Benatti, R. Floreanini, S. Olivares, F. Randi, K. Titimbo, M. Pividori, F. Novelli, F. Cilento, F. Parmigiani, and D. Fausti. Pulsed homodyne gaussian quantum tomography with low detection efficiency. *New Journal of Physics*, 16(4):043004, 2014. URL http://stacks.iop.org/1367-2630/16/i=4/a=043004.

[32] Leonhardt and Paul. Measuring the quantum state of light. *Prog. Quant. Electr.*, 19:84–130, 1995.

[33] M. Esposito, F. Randi, K. Titimbo, K. Zimmermann, G. Kourousias, A. Curri, R. Floreanini, F. Parmigiani, D. Fausti, and F. Benatti. Quantum interferences reconstruction with low homodyne detection efficiency. 2015. URL http://arxiv.org/abs/1508.07799.

[34] Zavatta, Viciani, and Bellini. Non-classical field characterization by high-frequency,time-domain quantum homodyne tomography. *Laser Phys. Lett.*, 3 (1):3–16, 2006.

[35] G. Garrett, A. Rojo, A. Sood, J. Whitaker, and R. Merlin. Vacuum Squeezing of Solids: Macroscopic Quantum States Driven by Light Pulses. *Science*, 275(5306):1638–1640, 1997. doi: 10.1126/science.275.5306.1638. URL http://dx.doi.org/10.1126/science.275.5306.1638.

[36] Hans A. Bachor and Timothy C. Ralph. *A Guide to experiments in Quantum Optics*. WILEY-VCH, 2004.

[37] D'Ariano, Paris, and Sacchi. Quantum tomography. *Advances in Imaging and Electron Physics*, 128:205–308, 2003.

4

Non-equilibrium photon number quantum statistics

Fluctuations of the atomic positions are at the core of a large class of unusual material properties ranging from quantum para-electricity to high temperature superconductivity. Their measurement in solids is the subject of an intense scientific debate focused on seeking a methodology capable of establishing a direct link between the variance of the atomic displacements and experimentally measurable observables. In this Chapter we address this issue by means of non-equilibrium optical experiments performed in shot-noise limited regime. The variance of the time dependent atomic positions and momenta is directly mapped into the quantum fluctuations of the photon number of the scattered probing light. The fully quantum description of the non-linear phonon-photon interaction, presented in Section 2.6, is benchmarked by unveiling the squeezing of thermal phonons in α-quartz.

4.1 Introduction

The time evolution of atomic positions in materials is usually addressed by means of non-equilibrium optical spectroscopy. An ultrashort light pulse (the pump) impulsively perturbs the lattice and a second one (the probe), properly delayed in time, measures a response that is proportional to the spatially-averaged instantaneous atomic positions. In those experiments, the time dependent atomic displacements are often revealed by an oscillating optical response at frequencies characteristic of the vibrational modes of the material. The latter is commonly dubbed with

the improper expression of *coherent phonon** response[1–11]. In this framework, it has been shown that a non-linear light-matter interaction can prepare non classical vibrational states[12,13] such as squeezed states, where the fluctuations of the lattice position (or momentum) can fall below the thermal limit. A reduction below the vacuum limit is known as vacuum squeezing[14].

Here we propose a joint experimental and theoretical approach to access the fluctuations of the atomic positions in time domain studies. An experimental apparatus that allows for the measurement of the photon number quantum fluctuations of the scattered probe pulses in a pump and probe setup is adopted. The connection between the measured photon number uncertainty and the fluctuations of the atomic positions is given by a fully quantum mechanical theoretical description of the time domain process. Overall we prove that, under appropriate experimental conditions, the fluctuations of the lattice displacements can be directly linked to the photon number quantum fluctuations of the scattered probe pulses. Our methodology, that combines non-linear spectroscopic techniques with a quantum description of the electromagnetic fields, is benchmarked on the measurement of phonon squeezing in α-quartz[15].

This Chapter is organized as follows,

- The impulsive excitation of Raman active vibrational modes in a crystal of quartz is described and some preliminary standard pump-probe experiments are reported (Section 4.2).
- The shot-noise limited pump-probe experiments are described and the experimental results about the photon number statistics to uncover the atomic fluctuations are shown (Section 4.3).
- The comparison with the fully quantum model presented in Section 2.7 is reported (Section 4.4).

4.2 Stimulated Raman scattering on α-quartz

Quartz can be considered as a benchmark material for the dynamic excitation of phonons via stimulated Raman scattering and it represents the ideal playground to test our approach to study atomic quantum fluctuations. Quartz undergoes a phase change at about 848 K. The low-temperature phase, with trigonal symmetry, is called α-quartz while the high-temperature phase, with hexagonal symmetry, β-quartz. Here we investigate the case of α-quartz. The latter has a trigonal crystal structure with D_3 symmetry and $N = 9$ atoms per unit cell (see Fig 4.1 (a)). Group-theory calculations show that the $3 \times N = 27$ degrees of freedom are divided into 2 acoustic vibrations of $A_2 + E$ symmetry and 16 optical vibrations of $4A_1 + 4A_2 + 8E$ symmetry[17]. In particular, the quartz Raman-active vibrational modes are are 4 totally symmetric modes of species A_1, and 8 doubly degenerate

*The term *coherent* in this context indicates a the temporal periodicity of the material response but does not imply the photo-excited vibrational mode to be in a coherent state of the quantum harmonic oscillator.

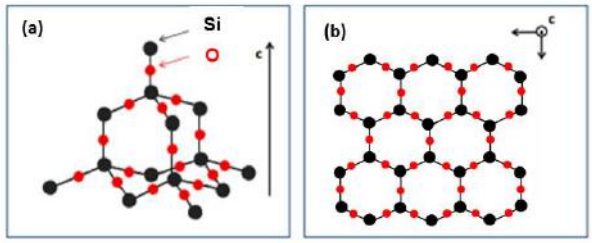

Figure 4.1: Atomic arrangement in quartz. (a) Crystal structure of α-quartz[16] and (b) its projection on the plane perpendicular to the c-axis.

modes of species E. In Fig. 4.2 the Raman spectra of *alpha*-quartz are reported[17].

Impulsive stimulated Raman scattering (ISRS) is a non resonant excitation mechanism of lattice vibrations in transparent materials by ultrashort laser pulses. As reported in Section 2.6, it is a four-wave mixing process due to third order polarization effects. The Cartesian components of the third order non-linear polarization are given by

$$P_i^{(3)}(\omega) = \sum_{jkl} \chi_{ijkl}^{(3)} \left[\mathcal{E}_1(\omega_1)\right]_j \left[\mathcal{E}_2(\omega_2)\right]_k \left[\mathcal{E}_3(\omega_3)\right]_l, \tag{4.1}$$

where $\chi_{ijkl}^{(3)}$ is the susceptibility tensor, $\mathcal{E}_1$ is the probe field and $\mathcal{E}_2$ and $\mathcal{E}_3$ are the pump fields. In conventional two pulses pump and probe experiments, the fields $\mathcal{E}_2(\omega_2)$ and $\mathcal{E}_3(\omega_3)$ are two different frequency components of the pump laser pulse. In particular, all photon pairs such that $\omega_3 - \omega_2 = \Omega$, where Ω is the frequency of the Raman active vibrational mode, contribute to ISRS[18]. The interaction of the probe field $\mathcal{E}_1(\omega_1)$ with the photo-excited material induces an emitted field, $\mathcal{E}_{\mathrm{EF}}(\omega)$ which depends on the pump-probe delay and carries information about the specific Raman mode excited in the crystal. In our experiments, the sample is a 1 mm thick α-quartz, oriented in order to have the principal symmetry axis parallel to the probe propagation direction. A scheme of the chosen experimental geometry is shown in Fig 4.3.
The probe propagates parallel to the c-axis of the crystal which corresponds to z-axis in our coordinates system. In this configuration, the only accessible vibrational modes are those of a system with C_3 rotational symmetry (with the c-axis as principal axis) such as a triatomic molecule with 3 atoms at the corner of an equilateral triangle. The normal vibrational modes for such kind of system are illustrated in Fig. 4.4. They consist of the A_1 breathing mode and two degenerate E-symmetry modes. The excited phonon state is detected via the scattering of the probe pulse which arrives on the sample with time delay τ with respect to the pump. The transmitted light undergoes a polarization selection through a polarizer positioned after the sample.

The pump direction is almost collinear with the probe one. Assuming that all

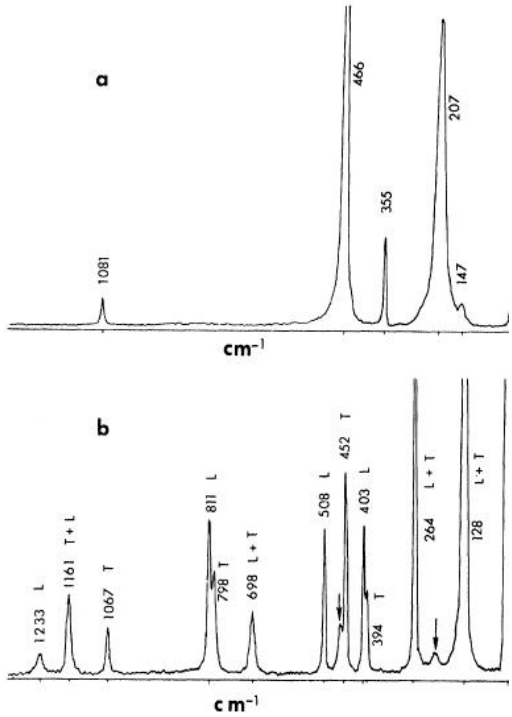

Figure 4.2: Room-temperature Raman spectra of α-quartz from[17]. Polarization assignments (L =longitudinal, T =transverse). (a) A_1 modes. (b) E modes. The arrows indicate intense A_1 modes being transmitted due to imperfect alignment.

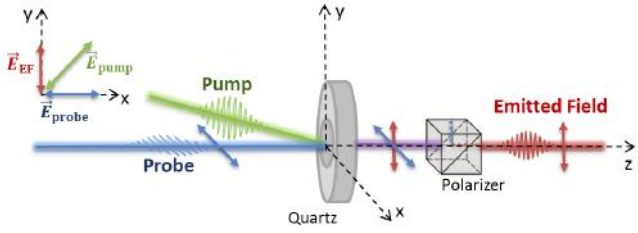

Figure 4.3: Experimental geometry for impulsive stimulated Raman scattering on α-quartz. The sample is depicted at the origin of the coordinates. The polarization configuration of pump, probe and emitted field is indicated on top-left. After the interaction with the sample the probe undergoes a polarization selection in order to detect the emitted field only.

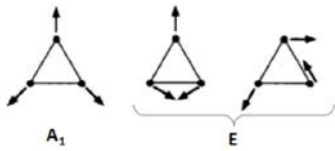

Figure 4.4: Normal mode vibrations for a system with C_3 symmetry. A symmetric A_1 breathing vibrational mode and a doubly-degenerate E-symmetry vibrational mode[19].

the involved optical fields propagate along the z direction, we can limit our analysis to the xy plane. In this case the quartz Raman tensors assume the form[20]

$$A = \begin{pmatrix} a & 0 \\ 0 & a \end{pmatrix} \quad E^T = \begin{pmatrix} c & 0 \\ 0 & -c \end{pmatrix} \quad E^L = \begin{pmatrix} 0 & -c \\ -c & 0 \end{pmatrix}. \tag{4.2}$$

Following the notation in[21], the susceptibility tensor can be expressed as:

$$\chi^{(3)}_{ijkl} = A_{ij}\, A_{kl} + E^T_{ij}\, E^T_{kl} + E^L_{ij}\, E^L_{kl}, \tag{4.3}$$

where each index can assume the values $1, 2$ associated to the direction x and y respectively. Thus, the susceptibility tensor $\chi^{(3)}_{ijkl}$ gives rise to a 4×4 block-matrix

$$\begin{pmatrix} \begin{pmatrix} a^2+c^2 & 0 \\ 0 & a^2-c^2 \end{pmatrix} & \begin{pmatrix} 0 & c^2 \\ c^2 & 0 \end{pmatrix} \\ \begin{pmatrix} 0 & c^2 \\ c^2 & 0 \end{pmatrix} & \begin{pmatrix} a^2-c^2 & 0 \\ 0 & a^2+c^2 \end{pmatrix} \end{pmatrix}. \tag{4.4}$$

The first two indexes refer to the outer matrix elements and describe the polarization components of the emitted field (i index) and of the probe field (j index), while the last two indexes (k and l) indicate the inner matrix elements and describe the polarization components of the two pump fields.

In particular, we are interested in selecting the excitation of an E symmetry Raman mode. For this purpose we use a probe linearly polarized along x and we perform a polarization selection after the sample in order to detect the emitted field component orthogonal to the probe (along y). This polarization configuration allows the selection of the susceptibility matrix elements $\chi^{(3)}_{21kl}$ associated with the involved E phononic mode. Notice that such elements vanish when $k = l$ that is when the two pump fields are both polarized along x or along y. Thus, in order to activate the process, we need the two pump fields (two frequency components of the same laser pulse) to have orthogonal polarizations. This is possible when the pump pulse is linearly polarized along a direction in between x and y. In particular, the efficiency of the ISRS is maximal when the pump polarization is at $45\,^\circ$ with respect to the x axis. This is indeed the configuration we chose and consequently the

matrix elements involved in our experiment are $\chi^{(3)}_{21kl(k\neq l)} = c^2$, getting an emitted field almost collinear with the unscattered probe photons and with polarization orthogonal to the probe one. We configure a polarizer after the sample in order to transmit the emitted field polarization only. The global polarization configuration is sketched in Fig 4.3.

Ideally, only the emitted field is selected after the polarizer. This is called *homodyne configuration* and the detected signal will be in the form,

$$I_{signal} \propto |E_{\mathrm{EF}}|^2. \tag{4.5}$$

Note that a full extinction of the unscattered probe is experimentally not achievable (polarizer extinction rate 10^5). The residual probe acts as a local oscillator amplifying the emitted field within the total signal[22]. The configuration in which the emitted field is amplified by an other optical field, called local oscillator, is dubbed *heterodyne configuration*. In this case the total intensity detected by the photodiode is,

$$I_{signal} \propto |E_{\mathrm{EF}} + E_{\mathrm{LO}}|^2 \propto |E_{\mathrm{EF}}|^2 + |E_{\mathrm{LO}}|^2 + E_{\mathrm{LO}}E^*_{\mathrm{EF}} + E^*_{\mathrm{LO}}E_{\mathrm{LO}} \ . \tag{4.6}$$

4.2.1 Preliminary standard pump-probe experiments

The preliminary experimental results adopting standard pump-probe optical spectroscopy are now presented. Such preliminary data have been recorded at the LOA laboratory in Paleseau. The pump and probe beams are generated by pulsed laser source with $1\,kHz$ repetition rate, $800\,nm$ central wavelength and almost 150 fs pulse duration. The spot radius respectively used for pump and probe is $60\,\mu m$ and $30\,\mu m$. Both the pump and the probe are focused on the sample by a lens and after the interaction a second lens collimates the transmitted beam. The pulse passes through a polarizer in order to select the emitted field and finally reaches the photodiode. The output of the photodiode is sent to a lock-in amplifier, which amplify a specific frequency component of the signal integrated over different subsequent pulses. In standard optical pump-probe experiments the signal is indeed modulated by using a mechanical chopper generally in the pump path. The frequency at which the chopper modulates the pump is sent in input to the lock in amplifiers in order to amplify the appropriate signal. The result of the experiment is the intensity of the transmitted probe as a function of the delay between the pump and probe. It is important to note that in this configuration the response is integrated over a large number of pulses determined by the lock-in acquisition time. This configuration allows for a very precise measurement of the mean photon number transmitted by the sample as a function of the pump-probe delay, but doesn't allow for the measurements of intrinsic noise due to pulse to pulse intensity fluctuation. A scheme of the setup is shown in Fig 4.5.

A set of measurements for different pump fluences is shown in Fig 4.6.
The results have been obtained with the polarizer, shown in Fig 4.3, set in order to minimize the transmission of the probe in absence of the pump. This should ideally correspond to the homodyne configuration. The probe energy per pulse is fixed at

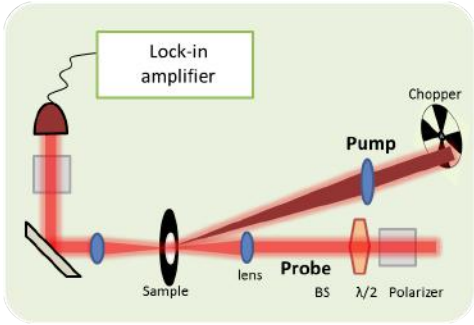

Figure 4.5: Standard pump-probe optical experiments setup. The lock-in acquisition configuration in sketched.

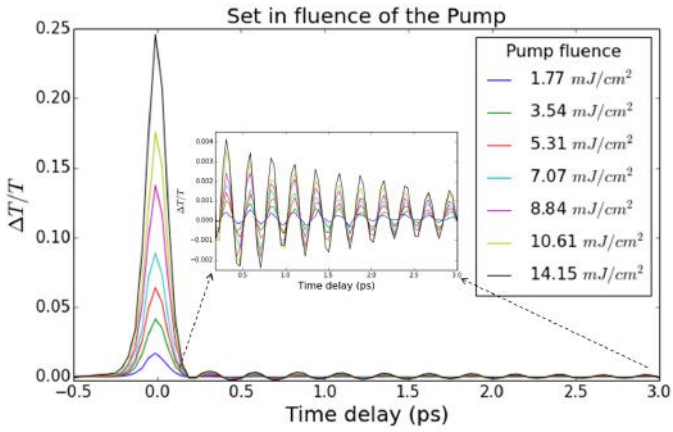

Figure 4.6: Standard pump-probe experimental results. Measurement on α-quartz for different values of the pump fluence.

50 nJ which corresponds to $\sim 1\text{mJ/cm}^2$ fluence (probe spot radius $\sim 30\,\mu$m). The oscillating response has been fit with a dumped-sin function $A\sin(\omega t+\phi)\,e^{-t/\tau}$. The best fit amplitude A parameter is plotted in Fig 4.7 as a function of the pump fluence.

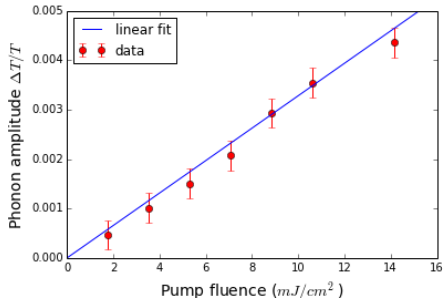

Figure 4.7: Oscillation amplitude vs pump fluence. Amplitude of the oscillating signal $\Delta T/T$ as a function of the pump fluence.

As it is expected from the theory, the results show the linear dependence of the amplitude of the emitted field vs the intensity of the pump. The Fourier transform of the oscillating part of the data is shown in Fig. 4.8. It confirms the excitation of the E-symmetry mode with frequency $\nu_E = 128\,cm^{-1} = 3.84\,THz$.

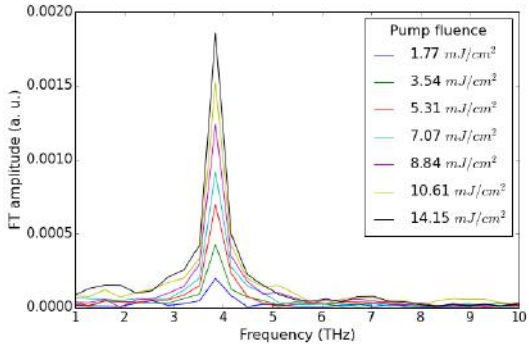

Figure 4.8: Fourier transform of the standard pump-probe signal. FT of the oscillating part of the measurements showed in Fig. 4.6

Concluding, the presented data have been obtained using standard pump-probe optical experiments and served as characterization measurements to design the experimental layout which allows to excite E-symmetry Raman optical modes in α-quartz at room temperature and get an emitted field with polarization orthogonal to the probe one.

In this as in all standard apparatuses we have access only to the mean number of photons of the emitted field, in the following we present a novel experimen-

tal approach which allows us to measure the complete photon number statistical distribution.

4.3 Shot-noise limited pump-probe experiments

We propose here a new approach to time domain studies. The experimental layout is similar to standard pump and probe experiments. The sample is excited by an ultrashort pump pulse and the time evolution of the response is measured by means of a second much weaker probe pulse, that interacts with the photo-excited material at a delay time τ. Both pump and probe come from the same laser source, a 250 kHz mode-locked amplified Ti:Sapphire system. The pulse duration is 80 fs, the fractional change in the probe transmission due to the pump is of the order of 5% for a pump fluence of 25 mJ cm^{-2}.

The unique characteristics of our setup are:

- i) unlike standard experiments, where the response is integrated over many repeated measurements, our system can measure individual pulses;
- ii) the apparatus operates in low noise conditions allowing for the measurement of intrinsic photon number quantum fluctuations.

In detail, we adopt a differential acquisition scheme where each probe pulse is referenced with a second pulse which has not interacted with the sample. A sketch of this configuration is shown in Fig 4.9.

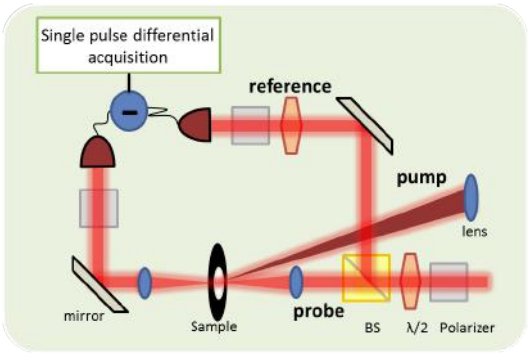

Figure 4.9: Scheme of the experimental setup. Each single pulse transmitted from the sample is detected using a single pulse differential acquisition system and referenced with a second pulse which has not interacted with the sample.

For each measurement the differential voltage is digitized and integrated, giving the transmittance ΔT_i for the i^{th} measurement (i^{th} transmitted pulse).

The acquisition system is made of a balanced amplified differential photodetector and a fast digitizer (*Spectrum* M3i.2132-exp) with sampling rate 1 GS s^{-1}. The differential photodetector, described in details in Appendix A, consists of two *Hamamatsu S3883* Silicon PIN photodiodes with 0.94 quantum efficiency connected

in reverse bias and followed by a low-noise charge amplifier. The photo-currents generated by the two photodiodes in response to a single optical pulse impinging on them (transmitted probe pulse on the first photodiode and reference pulse on the second photodiode) are physically subtracted and the resulting charge is amplified using *CAEN* custom designed electronic components. Note that we use here the convention of expressing the voltage acquired for every single differential pulse acquisition, ΔT_i , as the sum of the voltages digitized for 500 points at 1 GS s^{-1}. For reference, the digitized measurement of a pulse with a 1 V voltage peak corresponds to a value of 300 V. The shot-noise characterization of the detector is reported in Appendix A. We chose a probe power within the shot-noise linearity interval (2.5 mW, 0.2 mJ cm^{-2} on the sample; note that this corresponds roughly to 10^6 photons per pulse scattered in cross polarization on the detector). This provides a reference for the shot noise value of about 1 V^2 which is used to benchmark the noise in time domain experiments and avoid additional noise sources.
The detector shot-noise linearity test (Fig A.5) demonstrates that we are sensible to quantum fluctuations of the photon number. In particular, the shot-to-electronic noise at the maximum probe intensity in the linear regime is approximately 10 dB.

Going back to the actual experiment, for every pump and probe delay τ, we repeat this single pulse measurements for $N = 4000$ consecutive pulses. Fig. 5.1 (a) gives a useful visual representation of the obtained data. For one pump and probe scan l the normalized histogram of $N = 4000$ acquired pulses for each delay time is shown. Each histogram represents the distribution of the measured ΔT_i for a specific delay time τ. For a clearer visualization of the physically meaningful information in the time evolution of the statistical distribution, Fig. 5.1 (b) reports the histogram centered at zero.
The pump and probe scan is repeated several times and each l^{th} scan provides $\Delta T^{(l)}_{\text{mean}} = \frac{1}{N}\sum_i \Delta T_i$, and $\Delta T^{(l)}_{\text{var}} = \frac{1}{N}\sum_i [\Delta T_i - \Delta T^{(l)}_{\text{mean}}]^2$. Finally the averages of these two quantities are calculated over all M scans as $\Delta T_{\text{mean}} = \frac{1}{M}\sum_{l=1}^{M} \Delta T^{(l)}_{\text{mean}}$ and $\Delta T_{\text{var}} = \frac{1}{M}\sum_{l=1}^{M} \Delta T^{(l)}_{\text{var}}$.

The time domain response, averaged over $M = 10$ scans, is shown in Fig. 5.2 (a) for a representative pump fluence of 14 mJ cm^{-2} (a pump fluence dependent study is reported later). The blue curve depicts the time evolution of the mean value of the transmittance ΔT_{mean}, whereas the red curve shows the time evolution of its variance ΔT_{var}. The Fourier transform of the mean (Fig. 5.2 (c), blue curve) has a single peak which is ascribed to the E-symmetry quartz vibrational mode with frequency $\Omega = 128\,\text{cm}^{-1} = 3.84\,\text{THz}$[17]. The same frequency component is observed in the Fourier transform of the variance (Fig. 5.2 (c), red curve). In addition, a second peak at twice the phonon frequency appears exclusively in the variance. A wavelet analysis of the variance oscillations allows for a time domain study of the two frequency components (Fig. 5.2 (b)): one notices that, while the fundamental frequency survives for roughly 7 ps, the 2Ω component vanishes within the first 2 ps. The different lifetimes between the Ω and 2Ω components of the variance are seen also by a close inspection of the raw data distribution plotted in Fig. 5.2 (b).

Note that the 2Ω in our data is visible only in experimental conditions where

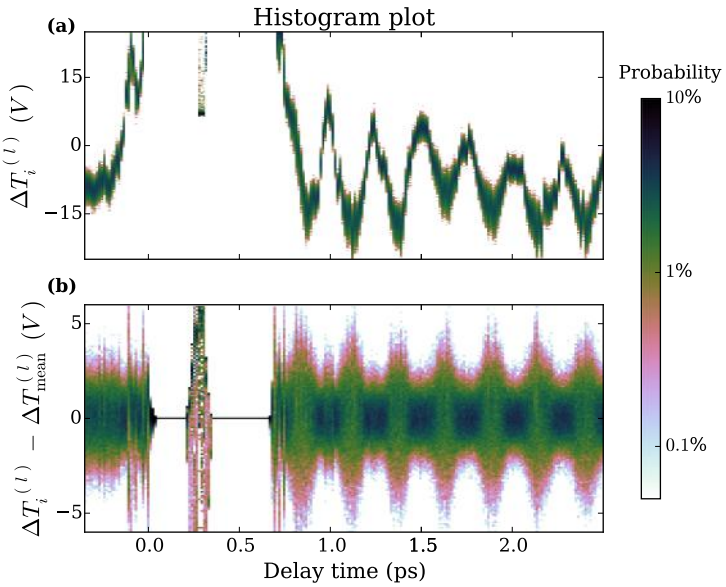

Figure 4.10: Time domain transmittance histogram plot. ΔT_i distribution as a function of pump-probe delay for a representative scan l. (a) For each time delay a color plot of the normalized histogram of $N = 4000$ acquired pulses is shown. (b) Histogram plot of ΔT_i centered at zero. The data shown are obtained with the largest pump fluence used in the experiments ($25\,\mathrm{mJ\,cm^{-2}}$).

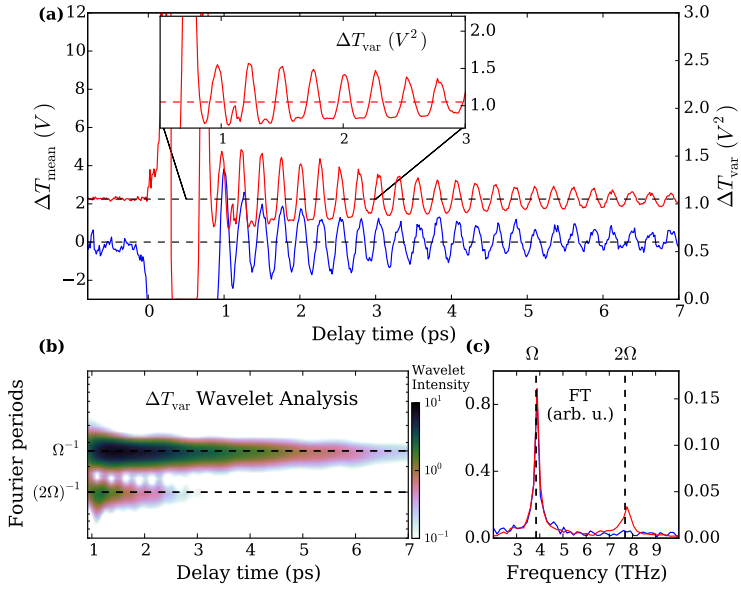

Figure 4.11: Time domain transmittance mean and variance. (a) ΔT_{mean} (blue curve) and ΔT_{var} (red curve) as a function of the pump-probe time delay. The zero time is the instant in which pump and probe arrive simultaneously on the sample. In the inset a zoom of the variance for the first 3 ps is shown. (b) Wavelet analysis (Morlet power spectrum) of the variance oscillating part. (c) Fourier transforms of the oscillating parts of mean (blue curve) and variance (red curve). In (a) and (c) the left axis is related to the mean while the right axis is related to the variance.

the noise is dominated by the quantum uncertainty, a situation which is known as shot-noise regime. In such conditions ΔT_{var} measures the quantum variance of the scattered probe photon number. In order to assure the absence of classical noise contribution, a full characterization of the classical noise sources has been done. The latter is reported in the Appendix.

It should further be stressed that in experimental conditions where the noise is larger and dominated by classical sources the 2Ω contribution to the noise becomes unmeasurable.

The presence of the 2Ω frequency component is suggestive of phonon squeezing, as it has been indicated by Raman tensor models[13,23,24], presented in Section 2.6.2. Nevertheless, the experimental evidences up to date lack a direct comparison with a reliable quantum noise reference[12,25–27]. Hence, in these experiments the observation of the 2Ω frequency in the optical noise is considered as an indication of phonon squeezing, but not an unequivocal proof. In details, a 2Ω oscillating optical noise was reported in[12], but later ascribed to an artifact[28] due to the experimental amplification process. In particular, it has been demonstrated that amplification artifacts become more relevant when, using a lock-in amplifier based acquisition, the time constant of the lock-in increases with respect to the time between steps in the pump-probe delay. This gives rise to maxima in the noise where the derivative of the mean signal is maximal[28]. Here we use a pump power density which is almost 3 orders of magnitude higher than in[12,28]. In addition, we observe a 2Ω frequency component in the optical variance which exhibits maxima in correspondence with the minima of the derivative of the mean signal, hence ruling out possible artifacts of the kind described in[28].

4.4 Comparison with the model

In order to predict how the fluctuations of the atomic positions in a lattice can be mapped onto the photon number quantum fluctuations of the probe field, we develop a novel theoretical approach to time domain studies which treats quantum mechanically both the material and the optical fields involved in the non-linear processes. Several semiclassical models describe the possibility of generating "classical" (coherent states) and non classical vibrational states by photo-excitation. In particular, for transparent materials like quartz, the most commonly used approach is to adopt Raman tensor models where the interaction between photons and phonons is not mediated by dipole allowed electronic transitions. In this condition, interactions linear in the phonon operators allow for the generation of coherent vibrational states, while high order interactions are required for the generation of non classical squeezed states[11,23,24]. In materials with allowed dipole transitions, as in presence of excitons, different models based on electron-phonon coupling Hamiltonians have been proposed. In those models it has been shown that squeezed phonon states can result only by successive excitations with a pair of pulses[14,29]. All these models mainly adopt semiclassical approaches where the optical fields are described classically[22], and therefore are unable to reproduce the quantum proprieties of the probe optical field that can be measured with the shot-noise limited

pump and probe setup presented here. The key aspect of our approach, allowing us to bridge this gap, is to study both generation and detection of phonon states using a fully quantum formalism through an effective photon-phonon interaction, which is descriptive of experiments in transparent systems, such as α-quartz. The basic tool is a quantum Hamiltonian able to describe both pump and probe processes. Being linear and bilinear in the photon and phonon operators, this Hamiltonian accounts for the possible generation of coherent and squeezed phonon states through the pump process. In particular, it models also the detection of the photo-excited phonon states, describing the probing process by a fully quantum approach, providing in this way a direct comparison with the experimentally measured photon number quantum fluctuations of the scattered probe pulses[30].

This fully quantum approach has been reported in detail in Section 2.7. Here we will report only the main ingredients of the model in order to obtain guide the reader in the comparison with the experimental results.

The first step is to adopt a quantized description for the mode-locked pulsed laser fields (Section 2.4). Each mode of frequency $\omega_j = \omega_0 + j\delta$, where ω_0 is the pulse central frequency, δ is a constant depending on the laser repetition rate and j is an integer, is quantized and described by single mode creation and annihilation operators $\hat{a}_j^\dagger$ and $\hat{a}_j$. In this framework ISRS can be modelled by means of an effective impulsive interaction Hamiltonian which is descriptive of both the pumping and the probing processes. In both processes two optical fields with orthogonal polarizations (denoted with subscript x or y) are involved: two pump fields in the pumping process and the probe and the emitted field in the probing process. The interaction Hamiltonian has the form

$$\begin{aligned}\mathcal{H} = \sum_{j,j'=-J}^{J} \Big[& \; g^1_{j,j'}\,\mu_{\mathrm{d}}\big(\hat{a}^\dagger_{xj}\,\hat{a}_{yj'}\,\hat{b}^\dagger + \hat{a}_{xj}\,\hat{a}^\dagger_{yj'}\,\hat{b}\big) \\ & + \; g^2_{j,j'}\,\mu_{\mathrm{s}}\big(\hat{a}^\dagger_{xj}\,\hat{a}_{yj'}\,(\hat{b}^\dagger)^2 + \hat{a}_{xj}\,\hat{a}^\dagger_{yj'}\,\hat{b}^2\big)\Big]\,, \end{aligned} \tag{4.7}$$

where $2J+1$ is the total number of modes within a mode-locked optical pulse, $\hat{b}$ and $\hat{b}^\dagger$ are the phonon annihilation and creation operators, μ_{d} and μ_{s} are coupling constants and the functions $g^\ell_{j,j'}$ take into account the relations between the frequencies of the involved fields,

$$g^\ell_{j,j'} = \begin{cases} 1 & \text{if } j' = j + \frac{\ell\Omega}{\delta} \\ 0 & \text{elsewhere,} \end{cases} \qquad \ell = 1, 2\,,$$

with Ω the phonon frequency. A complete interaction Hamiltonian should contain also second order processes involving phonons with opposite momenta. However, since the probe detects only the $\mathbf{k} \simeq 0$ optical transition, we can make use of an effective Hamiltonian that accounts only for this kind of process.

The whole theoretical description of the experiment can be rationalized in a four step process as sketched in Fig. 4.12: (i) generation of phonon states in the pumping process, (ii) evolution of the produced vibrational state, (iii) probing process and (iv) read out of the emitted photon observables.

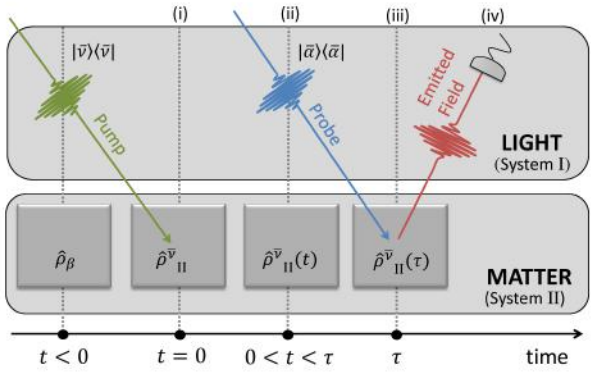

Figure 4.12: Sketch of the four steps effective theoretical model. The steps are indicated with roman numbers. The details of the theory for each step are reported in the text. The photon and phonon system are denoted with I and II, respectively.

- (i) Initially, the sample is in thermal equilibrium and it is described by a thermal phonon state $\hat{\rho}_\beta$, at inverse temperature β. The laser pump pulse is described by a multimode coherent state of high intensity $|\bar{\nu}\rangle = |\nu_{-J}\rangle \otimes \cdots \otimes |\nu_J\rangle$, where $|\nu_j\rangle$ are single mode coherent states associated with all the frequency components within the pulse. Each $|\nu_j\rangle$ is an eigenstate of the annihilation operator $\hat{a}_j$ of photons in the mode of frequency ω_j, $\hat{a}_j\,|\nu_j\rangle = \nu_j\,|\nu_j\rangle$. We indicate with $\bar{\nu}$ the vector whose components are the amplitudes ν_j. The equilibrium (pre-pump) photon-phonon state $\hat{\rho} = |\bar{\nu}\rangle\langle\bar{\nu}| \otimes \hat{\rho}_\beta$ is instantaneously transformed into $\hat{\rho}^{\bar{\nu}} = \mathcal{U}\,\hat{\rho}\,\mathcal{U}^\dagger$ by means of the unitary operator $\mathcal{U} = \exp\{-i\mathcal{H}\}$. Since the pumping operator $\mathcal{U}$ acts on a high intensity photon coherent state $\bar{\nu}$, we can use the mean field approximation for the photon degrees of freedom and replace $\hat{a}$ with ν and $\hat{a}^\dagger$ with ν^* for both pump modes involved in equation (4.7), thus replacing $\mathcal{U}$ by

$$\mathcal{U}_{\bar{\nu}} = \exp\Big\{-i \sum_{j,j'=-J}^{J} \Big[\; g^1_{j,j'}\,\mu_{\rm d}\big(\nu^*_{xj}\,\nu_{yj'}\,\hat{b}^\dagger + \nu_{xj}\,\nu^*_{yj'}\,\hat{b}\big) + \; g^2_{j,j'}\,\mu_{\rm s}\big(\nu^*_{xj}\,\nu_{yj'}\,(\hat{b}^\dagger)^2 + \nu_{xj}\,\nu^*_{yj'}\,\hat{b}^2\big)\Big]\Big\}. \quad (4.8)$$

The evolution operator generates coherent and squeezed phonon states, respectively, through the linear and quadratic terms in the phonon operators $\hat{b}$ and $\hat{b}^\dagger$. The initial state $\hat{\rho}^{\bar{\nu}}$ contains information about both photons and phonons. Tracing over the photon degrees of freedom, the resulting state $\hat{\rho}^{\bar{\nu}}_{\rm II}$ describes the excited phonons brought out of equilibrium by the impulsive

pump process.

- (ii) The time evolution of the excited phonons is described by using an open quantum systems approach, namely by means of a suitable master equation of Lindblad form[31,32] that takes into account, besides the quantum unitary evolution, also the dissipative and noisy effects due to the interaction with a thermal environment.

- (iii) The incoming probe pulses are in the multimode coherent state $|\bar{\alpha}\rangle$. The probing process at time τ is described by the same impulsive unitary operator $\mathcal{U}$ used for the pump. However, in this case we can apply the mean field approximation only to the probe photon operators with x polarization, which correspond to a much more intense field than those with y polarization. Moreover, since the probe field is much weaker than the pump field, the quadratic terms in the interaction Hamiltonian in equation (4.7) can now be neglected. The resulting unitary operator is

$$\mathcal{U}_{\bar{\alpha}'} = \exp\{-i\|\bar{\alpha}'\|\big(\hat{A}(\bar{\alpha}')\,\hat{b}^\dagger + \hat{A}^\dagger(\bar{\alpha}')\,\hat{b}\big)\}\ , \tag{4.9}$$

  where $\hat{A}(\bar{\alpha}')$ is the collective photon annihilation operator,

$$\hat{A}(\bar{\alpha}') = \frac{1}{\|\bar{\alpha}'\|}\sum_{j=-J}^{J}(\alpha'_j)^*\,\hat{a}_{yj}\ ,$$

  such that $\Big[\hat{A}(\bar{\alpha}'), \hat{A}^\dagger(\bar{\alpha}')\Big] = 1$, and $\bar{\alpha}'$ is the vector with components

$$\alpha'_j = \mu_{\rm d}\sum_{j'=-J}^{J} g^1_{j',j}\,\alpha_{xj'}\ .$$

  The unitary operator in equation (4.9) acts on a state of the form $|\bar{\alpha}\rangle\langle\bar{\alpha}| \otimes \hat{\rho}^{\bar{\nu}}_{\rm II}(\tau)$. The information about the phonons are extracted by measuring the emitted field photons. In particular, the emitted photon state $\hat{\rho}_{\rm I}(\tau)$ is obtained by tracing away the phonon degrees of freedom.

- (iv) The possible quantum features of the phonon state, e.g. squeezing, can be read off as they are imprinted into $\hat{\rho}_{\rm I}(\tau)$. In particular for each time delay τ we can compute the quantities

$$\langle\hat{N}_y\rangle_\tau = \langle\hat{A}^\dagger(\bar{\alpha}')\hat{A}(\bar{\alpha}')\rangle_\tau$$

  and

$$\Delta^2_\tau\hat{N}_y = \langle\hat{N}^2_y\rangle_\tau - \langle\hat{N}_y\rangle^2_\tau\ ,$$

  which correspond to the observables measured in the experiment, that are the mean value and the variance of the number of photons of the emitted field.

In particular, one uses that

$$\begin{aligned} U^{\dagger}_{\bar{\alpha}'}\,\hat{N}_y\,U_{\bar{\alpha}'} &= A^{\dagger}(\bar{\alpha}')\hat{A}(\bar{\alpha}')\cos^2(\|\bar{\alpha}'\|) + \hat{b}^{\dagger}\hat{b}\sin^2(\|\bar{\alpha}'\|) + \\ &+ \frac{i}{2}\sin(2\|\bar{\alpha}'\|)\big(A(\bar{\alpha}')\hat{b}^{\dagger} + A^{\dagger}(\bar{\alpha}')\hat{b}\big), \end{aligned} \tag{4.10}$$

where, given the experimental conditions effectively described by the model, it is plausible to set all amplitudes $\alpha_{xj} = \alpha_x$ and $\alpha_{yj} = \alpha_y = |\alpha_y|\exp(i\theta_y)$, in which case

$$\alpha'_j = \mu_{\rm d}\alpha_x = |\mu_{\rm d}\alpha_x|e^{i\theta'}, \qquad \text{and} \qquad \|\bar{\alpha}'\| = \sqrt{K}|\mu_{\rm d}\alpha_x|\,, \tag{4.11}$$

where $K = 2J+1$ is the total number of modes within a mode-locked optical pulse.
By denoting with $I_y = K|\alpha_y|^2$ the pulse intensity for the y polarization and using that

$$\hat{A}(\bar{\alpha}')\,|\bar{\alpha}_y\rangle = \sqrt{I_y}e^{-i(\theta'-\theta_y)}\,|\bar{\alpha}_y\rangle\,, \tag{4.12}$$

one explicitly computes:

$$\begin{aligned} \langle\hat{N}_y\rangle_{\tau} &= I_y\cos^2(\|\bar{\alpha}'\|) + \sin^2(\|\bar{\alpha}'\|)\,\langle\hat{b}^{\dagger}\hat{b}\rangle_{\tau} \\ &+ \frac{i}{2}\sqrt{I_y}\,\sin(2\|\bar{\alpha}'\|)\left(e^{-i(\theta'-\theta_y)}\,\langle\hat{b}^{\dagger}\rangle_{\tau} - e^{i(\theta'-\theta_y)}\,\langle\hat{b}\rangle_{\tau}\right), \end{aligned} \tag{4.13}$$

where $\langle\hat{O}\rangle_{\tau} = {\rm Tr}_{\rm II}\left(\hat{\rho}^{\bar{\nu}}_{\rm II}(\tau)\,\hat{O}\right)$ is the expectation value of any phonon operator $\hat{O}$ with respect to the phonon state $\hat{\rho}^{\bar{\nu}}_{\rm II}(\tau)$.

Despite its complicated expression, we report also the number variance $\Delta^2_{\tau}\hat{N}_y$ predicted by the model, as $\langle\hat{N}_y\rangle_{\tau}$ and $\Delta^2_{\tau}\hat{N}_y$ are the quantities compared with the experimental data:

$$\begin{aligned} \Delta^2_{\tau}\hat{N}_y &= I_y\cos^4(\|\bar{\alpha}'\|) + \sin^4(\|\bar{\alpha}'\|)\left(\langle(\hat{b}^{\dagger}\hat{b})^2\rangle_{\tau} - \langle\hat{b}^{\dagger}\hat{b}\rangle^2_{\tau}\right) \\ &+ \sin^2(\|\bar{\alpha}'\|)\cos^2(\|\bar{\alpha}'\|)\;\langle\hat{b}^{\dagger}\hat{b}\rangle_{\tau} \\ &- I_y\sin^2(\|\bar{\alpha}'\|)\cos^2(\|\bar{\alpha}'\|)\;\Big[e^{-2i(\theta'-\theta_y)}\left(\langle(\hat{b}^{\dagger})^2\rangle_{\tau} - \langle\hat{b}^{\dagger}\rangle^2_{\tau}\right) \\ &+ e^{2i(\theta'-\theta_y)}\left(\langle\hat{b}^2\rangle_{\tau} - \langle\hat{b}\rangle^2_{\tau}\right)\Big] \\ &+ I_y\sin^2(\|\bar{\alpha}'\|)\cos^2(\|\bar{\alpha}'\|)\;\left(2\,\langle\hat{b}^{\dagger}\hat{b}\rangle_{\tau} + 1 - 2\,\langle\hat{b}^{\dagger}\rangle_{\tau}\,\langle\hat{b}\rangle_{\tau}\right) \\ &+ i\sqrt{I_y}\,\sin(\|\bar{\alpha}'\|)\cos^3(\|\bar{\alpha}'\|)\;\left(e^{-i(\theta'-\theta_y)}\,\langle\hat{b}^{\dagger}\rangle_{\tau} - e^{i(\theta'-\theta_y)}\,\langle\hat{b}\rangle_{\tau}\right) \\ &+ i\sqrt{I_y}\,\sin^3(\|\bar{\alpha}'\|)\cos(\|\bar{\alpha}'\|)\;\Big[2e^{-i(\theta'-\theta_y)}\left(\langle(\hat{b}^{\dagger})^2\hat{b}\rangle_{\tau} - \langle\hat{b}^{\dagger}\hat{b}\rangle_{\tau}\,\langle\hat{b}^{\dagger}\rangle_{\tau}\right. \\ &+ \left.\frac{1}{2}\,\langle\hat{b}^{\dagger}\rangle_{\tau}\right) - 2e^{i(\theta'-\theta_y)}\left(\langle\hat{b}^{\dagger}\hat{b}^2\rangle_{\tau} - \langle\hat{b}^{\dagger}\hat{b}\rangle_{\tau}\,\langle\hat{b}\rangle_{\tau} + \frac{1}{2}\,\langle\hat{b}\rangle_{\tau}\right)\Big]. \end{aligned} \tag{4.14}$$

The theoretical results for $\mu_s = 0$ and $\mu_s \neq 0$ are shown in Fig. 4.13 together with the corresponding wavelet analysis for the variance of the number of emitted photons. The calculations reproduce the experimental results in Fig. 5.2, revealing

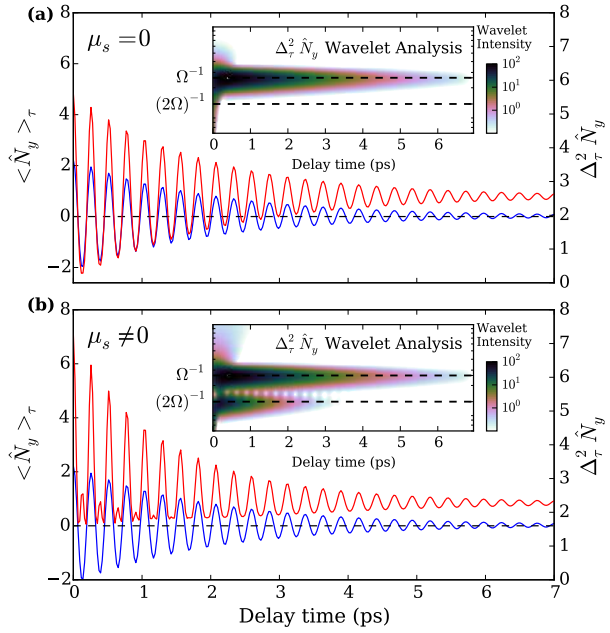

Figure 4.13: Model predictions. Theoretical calculations of the mean value and the variance of the number of photons of the emitted field. The left axis is related to the mean while the right axis is related to the variance. Comparison between the case with squeezing coupling constant $\mu_s = 0$ (a) and $\mu_s \neq 0$ (b). A wavelet analysis (Morlet power spectrum) of the variance is reported in the inset for both cases.

a 2Ω frequency component in the variance, only when the pump creates squeezed phonon states ($\mu_s \neq 0$). In particular, for $\mu_s \neq 0$, the model reproduces the different lifetimes between the Ω and 2Ω components in the variance observed in the experiments.

The proposed effective interaction model is further validated by a pump fluence dependence study. Fig. 4.14 shows the amplitude of the 2Ω peak in the Fourier transform of the variance, ΔT_{var}, as a function of the pump fluence. The functional behaviour obtained from the model predictions (continuous line in Fig. 4.14) agrees with the experimental data only in presence of a pump-induced squeezing of the phonon mode ($\mu_s \neq 0$).

One can observe that in equation (4.14) the phononic correlation functions involving $\hat{b}$ and $\hat{b}^\dagger$ contribute with oscillations at frequency Ω while those involving $\hat{b}^2$ and $\hat{b}^{\dagger 2}$ give rise to 2Ω oscillations. Collecting the corresponding coefficients one

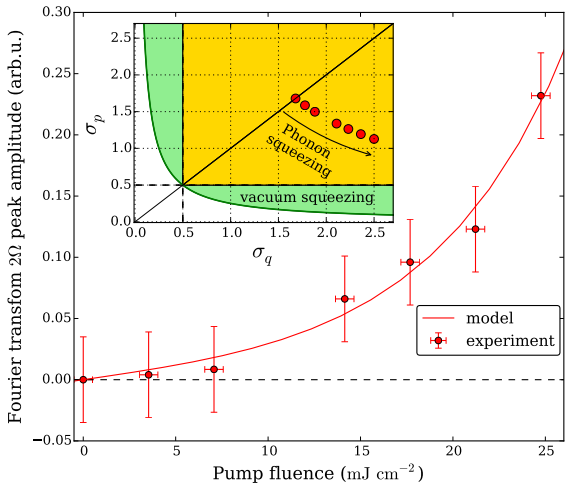

Figure 4.14: Fourier transform 2Ω peak amplitude of the variance. Amplitude of the 2Ω peak of the Fourier transform of the time dependent variance ΔT_{var}. The error bars indicate the standard deviation over 10 scans. Comparison between experiments and theory as a function of the pump fluence. In the inset the uncertainties for the phonon position and momentum operators, calculated from the model, are plotted for the corresponding pump fluences.

finds the following amplitude for the 2Ω oscillating components:

$$|A_{2\Omega}(\tau)| = \frac{I_y(1+2n')}{8} e^{-\lambda\tau} \sin^2(2\|\bar{\alpha}'\|) \sinh(2r) \ , \tag{4.15}$$

where the amplitude of the squeezing parameter $r = 2|c_2| = 2K|\mu_s||\nu|^2$ is obtained from (2.80) and (2.76) by putting all pump amplitudes equal to ν. Moreover we take λ to comply with the observed oscillation time-scale and the time $\tau > 0$ such that $\lambda\tau \ll 1$. In particular, in Fig. 4.14 we show a fit of the experimental results for different pump intensities with the functional behaviour of $A_{2\Omega}$ predicted by the model in equation (4.15). We find an optimal value of the coupling parameter μ_s for which the model agrees with the experiments. We used such a value for computing the amplitude r of the squeezing parameter (defined in equation (2.76)) for all the experimental pump fluences. In particular $|\nu|^2$ is the number of photons per unit cell per pulse. We then computed the uncertainties in the position and momentum phonon operators as in equation (2.82). The results reported in the inset of Fig. 4.14 unveil photo-excited thermal squeezed vibrational states. For high pump fluences the uncertainty on one of the phonon quadratures falls indeed below the thermal limit at the equilibrium, indicating the squeezed nature of the photo-excited thermal vibrational states.

The experimental amplitude of the Ω peak in the Fourier Transform of the mean, ΔT_{mean}, and of the variance, ΔT_{var}, as a function of the pump fluence are shown in Fig 4.15.

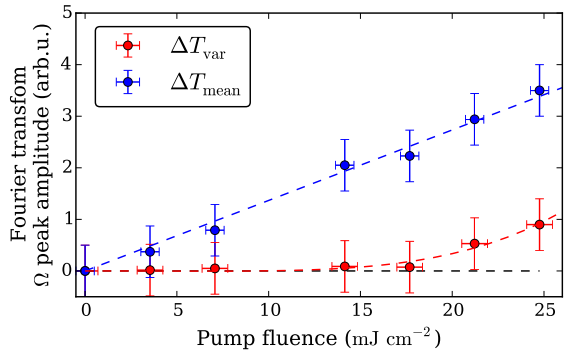

Figure 4.15: Amplitude of the Ω peak of the Fourier transform. Fourier transform Ω peak of the time dependent mean, ΔT_{mean}, (blue points) and of the time dependent variance, ΔT_{var}, (red points). The dashed lines are a guide for the eyes. The error bars indicate the standard deviation over 10 scans.

For completeness we also report the explicit time evolution of $\Delta^2_\tau \hat{N}_y$ in terms of both the amplitude $A_{2\Omega}$ of the 2Ω frequency component and the amplitude A_Ω of the fundamental frequency component:

$$\Delta^2_\tau \hat{N}_y = A_0(\tau) + A_\Omega(\tau)e^{i\Omega\tau} + A^*_\Omega(\tau)e^{-i\Omega\tau} + A_{2\Omega}(\tau)e^{2i\Omega\tau} + A^*_{2\Omega}(\tau)e^{-2i\Omega\tau}, \quad (4.16)$$

where the explicit expression for $|A_\Omega(\tau)|$ is:

$$\begin{aligned} |A_\Omega(\tau)| \;=\; & \frac{1}{2}\sqrt{I_y}\,|z|\,e^{-\lambda\tau/2} \\ & \times \Big|2e^{-\lambda\tau}\sin(2\|\bar{\alpha}'\|)\sin^2(\|\bar{\alpha}'\|)\left[(1+n'+n-(1+2n')\cosh(2r))\,e^{i\theta_r}\cosh(r)\right. \\ & + \left.(n'-n+(1+2n')\cosh(2r))\,e^{2i\theta_z}\sinh(r)\right] \\ & - \sin(2\|\bar{\alpha}'\|)\left(1+2n\sin^2(\|\bar{\alpha}'\|)\right)\left(e^{i\theta_r}\cosh(r)-e^{2i\theta_z}\sinh(r)\right)\Big|\ , \end{aligned} \quad (4.17)$$

where $|z|$ is the corresponding photo-exited displacement in the phonon and θ_z its phase.

We stress that, if the pump pulse does not generate squeezed phonons, vanishing squeezing parameter ($r \to 0$), the amplitudes of the two frequency components become,

$$\begin{aligned} |A_\Omega(\tau)| \;=\; & \frac{1}{2}\sqrt{I_y}\,z\,e^{-\lambda\tau/2}\,|\sin(2\|\bar{\alpha}'\|) \\ & + 2\sin(2\|\bar{\alpha}'\|)\sin^2(\|\bar{\alpha}'\|)\left(n-(n-n')e^{-\lambda\tau}\right)\Big|\ , \end{aligned} \quad (4.18)$$

$$|A_{2\Omega}(\tau)| = 0\ , \quad (4.19)$$

indicating the absence of the 2Ω frequency component in the variance in absence of phonon squeezing.

From equations (4.17) and (4.15) one can notice that the damping constant λ, characterizing the dissipative phonon time evolution between the excitation and the probing process, contributes differently to $A_{2\Omega}$ and to A_{Ω}, giving rise to different decay times for the two components and reproducing the experimental results.

4.5 Conclusions

Our novel experimental approach allows for the direct measurement of the photon number quantum fluctuations of the probing light in the shot-noise regime and our fully quantum model for time domain experiments maps the phonon quantum fluctuations into such photon number quantum fluctuations, thereby providing an absolute reference for the vibrational quantum noise. The comparison of the predicted noise with the experimental photon number quantum uncertainty, measured in shot-noise conditions, allows us to unveil non classical vibrational states produced by photo-excitation. A future extension of the model taking into account the role of the electronic degrees of freedom would allow to extend such a study from transparent materials to complex absorbing systems.

In conclusion, a Raman active phonon mode has been impulsively excited via ISRS in a α-quartz by means of a pump and probe transmittance experiment with single pulse differential acquisition in noise conditions limited by intrinsic probe photon number fluctuations. A fully quantum mechanical effective model where both phonons generation and detection are studied through the same effective coupling Hamiltonian establishes a direct connection between the measured photon number quantum fluctuations of the emitted probe field and the fluctuations of the atomic positions in a real material. Our novel approach is used here to reveal distinctive quantum properties of vibrational states in matter, in particular the squeezed nature of photo-excited phonon states in α-quartz. Finally, we stress that our innovative approach paves the way for future studies addressing the role of unconventional vibrational states in complex systems[33,34], and the thermodynamics of vibrational states[35,36] possibly in the quantum regime.

References

[1] Dhar, Rogers, and Nelson. Time-resolved vibrational spectroscopy in the impulsive limit. *Chem. Rev.*, 94:157, 1994.

[2] Beaud P. Vorobeva E. Milne C. J. Murray É. D. Fahy S. Johnson, S. L. and G. Ingold. Directly observing squeezed phonon states with femtosecond x-ray diffraction. *Phys. Rev. Lett.*, 102:175503, 2009.

[3] Trigo M. Chollet M. Clark J. N. Fahy S. Glownia J. M. Jiang M. P. Kozina M. Liu H. Song S. Zhu D. Reis D. A. Henighan, T. How to distinguish squeezed and coherent phonons in femtosecond x-ray diffuse scattering. *Preprint at http://arxiv.org/abs/1510.02403*, 2015.

[4] M. et al. Trigo. Fourier-transform inelastic x-ray scattering from time- and momentum-dependent phonon-phonon correlations. *Nat. Phys.*, 9:790–794, 2013.

[5] R. Merlin. Generating coherent thz phonons with light pulses. *Solid State Communications*, 102:207 – 220, 1997. doi: http://dx.doi.org/10.1016/S0038-1098(96)00721-1. URL http://www.sciencedirect.com/science/article/pii/S0038109896007211.

[6] E. Papalazarou, J. Faure, J. Mauchain, M. Marsi, A. Taleb-Ibrahimi, I. Reshetnyak, A. van Roekeghem, I. Timrov, N. Vast, B. Arnaud, and L. Perfetti. Coherent phonon coupling to individual bloch states in photoexcited bismuth. *Phys. Rev. Lett.*, 108:256808, 2012. doi: 10.1103/PhysRevLett.108.256808. URL http://link.aps.org/doi/10.1103/PhysRevLett.108.256808.

[7] J. J. Li, J. Chen, D. A. Reis, S. Fahy, and R. Merlin. Optical probing of ultrafast electronic decay in bi and sb with slow phonons. *Phys. Rev. Lett.*, 110:047401, 2013. doi: 10.1103/PhysRevLett.110.047401. URL http://link.aps.org/doi/10.1103/PhysRevLett.110.047401.

[8] Andrew M Weiner, Gary P Wiederrecht, Keith A Nelson, and DE Leaird. Femtosecond multiple-pulse impulsive stimulated raman scattering spectroscopy. *JOSA B*, 8(6):1264–1275, 1991.

[9] H. J. Zeiger, J. Vidal, T. K. Cheng, E. P. Ippen, G. Dresselhaus, and M. S. Dresselhaus. Theory for displacive excitation of coherent phonons. *Phys. Rev.*

B, 45:768–778, 1992. doi: 10.1103/PhysRevB.45.768. URL http://link.aps.org/doi/10.1103/PhysRevB.45.768.

[10] Ahmed I. Lobad and Antoinette J. Taylor. Coherent phonon generation mechanism in solids. *Phys. Rev. B*, 64:180301, 2001. doi: 10.1103/PhysRevB.64.180301. URL http://link.aps.org/doi/10.1103/PhysRevB.64.180301.

[11] Xuedong Hu and Franco Nori. Phonon squeezed states generated by second-order raman scattering. *Phys. Rev. Lett.*, 79:4605–4608, 1997. doi: 10.1103/PhysRevLett.79.4605. URL http://link.aps.org/doi/10.1103/PhysRevLett.79.4605.

[12] O. V. Misochko, K. Sakai, and S. Nakashima. Phase-dependent noise in femtosecond pump-probe experiments on bi and gaas. *Phys. Rev. B*, 61: 11225–11228, 2000. doi: 10.1103/PhysRevB.61.11225. URL http://link.aps.org/doi/10.1103/PhysRevB.61.11225.

[13] Huedong Xu and Franco Nori. Quantum phonon optics: coherent and squeezed atomic displacements. *Phys. Rev. B*, 53:2419–2424, 1996.

[14] Daniels J. M. Reiter D. E. Kuhn T. Vagov A. Sauer, S. and V. M. Axt. Lattice fluctuations at a double phonon frequency with and without squeezing: an exactly solvable model of an optically excited quantum dot. *Phys. Rev. Lett.*, 105:157401, 2010.

[15] M. Esposito, K. Titimbo, K. Zimmermann, F. Giusti, F. Randi, D. Boschetto, F. Parmigiani, R. Floreanini, F. Benatti, and Fausti D. Photon number statisctics uncover the fluctuations in non-equilibrium lattice dynamics. *Nature Communication*, 6(10249). doi: 10.1038/ncomms10249. URL http://dx.doi.org/10.1038/ncomms10249.

[16] Jim Clark. The structure of silicon dioxide. http://www.chemguide.co.uk/atoms/structures/giantcov.html, 2009. [Online; accessed 23-November-2015].

[17] Scott and Porto. Longitudinal and transverse optical lattice vibrations in quartz. *Physical Review*, 161, 1967.

[18] Kuhl J. Stevens, T. E. and R. Merlin. Coherent phonon generation and the two stimulated raman tensors. *Phys. Rev. B*, 65:144304, 2002.

[19] Marc M. Wefers, Hitoshi Kawashima, and Keith A. Nelson. Optical control over two-dimensional lattice vibrational trajectories in crystalline quartz. *JOURNAL OF CHEMICAL PHYSICS*, 108, 1998.

[20] P. Umari, Alfredo Pasquarello, and Andrea Dal Corso. Raman scattering intensities in α-quartz: A first-principles investigation. *Phys. Rev. B*, 63: 094305, 2001. doi: 10.1103/PhysRevB.63.094305. URL http://link.aps.org/doi/10.1103/PhysRevB.63.094305.

[21] Andy Rundquist, Jon Broman, David Underwood, and David Blank. Polarization-dependent detection of impulsive stimulated raman scattering in alpha-quartz. *Journal of Modern Optics*, 52, 2006.

[22] Shaul Mukamel. *Principles of Nonlinear optical spectoscopy*. Oxford University Press, 1995.

[23] Huedong Xu and Franco Nori. Squeezed phonon states: Modulating quantum fluctuations of atomic displacements. *Phys. Rev. Lett.*, 76:2294–2297, 1996.

[24] Xuedong Hu and Franco Nori. Phonon squeezed states: quantum noise reduction in solids. *Physica B: Condensed Matter*, 263-264:16–29, 1999. doi: 10.1016/S0921-4526(98)01483-5.

[25] G. Garrett, A. Rojo, A. Sood, J. Whitaker, and R. Merlin. Vacuum Squeezing of Solids: Macroscopic Quantum States Driven by Light Pulses. *Science*, 275(5306):1638–1640, 1997. doi: 10.1126/science.275.5306.1638. URL http://dx.doi.org/10.1126/science.275.5306.1638.

[26] Gregory Garrett, John Whitaker, Ajay Sood, and Roberto Merlin. Ultrafast optical excitation of a combined coherent-squeezed phonon field in srtio3. *Opt. Express*, 1(12):385–389, 1997. doi: 10.1364/OE.1.000385. URL http://www.opticsexpress.org/abstract.cfm?URI=oe-1-12-385.

[27] O. V. Misochko. Nonclassical states of lattice excitations: squeezed states and entangled phonons. *Phys. Usp.*, 183:917–933, 2013.

[28] A. Hussain and S. R. Andrews. Absence of phase-dependent noise in time-domain reflectivity studies of impulsively excited phonons. *Phys. Rev. B*, 81: 224304, 2010. doi: 10.1103/PhysRevB.81.224304. URL http://link.aps.org/doi/10.1103/PhysRevB.81.224304.

[29] Wigger D. Axt V. M. Reiter, D. E. and T. Kuhn. Generation and dynamics of phononic cat states after optical excitation of a quantum dot. *Phys. Rev. B*, 88:195327, 2011.

[30] Kelvin Titimbo. Creation and detection of squeezed phonons in pump and probe experiments: A fully quantum treatment, 2015.

[31] R. Alicki and K. Lendi. *Quantum Dynamical Semigroups and Applications*. Springer-Verlag, Berlin, 2007.

[32] H.-P. Breuer and F. Petruccione. *Quantum Optics*. Oxford University Press, New York UK, 2002.

[33] D. M. Newns and C. C. Tsuei. Fluctuating cu-o-cu bond model of high-temperature superconductivity. *Nature Physics*, 184(191):1745–2473, 2007.

[34] K Alex Müller, W Berlinger, and E Tosatti. Indication for a novel phase in the quantum paraelectric regime of srtio3. *Zeitschrift für Physik B Condensed Matter*, 84(2):277–283, 1991.

[35] Hänggi P. Campisi, M. and P. Talkner. *Colloquium* : Quantum fluctuation relations: Foundations and applications. *Rev. Mod. Phys.*, 83:771–791, 2011.

[36] Huber M. Riera A. Del Rio L. Goold, J. and Skrzypczyk P. The role of quantum information in thermodynamics — a topical review. *Preprint at http://arxiv.org/abs/1505.07835*, 2015.

5

Non-equilibrium quantum state tomography

Studying the quantum state of collective excitations, like lattice atomic vibrations, in solid state physics is a fundamental tool to understand the microscopic origin of macroscopic material proprieties. In the recent years the development of laser cooling technologies allowed to control, manipulate and measure[1] non-classical quantum states associated with the lowest energy vibrations of few single atoms artificially trapped. However, even when a large number of atoms, of the order of 10^{23}, are arranged in a real crystal, they can still manifest their quantum nature. Quantum fluctuations of collective atomic vibrations in crystals play indeed a leading role in the onset of many intriguing material proprieties[2–8]. We propose an experimental method to access non-classical phonon quantum states in crystals through the measurement of the photon quantum state of probing light[9]. The method, that we called "pump probe quantum state tomography", allows to study the evolution on the probing photon quantum state after the interaction with the photo-excited material[10]. In this Chapter the preliminary results of this experimental approach are reported.

5.1 Introduction

Optical homodyne tomography is a method extensively used in quantum optics to reconstruct quantum states of light[11]. Here we exploit such a technique in the framework of pump-probe spectroscopy for the study of ultra-fast dynamics of phonons in condensed matter. In the previous Chapter we demonstrated that the measurement of the quantum statistical distribution of the number of probing

photons can reveal the squeezed nature of the photo-excited phonons in transparent materials.

Here we extend such a study, adopting an experimental apparatus which combines quantum optics techniques with ultrafast solid state spectroscopy. In this case we have access not only to the photon number statistics, but also to the statistical distribution of any observable of the scattered light, since a fully optical quantum state reconstruction is performed.

The conceptual step to do is to connect the single pulse acquisition pump-probe experiment (Section 4.3) is series with the balanced homodyne detection experiment (Section 3.2) for optical quantum state tomography. Such a conceptual passage easily turns into an "hybrid" experimental approach, that we call *pump-probe quantum state tomography*. A scheme of this experimental combination is shown in Fig 5.1.

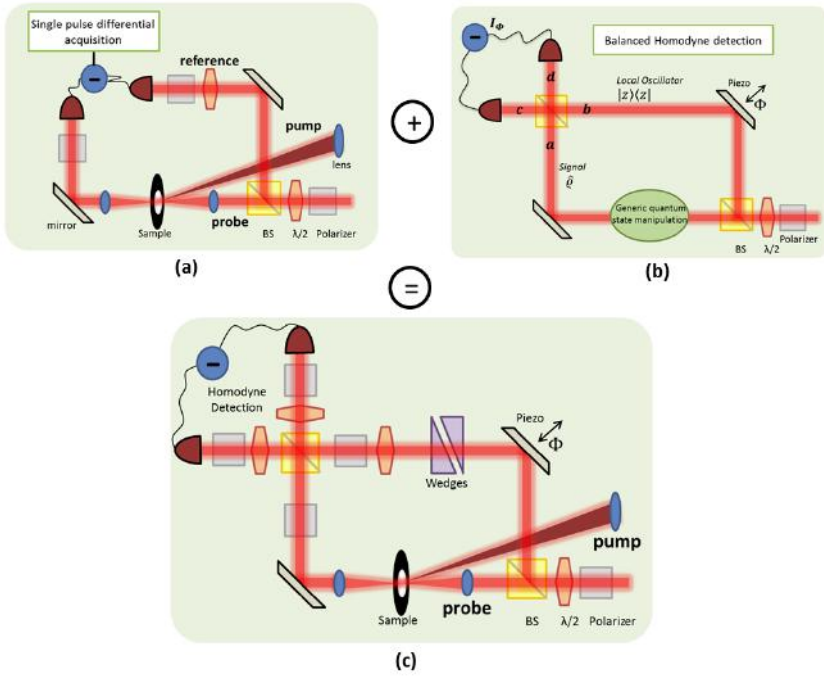

Figure 5.1: Pump probe quantum state tomography setup. The combination between the experimental schemes in (a) (single pulse acquisition pump-probe experiments) and in (b) (Mach-Zehnder interferometer for balance homodyne detection experiments) gives rise to the experimental set up in (c) for the pump-probe quantum state tomography.

The experiment can be divided in two consecutive parts.

(i) The sample under investigation is driven out of the equilibrium by an intense laser pulse, the pump. At a precise delay time after the perturbation a second laser pulse, the probe, interacts with the material and is scattered carrying information

about the photo-excited system.

(ii) Each transmitted probe pulse, that here we call *signal* pulse, is made interfere with a local oscillator (LO) pulse through a 50/50 beam-splitter. Finally the two beam-splitter output pulses are acquired with two photodiodes and the difference between the two generated photo-voltages, homodyne photo-voltage V_Φ, is measured. This acquisition can be repeated for different phase values Φ, which represents the phase difference between the signal and the local oscillator. The second part of the experiment constitutes the balanced homodyne detection part. In particular, it can be proven that, when the LO is significantly more intense than the *signal*, the homodyne photo-voltage V_Φ is proportional to the *signal* quadrature (Section 3.2). Denoting by $\hat{A}$ and $\hat{A}^\dagger$ the photonic annihilation and creation operators associated with the *signal*, the quadrature operator is defined as,

$$\hat{x}_\Phi = \frac{\hat{A}e^{-i\Phi} + \hat{A}^\dagger e^{i\Phi}}{\sqrt{2}} \ , \tag{5.1}$$

where Φ is the relative phase between the *signal* and the LO. The passage from the measured V_Φ to the field quadratures x_Φ happens through a calibration with respect to the vacuum state[12]. The continuum set of quadratures with $\Phi \in [0, \pi]$ provides a complete characterization of the *signal* quantum state. This means that by processing the results of repeated V_Φ measurements for different $\Phi \in [0, \pi]$ through appropriate tomographic technique the quantum state of the signal can be retrieved.

With this approach we can really monitor the evolution of the signal quantum state after the interaction with the material at different temporal distances from the pump perturbation.

Notice that in the experiment presented in the previous Chapter, sketched in Fig 5.1 (a), at a given pump-probe delay time, several consecutive probe transmitted pulses are singulary acquired. In this case, Fig 5.1 (c), they are not only simply acquired, but each pulse undergoes a balanced homodyne detection measurement.

Here we test this novel experimental approach considering a prototype transparent material, quartz.

The Chapter is organized as follows,

- The experiment is described in detail and the raw homodyne data are presented (Section 5.2).
- The analysis of the raw homodyne data which allows to pass from the measured photovoltage V_Φ to the field quadratures x_Φ in equation (5.1) is reported (Section 5.3).
- The procedure that from the field quadrature data allows to retrieve the quantum state of the scattered probing light as a function of time is presented and the results are shown (Section 5.4).
- The preliminary comparison with the model predictions is reported (Section 5.5).

5.2 Experiment

The experiment has been performed on 1 mm thick α-quartz sample at room temperature. Both pump and probe pulses are generated from the same pulsed laser source and are characterized by 800 nm wavelength, 250 kHz repetition rate and 80 fs pulse duration. In order to excite the E-symmetry Raman active mode in α-quartz we adopt a suitable configuration for the sample orientation and for the pump and probe polarizations[13]. In particular, the pump and probe are linearly polarized at 45° one with respect to the other. In this way, through the process of impulsive stimulate Raman scattering (ISRS), the phonon excitation generates an emitted field with polarization orthogonal to the probe one.

The emitted field carries information about the photo-excited material and the adopted symmetries configuration allows us to discriminate the unscattered probe from the emitted field by exploiting the orthogonality of the polarizations. Such a configuration is shown in Fig 5.2.

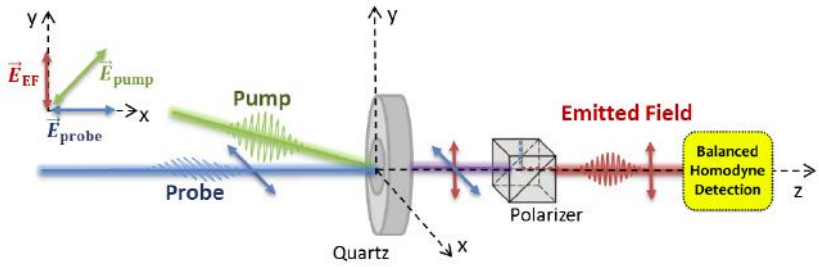

Figure 5.2: Experimental polarization configuration. The sample is depicted at the origin of the coordinates. The c-axis of the crystal correspond to the z-axis of the coordinate system. The polarization configuration of pump, probe and emitted field is indicated on top-left. After the interaction with the sample the probe undergoes a polarization selection in order to have in output the emitted field only.

This configuration for $\alpha-$quartz guarantees the excitation via ISRS of the E-symmetry Raman mode with frequency $\nu_{\mathrm{E}} = 3.84\,\mathrm{THz}$ (see Section 4.2).

A detailed scheme of the opto-mechanical setup is shown in Fig 5.3. One can notice that the setup is divided in two parts.
The first consists in a typical pump-probe opto-mechanical scheme. The beam coming from the laser source is split in two beams, the pump beam and the probe beam and a delay line (mechanical slit) is mounted on one of the paths in order to control the delay time τ between the pump and probe pulses at the arrival on the sample.
The second part consist in a Mach-Zehnder interferometric scheme. In this case the pump beam plays no role since it is blocked after the sample. It is the probe beam that, before the interaction with the sample, is splitter in two parts which constitute the two arms of the interferometer. The sample is placed in one of the arm of the interferometer, the probe transmitted by the sample undergoes a

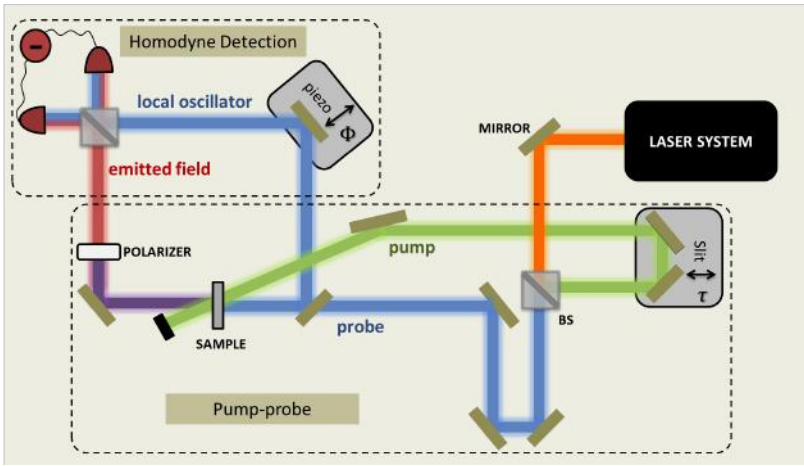

Figure 5.3: Scheme of the opto-mechanical setup. Combination between pump-probe and homodyne detection experiments.

polarization filtering in order to select only the emitted field generated from the non-linear interaction with the material.

The emitted field takes thus the role of the signal in the homodyne detection, while the beam which travels through the second arm of the interferometer represents the LO. The phase difference Φ between the two fields can be controlled with a piezo linear stage (*PI P622-ZCD*) mounted in the LO arm. The signal and the LO interfere on the last beam-splitter and the homodyne photo-vaoltage can be measured. Due to the low efficiency of the ISRS process, the emitted field (the signal) is much weaker than the LO. This condition guarantees that the measured homodyne photo-voltages can be related to the signal quadrature as $V_\Phi = \gamma' x_\Phi$, where γ' is the vacuum calibration constant[12] (see Section 3.4.1).

In this framework there are two main experimental quantities that can be controlled, the delay time τ between the pump and the probe pulses, and the phase difference Φ between the signal transmitted through the sample and the local oscillator in the Mach-Zehnder interferometer. For a specific time delay τ and a given phase Φ, $N = 800$ measurements of homodyne photo-voltages $[V_\Phi(\tau)]_i$ are acquired (each measurement correspond with a single acquired pulse).

The acquisition system is made of a balanced amplified differential photodetector and a fast digitizer (*Spectrum* M3i.2132-exp) with sampling rate 1 GS s^{-1}. The differential photodetector consists of two *Hamamatsu S3883* Silicon PIN photodiodes with 0.94 quantum efficiency connected in reverse bias and followed by a low-noise charge amplifier. The photo-currents generated by the two photodiodes in response to a single optical pulse impinging on them are physically subtracted and the resulting charge is amplified using *CAEN* custom designed electronic components. The photo-voltage acquired for every single differential pulse acquisition, $[V_\Phi]_i$, is the sum of the voltages digitized for 500 points at 1 GS s^{-1}. Details about the detection-acquisition system are reported in Appendix A.

5.2.1 Raw data

A typical experimental result is shown in Fig 5.4. A color-plot of the average of the N acquired photo-voltages, $\overline{V}_\Phi(\tau) = \sum_i^N \frac{1}{N}[V_\Phi(\tau)]_i$, is shown as a function of the homodyne phase Φ, on the vertical axis, and of the pump-probe delay time τ, on the horizontal axis. The displayed data are the result of the average of $M = 5$ repeated scans. This measurement has been obtained with a pump fluence on the

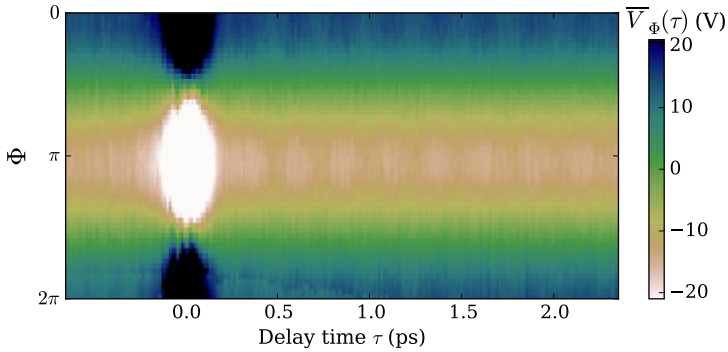

Figure 5.4: Photo-voltages average. $\overline{V}_\Phi(\tau)$ as a function of the homodyne phase Φ, on the vertical axis, and of the pump-probe delay time τ, on the horizontal axis.

sample of about $25\,\mathrm{mJcm^{-2}}$ (700 mW pump power for $60\,\mu$m pump spot radius) and a probe fluence on the sample of about $0.2\,\mu\mathrm{Jcm^{-2}}$ ($2\,\mu$W probe power for $40\,\mu$m probe spot radius).

In Fig 5.5 the behaviour of $\overline{V}_\Phi(\tau)$ for a specific phase $\Phi = \pi$ is shown. This correspond to an horizontal cut in the data-set shown in Fig 5.4. The zero time

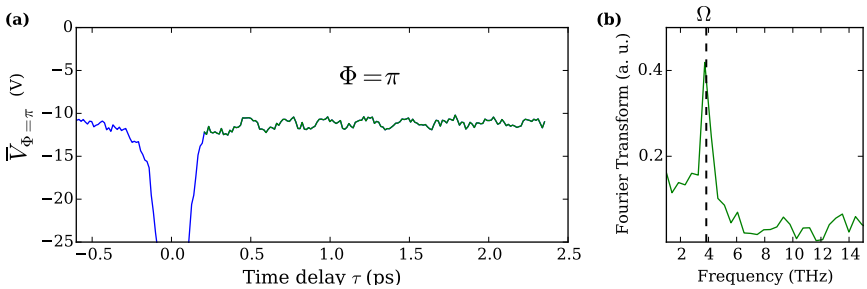

Figure 5.5: Average homodyne photo-voltage for $\Phi = \pi$. (a) $\overline{V}_{\Phi=\pi}(\tau)$. (b) Fourier transform of the oscillating part (signal in green); the dashed line indicates the value of the phonon frequency Ω.

represents the instant in which pump and probe arrives simultaneously on the sample. The response around time zero is not physically meaningful since it is due to saturation effects of the acquisition systems in presence of a high intensity due to scattering effects of the pump. What is indeed meaningful is the behaviour at

positive times. It is characterized by an oscillating response at the frequency of the photo-excited phonon $\Omega = 3.84\,\mathrm{THz}$. The Fourier transform of the oscillating part of the signal (green in Fig 5.5) displays a peak at Ω.

Since for a given phase Φ and a given time τ we acquire the photo-voltage for $N = 800$ repeated pulses, we have enough statistics to be able to calculate in addition to the mean also the variance. In Fig 5.6 a color-plot of the variance of the N acquired photo-voltages, $V_\Phi^{\mathrm{var}}(\tau) = \sum_i^N \frac{1}{N}\left[[V_\Phi(\tau)]_i - \overline{V}_\Phi(\tau)\right]^2$, is shown as a function of the homodyne phase Φ, on the vertical axis, and of the pump-probe delay time τ, on the horizontal axis. The displayed data are again the result of the

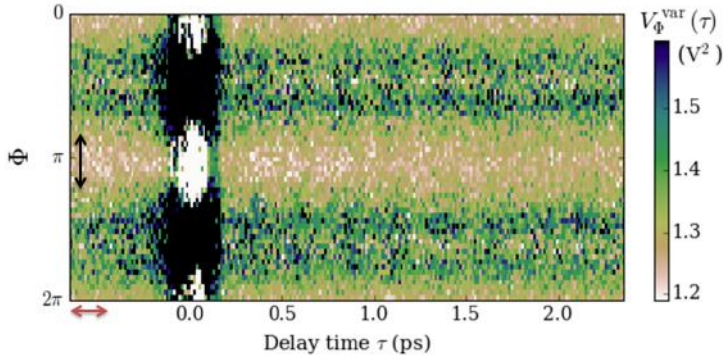

Figure 5.6: Photo-voltages variance. $V_\Phi^{\mathrm{var}}(\tau)$ as a function of the homodyne phase Φ, on the vertical axis, and of the pump-probe delay time τ, on the horizontal axis.

average of $M = 5$ repeated scans. In detail, for each scan we calculate $V_\Phi^{\mathrm{var}}(\tau)$ and the average over all the scan is performed.

In Fig 5.7 the time dependent behaviour of $V_\Phi^{\mathrm{var}}(\tau)$ for a specific phase $\Phi = \pi$ is shown. In particular, since the variance is more noisy than the average, in Fig

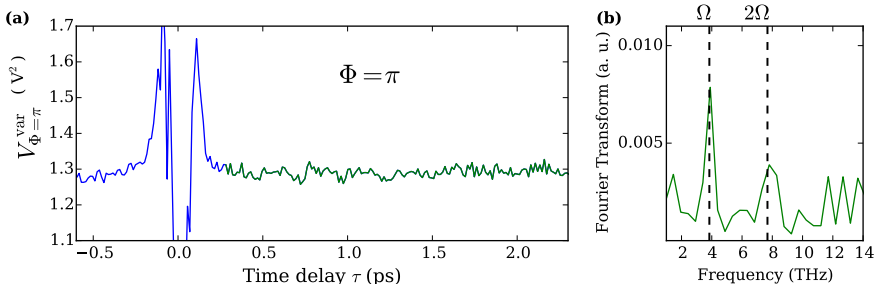

Figure 5.7: Variance homodyne photo-voltage for $\Phi = \pi$. (a) $V_\Phi^{\mathrm{var}}(\tau)$ for $\Phi = \pi$ (average of 16 rows in Fig 5.6). (b) Fourier transform of the oscillating part (signal in green); the dashed line indicates the value of the phonon frequency Ω and of the frequency 2Ω.

5.7 we consider the average of several adjacent phases. In detail we averaged 16

phases around the value $\Phi = \pi$ corresponding to the range of rows indicated by the black arrow in Fig 5.6.

The results show that even in the variance of the signal a modulation in time is present. In particular the Fourier transform of the variance homodyne photovoltage for $\Phi = \pi$ presents a peak at the phonon frequency and also a smaller but significant frequency component at twice the phonon frequency.

5.2.2 A phase sensible technique

Another information one can extract directly from the raw data is the phase of the optical field as a function of the pump-probe delay time. The homodyne detection is indeed a phase-sensible technique that allows for the measurement not only of the field amplitude but also of its phase.

In Fig 5.8 the phase Φ_0 as a function of the pump-probe time delay is shown. It is calculated as the best fit parameter obtained from the fit of the homodyne data with a function of the kind: $A\sin(\omega t + \Phi_0)$.

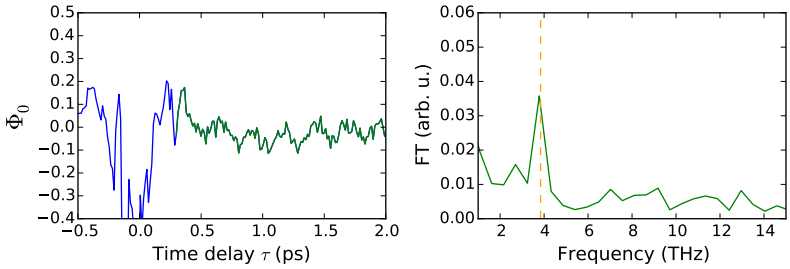

Figure 5.8: Phase Φ_0 of the emitted field as a function of the pump-probe time delay. The Fourier transform of the signal at positive times (signal in green) is reported on the left; the dashed line indicates the value of the phonon frequency Ω.

One can notice that the phase Φ_0 presents an oscillating component at the phonon frequency Ω.

5.3 Homodyne data analysis

In this section we focus on the procedure we adopt for the analysis of the raw homodyne data. The data analysis is divided in two subsequent steps:

1. the correction of the experimental artifacts;
2. the calibration of the corrected raw data with respect to the vacuum.

5.3.1 Correction of the experimental artifacts

The main experimental artifact to be corrected is associated with the fact that the variance in Fig 5.7 is phase dependent at negative times (before the arrival

of the pump). This behaviour is present even in absence of the sample, when in principle the analyzed light should be in a coherent state with no phase dependence of the photo-voltage variance. For this reason we attributed this behaviour to an experimental artifact. A deeper analysis of this effect is shown in Fig 5.9, where the average of the first 20 columns in Fig 5.6 is shown (the considered columns are indicated in Fig 5.6 with the red arrow).

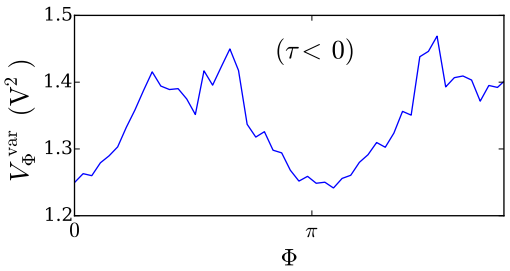

Figure 5.9: Photo-voltages variance at negative times. Average of the first 20 columns in Fig 5.6. The involved phases are indicated with a red arrow in Fig 5.6.

The phase dependence of the photo-voltage variance even at negative times is due to an experimental artifact. The error in the phase value, due to the error associate with the read piezo position, is mapped indeed in an error on the photo-voltage which is maximum at the maxima of the derivative of the signal. This causes the photo-voltage variance to be maximum in correspondence of the maxima of the derivative of the photo-voltage mean. We partially correct this experimental artefact with a proper data treatment. In detail, for each phase Φ, the photo-voltages are shifted of a quantity Δ_Φ which is the difference between the mean value $\overline{V}_\Phi$ and the value of a best fit sin function at Φ. This correction serves to exclude the classical noise which occurs between different phases, keeping only the intrinsic quantum noise between consecutive pulses. The effects of classical slow noise have been analyzed in detail in Appendix A, Fig A.6, where the noise increase as a function of the number of detected pulses is studied.

At the end of the procedure we redefine the photo-voltages V_Φ including the correction for the slow noise.

5.3.2 Vacuum calibration

As already discussed in Section 3.2, in order to calibrate the acquired homodyne data, one needs to consider a homodyne acquisition for the vacuum state as reference. In particular, indicating with $[V_{|0\rangle}]_i$ the homodyne photo-voltage for a single pulse i obtained keeping blocked the signal beam (vacuum homodyne detection), one can calculate the calibration constant as in equation (3.36) by assuming the variance of the vacuum quadrature to be 1/2. In this way the calibration constant results

$$\gamma' = \sqrt{2\, V_{|0\rangle}^{\mathrm{var}}}\,, \tag{5.2}$$

where $V_{|0\rangle}^{\text{var}} = \sum_i^N \frac{1}{N}\left[[V_{|0\rangle}]_i - \overline{V}_{|0\rangle}\right]^2$ is the variance of $N = 80000$ vacuum photo-voltages.

Thus, the quadrature calibration is the following:

$$x_\Phi = \frac{V_\Phi}{\gamma'} \ , \tag{5.3}$$

where the photo-voltage V_Φ already includes the correction for the experimental artifacts.

5.3.3 Corrected and calibrated homodyne data

Here we report the homodyne data after the correction for the experimental artifacts and the vacuum calibration.

In Fig 5.10 the average of the homodyne quadrature data is shown and in Fig 5.11 the time dependent behaviour is reported for a specific phase $\Phi = \pi$.

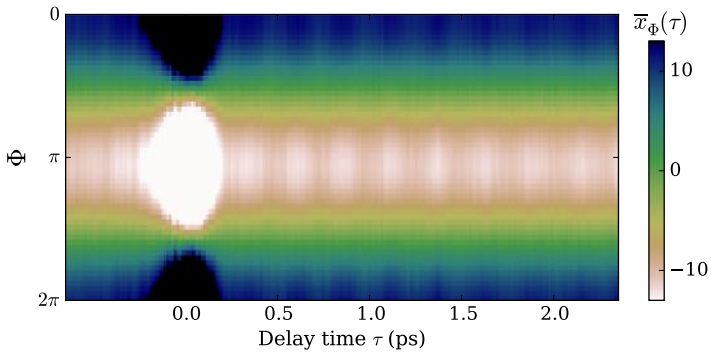

Figure 5.10: Quadratures average. $\overline{x}_\Phi(\tau)$ as a function of the homodyne phase Φ, on the vertical axis, and of the pump-probe delay time τ, on the horizontal axis.

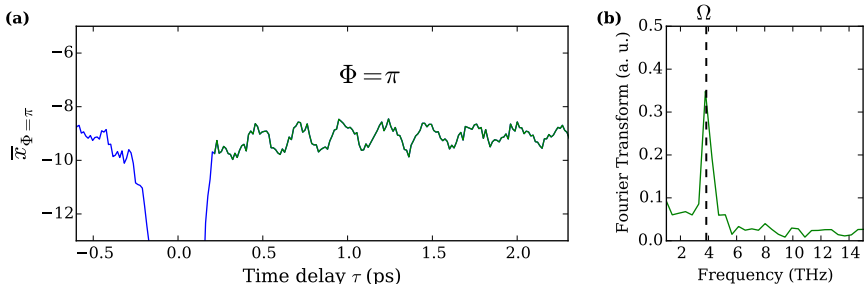

Figure 5.11: Average homodyne quadrature for $\Phi = \pi$. (a) $\overline{x}_\Phi(\tau)$ for $\Phi = \pi$. (b) Fourier transform of the oscillating part (signal in green); the dashed line indicates the value of the phonon frequency Ω.

One can notice that the behaviour of the quadratures average is similar to the one of the uncorrected and uncalibrated photo-voltages average in Fig 5.4 and 5.5.

On the contrary, the result of the data analysis is noticeable in the variance. In Fig 5.12 the variance of the calibrated quadrature data is shown.

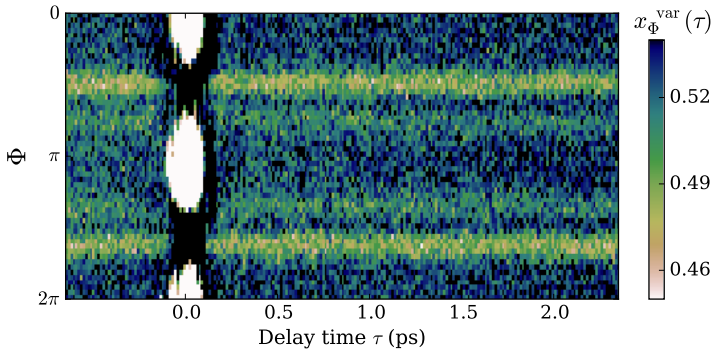

Figure 5.12: Quadrature variance. $x_\Phi^{\mathrm{var}}(\tau)$ as a function of the homodyne phase Φ, on the vertical axis, and of the pump-probe delay time τ, on the horizontal axis.

One can notice that, after the correction for the classical noise sources, the artifact of the phase dependence of the quadrature variance at negative times is now less evident than in Fig 5.6.

The time dependent behaviour for a specific phase $\Phi = \pi$ is reported in Fig 5.13.

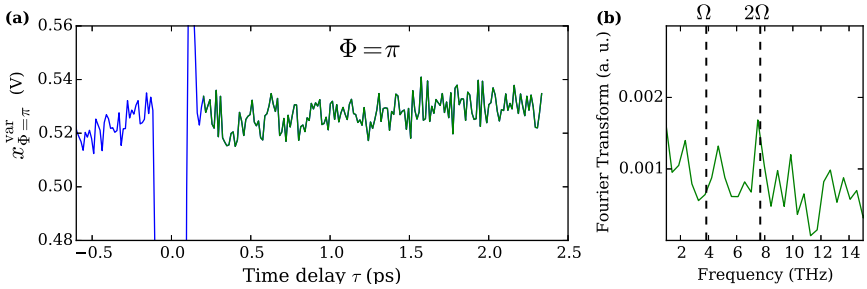

Figure 5.13: Variance homodyne quadrature for $\Phi = \pi$. (a) $x_\Phi^{\mathrm{var}}(\tau)$ for $\Phi = \pi$. (b) Fourier transform of the oscillating part (signal in green); the dashed line indicates the value of the phonon frequency Ω and of the frequency 2Ω.

The results indicate that after the homodyne data analysis the Ω component in the variance homodyne quadrature for $\Phi = \pi$ is repressed while probably the frequency component at 2Ω is still contributing to the signal.

We stress that the reported preliminary results are still not conclusive since work about the possibility of improving the data analysis and the experimental artifacts correction is still in progress.

5.4 Time domain Wigner function reconstruction

In the previous sections we presented the the experimental procedure and the output data in terms of the statistical proprieties like the average and the variance. This section is about the tomographic method that from the homodyne data allows for the optical quantum state reconstruction. For each delay time τ, we acquire the homodyne photo-voltages, V_Φ, as a function of the homodyne phase Φ. In particular, for each phase value we measure $N = 800$ subsequent pulses. In Fig 5.4 and 5.6 we have shown the average and the variance associated with these 800 measurements. Here we consider instead the entire distribution of the measurements.

In Fig 5.14 the histogram plot of the 800 measurements is shown for each phase value and for a specific time delay $\tau = 0.5$ fs. The average $\overline{V}_\Phi = \sum_i^N \frac{1}{N}[V_\Phi]_i$ is also

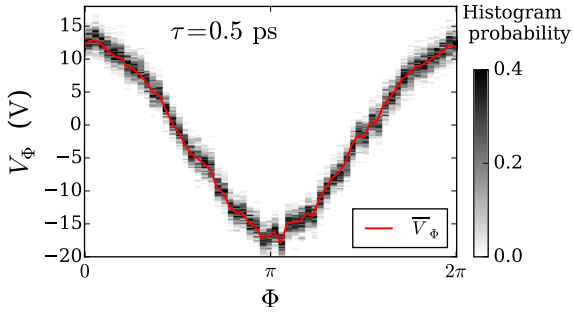

Figure 5.14: Histogram plot of the measured homodyne photo-voltages at delay time $\tau = 0.5$ ps. For each phase value Φ the histogram is representative of $N = 800$ acquired pulses. The average $\overline{V}_\Phi = \sum_i^N \frac{1}{N}[V_\Phi]_i$ is shown in red.

shown in red. The latter represents a vertical cut in the data-set shown in Fig 5.4.

The homodyne photo-voltages after the data analysis described in Section 5.3 become homodyne quadratures. In Fig 5.15 the analyzed and calibrated homodyne quadrature data correspondent to the raw data in Fig 5.14 are shown.

The data in Fig 5.15 represent a typical data-set in balanced homodyne detection. The peculiarity of our experiment is that we perform repeated homodyne experiments for each pump probe time delay.

The homodyne data in Fig 5.15 are fed to a quantum tomographic algorithm which allows the reconstruction of the quantum state (in terms of the Wigner function) of the emitted optical field for the delay time value $\tau = 0.5$ ps. This procedure is repeated for each pump-probe delay time.

The Wigner functions are thus reconstructed for each time delay τ starting from the homodyne quadrature data. The reconstruction is obtained by exploiting a tomographic method based on the inverse Radon transform algorithm[11]. The specific algorithm adopted here is the one developed in reference[14] and optimized for homodyne efficiencies lower than one.

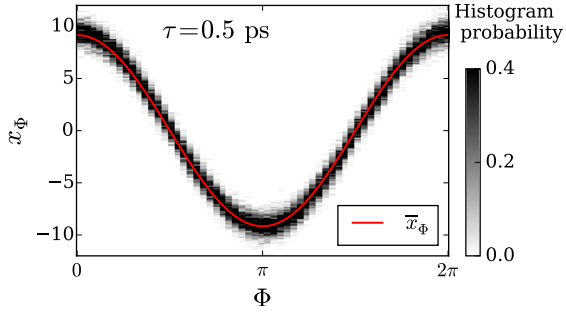

Figure 5.15: Histogram plot of the measured homodyne quadratures at delay time $\tau = 0.5$ ps. For each phase value Φ the histogram is representative of $N = 800$ acquired pulses. The average $\overline{x}_\Phi = \sum_i^N \frac{1}{N}[x_\Phi]_i$ is shown in red.

The homodyne efficiency depends on the noise performances of the differential detector. In our case, from the detector shot-noise characterization reported in Section A.1, we estimate a homodyne equivalent efficiency $\eta_{\text{eq}} \approx 0.85$ in correspondence of a single channel pulse peak of about 1.2 V (Fig A.5). The tomographic method for the Wigner function reconstruction has been presented in detail in Section 3.3.1.

In Fig 5.16 the reconstructed Wigner functions for a single scan at different pump-probe delay times are reported. The Wigner function provides the maximum

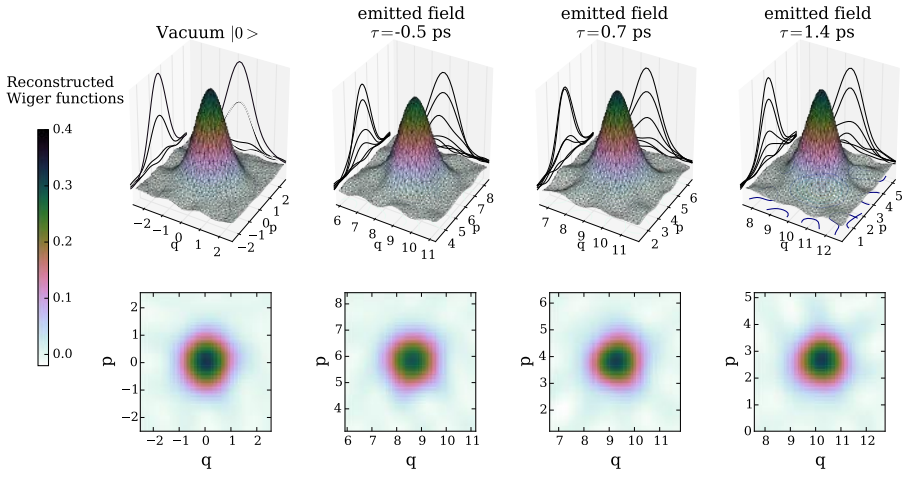

Figure 5.16: Reconstructed Wigner functions (a) Reconstructed Wigner function of the vacuum state. (b), (c), (d) Reconstructed Wigner functions of the emitted field for different delay times τ.

information about the quantum state of the emitted field. Once known the Wigner function one can indeed calculate the expectation value of any observable of the system (see Section 2.2.1).

In Fig 5.17 we show the expectation values as a function of pump-probe time delay of significant observables of the emitted field, the position and the momentum operators, $\hat{q}$ and $\hat{p}$ (see definition in equation (2.14)), their variances, $\sigma^2_{\hat{q}}$ and $\sigma^2_{\hat{p}}$, and a quantity associated to the ratio between the two variances, $\frac{1}{4}\log(\sigma^2_{\hat{p}}/\sigma^2_{\hat{q}})$. The latter gives an indication of the squeezing of one uncertainty with respect to the other*.

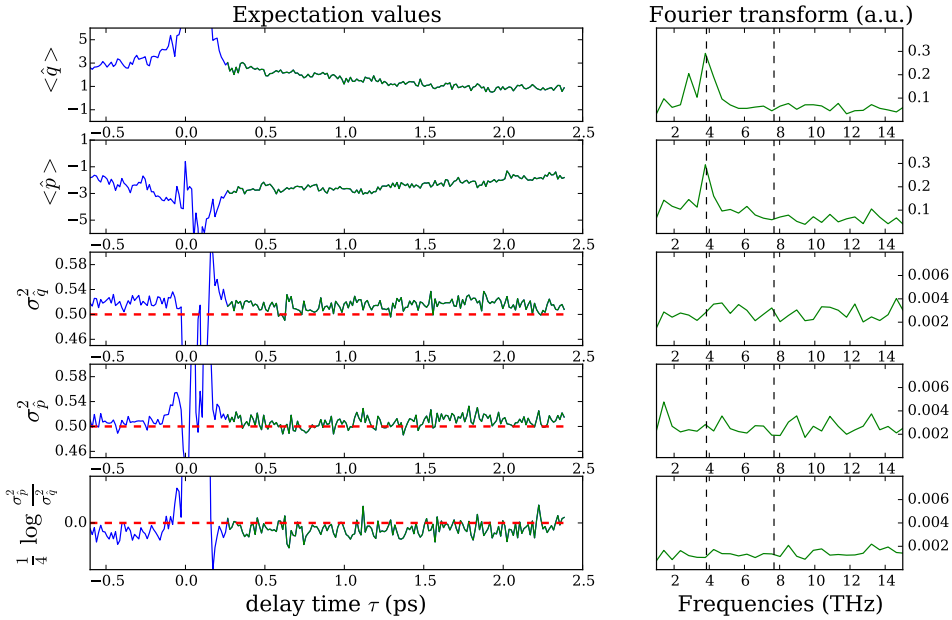

Figure 5.17: Expectation values of meaningful observables of the emitted field. Expectation values as a function of the delay times τ of the position operator, momentum operator and of their variances. The Fourier transform of the signal at positive times (signal in green) is reported on the left; the dashed line indicates the value of the phonon frequency Ω and of the frequency 2Ω. The signal is averaged over 5 scans and the FT is the average of the FTs.

The reported results are still preliminary and much can still be done to improve the correction for the experimental artifacts. In particular, it is possible to note a slow drift in the position and momentum operator which can be attributed to a slow shift in the phase of the emitted field due to thermal instabilities of the

*The expression $\frac{1}{4}\log\left(\frac{\sigma^2_{\hat{p}}}{\sigma^2_{\hat{q}}}\right)$ becomes the correct definition of the squeezing parameter only when $\sigma^2_{\hat{p}}$ and $\sigma^2_{\hat{p}}$ the eigenvalues of the covariance matrix in (2.33).

opto-mechanics.

However what emerges from Fig 5.17 at this stage is an oscillation of the position and momentum operator at the phonon frequency. This observation, together with the oscillation of the phase of the emitted field (Fig 5.8) suggests a rotation of the Wigner function around a point in the phase space at the phonon frequency.

The variances of the position and momentum operators do not present instead significate behaviours in time, at least at this stage of the analysis. The values of $\sigma^2_{\hat{q}}$ and $\sigma^2_{\hat{p}}$ are almost stable around the value 0.5, expected for a coherent optical state. However, the fact that the variance of the homodyne data before the tomographic process (Fig 5.13) presents instead a 2Ω oscillating component stimulate us in improving the data analysis with the aim to obtain consistent results from the unprocessed homodyne data and from the result of the tomographic process.

5.5 Comparison with the model

The core of the experiment presented in this Chapter is the quantum state reconstruction of probing light after the interaction with a photo-excited material.

In order to properly describe the experiment it is thus necessary to adopt a quantum description of the electromagnetic fields involved in the process. The effective fully quantum model for ISRS presented in Section 2.7 satisfies such a requirement [15]. It allows indeed to describe both the excitation and the detection of phonon states via impulsive stimulate Raman scattering experiments. In particular, the model maps the quantum state of the photo-excited phonon into the quantum state of the transmitted probing optical pulses. This quantity is exactly what we measure in the experiment presented in the previous section. The model describes first the pump process, then the phonon dynamics and finally the probe process.

The analysis of our preliminary experimental results in comparison with the model are still under investigation. For this reason here we report only the main ingredients necessary to describe the experiment through the model [15].

We focus on the description of the probe process and on the analysis of the quantum state of the transmitted probing optical pulses. In particular, we present the model predictions for the time dependent behaviour of significant observables of the emitted field which have been experimentally obtained from the Wigner function reconstruction. The details of the model are reported in Section 2.7.

The probe process is described by the impulsive unitary operator

$$\mathcal{U}_{\text{probe}} = \mathcal{U}_{\bar{\alpha}'} = \exp\{-i\|\bar{\alpha}'\|\left(\hat{A}\,\hat{b}^\dagger + \hat{A}^\dagger\,\hat{b}\right)\}\ , \tag{5.4}$$

where $\hat{A}$ is the collective photon annihilation operator defined in (2.85) and $\hat{b}$ the annihilation phonon operator of the photo-excited vibrational mode (see also equation (2.84)).

The evolution operator in (5.4) affects the collective photon-phonon initial state $|\bar{\alpha}_y\rangle\langle\bar{\alpha}_y| \otimes \hat{\rho}_{\text{phonon}}(\tau)$ $\hat{\rho}^{\bar{\nu}}_{\text{II}}(\tau)$, where $|\bar{\alpha}_y\rangle = |\alpha_{y\,-J}\rangle \otimes \cdots \otimes |\alpha_{y\,J}\rangle$ is the optical coherent state involving only the y polarization components of the probe and $\hat{\rho}_{\text{phonon}}(\tau)$ $\hat{\rho}^{\bar{\nu}}_{\text{II}}(\tau)$ is the phonon state at the instant τ after the photo-excitation.

The quantum state of the emitted optical field is then given by

$$\hat{\rho}_{\mathrm{I}}(\tau) = \mathrm{Tr}_{\mathrm{II}}\left(\mathcal{U}_{\mathrm{probe}}\,|\bar{\alpha}_y\rangle\langle\bar{\alpha}_y|\otimes\hat{\rho}^{\nu}_{\mathrm{II}}(\tau)\,\mathcal{U}^{\dagger}_{\mathrm{probe}}\right)\,, \tag{5.5}$$

where we indicate with I and II the photon and the phonon subsystem respectively. The quantum state of the emitted field is exactly what is measured in the experiment through the reconstruction of the Wigner function for different pump-probe time delays.

Once calculated the expression for the quantum state of the light pulses scattered by the phonon, $\hat{\rho}_{\mathrm{I}}(\tau)$, the expectation values of the significant observables can be computed. In particular we report here the expressions for the expectation values of the optical field quadrature operator in (5.1) and of the corresponding variance in terms of the time dependent phonon correlation functions $\langle(\hat{b}^{\dagger})^m(\hat{b})^n\rangle_{\tau}$:

$$\begin{aligned}\langle\hat{x}_{\Phi}\rangle(\tau) = \frac{1}{\sqrt{2}}\Big[\quad & 2\sqrt{I_y}\,\cos(\Phi+\theta'-\theta_y)\,\cos(\|\bar{\alpha}'\|)\\ & -i\Big(e^{-i\Phi}\,\langle\hat{b}\rangle_{\tau} - e^{i\Phi}\,\langle\hat{b}^{\dagger}\rangle_{\tau}\Big)\sin(\|\bar{\alpha}'\|)\Big]\,,\end{aligned} \tag{5.6}$$

$$\begin{aligned}\sigma^2_{\hat{x}_{\Phi}}(\tau) = \frac{1}{2} - \frac{\sin^2(\|\bar{\alpha}'\|)}{2}\Big[\quad & \left(\langle\hat{b}^2\rangle_{\tau} - \langle\hat{b}\rangle^2_{\tau}\right)e^{-2i\Phi} + \left(\langle(\hat{b}^{\dagger})^2\rangle_{\tau} - \langle\hat{b}^{\dagger}\rangle^2_{\tau}\right)e^{+2i\Phi}\\ & -2\left(\langle\hat{b}^{\dagger}\hat{b}\rangle_{\tau} - \langle\hat{b}^{\dagger}\rangle_{\tau}\,\langle\hat{b}\rangle_{\tau}\right)\Big]\,.\end{aligned} \tag{5.7}$$

By substituting the phase Φ with 0 or π one gets the predictions of the model for the position and momentum operator (equation (5.6)) and for their variances (equation (5.7)).

This allows to put in relation the photonic observables, which are directly measured in the experiment, with the phononic observables that are in this way indirectly explored. By substituting the explicit expressions for the time dependent phonon correlation functions $\langle(\hat{b}^{\dagger})^m(\hat{b})^n\rangle_{\tau}$ [15] it is possible to relate the expectation values of the phononic observables to the characteristics of the phonon quantum state, for example the phonon displacement parameter and the phonon squeezing parameter.

In particular, it is possible to show that the predicted quadrature variance in (5.7) presents an oscillating component at twice the phonon frequency (2Ω) only when the interaction Hamiltonian, which mimics the photo-excitation process, generates a squeezed phonon state. Moreover, in this condition, the position and momentum operator are predicted to oscillate at the phonon frequency together with the phase of the emitted field.

We stress that the work of comparison of the preliminary experimental results with the model prediction is still in progress. However, the indications in the experimental data of the presence of a 2Ω oscillating component in the quadrature variance (see Fig 5.13 and Fig 5.7) and of the Ω component in the position and momentum expectation values (Fig 5.17) and in the phase (Fig 5.8) are suggestive

of a meaningful description of the experiment through the proposed effective model. Further analysis are needed and work is in progress in this direction.

5.6 Conclusions

In this Chapter the preliminary results about the pump-probe quantum state tomography experiments have been reported. The technique has been tested by studying an impulsive stimulated Raman scattering process in a sample of quartz. In particular, the pump-probe polarization configuration has been chosen in order to excite the E symmetry Raman active mode in quartz at room temperature. In this configuration, the probe, interacting with the photo-excited material, gives rice to an emitted field scattered by the phonon with a linear polarization orthogonal to the probe one. The emitted field, after a polarization selection, is sent to a balanced homodyne detection apparatus in order to reconstruct its quantum state. The emitted field quantum state is reconstructed for each pump-probe delay time. In particular the Wigner function associated with the quantum state is retrieved.

The main information extracted from the time domain quantum state reconstruction is the presence of a oscillatory dynamics at the phonon frequency Ω not only in the expectation value of the number of photons, but also of the field quadratures, in particular of the position and momentum operators. We have access indeed not only on the amplitude of the emitted field (as in standard pump-probe experiments) but also to its phase. The preliminary experimental results show an oscillation of the emitted field phase at the frequency of the phonon.

Beyond to be a *phase-sensible* technique, pump probe quantum state tomography is overall a *quantum state-sensible* technique. In this respect, the preliminary experimental results suggest the presence of an oscillating component at the frequency 2Ω in the quadratures quantum fluctuations of the emitted field. This founding goes in the direction of the model predictions.

The effective fully quantum model presented in Section 2.7, forecasts indeed an oscillating response of the quadrature quantum noise of the emitted field at 2Ω. In particular, the model predicts such a behaviour for the emitted field provided that the vibration state it has interacted with has been photo-excited in a squeezed phonon state.

Concluding, even if the reported results are still preliminary and need to be deeper analyzed in the future, they represents a first step towards the investigation of the quantum proprieties of photo-excited phononic states in crystals through the measurement of the photon quantum state the probing pulses.

References

[1] Ed Hinds and Rainer Blatt. Nobel 2012 physics: Manipulating individual quantum systems. *Nature*, 496:55, 2012.

[2] Subir Sachdev. Quantum criticality: Competing ground states in low dimensions. *Science*, 288(5465):475–480, 2000. doi: 10.1126/science.288.5465.475.

[3] Shunsuke Nozawa, Toshiaki Iwazumi, and Hitoshi Osawa. Direct observation of the quantum fluctuation controlled by ultraviolet irradiation in $SrTio_3$. *Phys. Rev. B*, 72:121101, 2005. doi: 10.1103/PhysRevB.72.121101. URL http://link.aps.org/doi/10.1103/PhysRevB.72.121101.

[4] D. M. Newns and C. C. Tsuei. Fluctuating cu-o-cu bond model of high-temperature superconductivity. *Nature Physics*, 184(191):1745–2473, 2007.

[5] K. Hashimoto, K. Cho, T. Shibauchi, S. Kasahara, Y. Mizukami, R. Katsumata, Y. Tsuruhara, T. Terashima, H. Ikeda, M. A. Tanatar, H. Kitano, N. Salovich, R. W. Giannetta, P. Walmsley, A. Carrington, R. Prozorov, and Y. Matsuda. A sharp peak of the zero-temperature penetration depth at optimal composition in bafe2(as1x96xpx)2. *Science*, 336(6088):1554–1557, 2012. doi: 10.1126/science.1219821.

[6] C. Castellani, C. Di Castro, and M. Grilli. Non-fermi-liquid behavior and d-wave superconductivity near the charge-density-wave quantum critical point. *Zeitschrift fur Physik B Condensed Matter*, 103(2):137–144, 1996. doi: 10.1007/s002570050347. URL http://dx.doi.org/10.1007/s002570050347.

[7] K Alex Müller, W Berlinger, and E Tosatti. Indication for a novel phase in the quantum paraelectric regime of srtio3. *Zeitschrift für Physik B Condensed Matter*, 84(2):277–283, 1991.

[8] Meenehan S. M. MacCabe G. S. Groblacher S. Safavi-Naeini A. H. Marsili F. Shaw M. D. Cohen, J. D. and O. Painter. Phonon counting and intensity interferometry of a nanomechanical resonator. *Nature*, 520:522–525, 2015.

[9] F. Giusti. Quantum state tomography applied to time resolved spectroscopy, 2014. URL https://sites.google.com/site/danielefausti/educational-materials.

[10] Martina Esposito, Francesco Randi, Francesca Giusti, Davide Boschetto, Fulvio Parmigiani, and Daniele Fausti. Quantum optics for studying ultrafast

processes in condensed matter. *CLEO: 2015*, page FTu2B.2, 2015. doi: 10.1364/CLEO_QELS.2015.FTu2B.2. URL http://www.osapublishing.org/abstract.cfm?URI=CLEO_QELS-2015-FTu2B.2.

[11] Lvovsky and Raymer. Continuous-variable optical quantum-state tomography. *REVIEWS OF MODERN PHYSICS*, 81(1):299, January-March 2009.

[12] M Esposito, F Benatti, R Floreanini, S Olivares, F Randi, K Titimbo, M Pividori, F Novelli, F Cilento, F Parmigiani, and D Fausti. Pulsed homodyne gaussian quantum tomography with low detection efficiency. *New Journal of Physics*, 16(4):043004, 2014. URL http://stacks.iop.org/1367-2630/16/i=4/a=043004.

[13] Etchepare, GRILLON, CHAMBARET, HAMONIAUX, and ORSZAG. Polarization selectivity in time-resolved transient phase grating. *Optic. Comm.*, 63, 1987.

[14] M. Guta C. Butucea and L. Artiles. Minimax and adaptive estimation of the wigner function in quantum homodyne tomography with noisy data. *Ann. Stat.*, 35:465, 2007.

[15] Kelvin Titimbo. Creation and detection of squeezed phonons in pump and probe experiments: A fully quantum treatment, 2015.

6

Conclusions and perspectives

The research presented in this thesis places in between the fields of solid state physics and quantum optics. In detail, we propose a new approach to access the quantum fluctuations of the atomic positions in solids.

The scientific motivation that drives our research is to develop a unique tool to study the microscopic quantum mechanisms at the basis of intriguing macroscopic material proprieties, like for example quantum para-electricity, charge density waves, or high temperature superconductivity. In these systems it has been shown that the quantum nature of collective excitations, like lattice atomic vibrations, may be the key player in determining the onset of the exotic phenomena observed [1,2]. It is in this perspective that the new tool which is used here to measure directly the fluctuations on a simple material may become a fundamental tool to understand the microscopic origin of exotic macroscopic proprieties (Chapter 1).

The leading idea of this project is to address the quantum state of collective atomic vibrational excitation in solids through the measurement of the quantum state of ultrashort light pulses subsequently to their interaction with the material.

In order to prepare and probe vibrational states in crystals we exploit optical ultrafast spectroscopy techniques. In this kind of experiments an intense pump laser pulse drives a collective atomic excitation in the crystal and a less intense probe laser pulse interacts with the system out-of-equilibrium. Standard pump-probe techniques measure the intensity of the output probe, providing information in real time about the average of the atomic positions during the collective excitation. However, in this kind of experiments one has no chances to directly measure the quantum fluctuations of the atomic positions around their average. In this thesis we propose a new spectroscopic approach to fill this gap.

We developed two experimental schemes that allow for the measurement of (i) the photon number quantum statistics and (ii) the quantum state reconstruction

of the probe pulses in a pump-probe setup. Moreover, in order to predict how the fluctuations of the atomic positions in a lattice can be mapped onto the photon quantum fluctuations of the probe field, we propose a fully quantum theoretical approach to time domain studies (Chapter 2).

In order to characterize from the quantum mechanical point of view the light pulses after the interaction with the material, we adopted a well known technique in quantum optics, that is optical homodyne tomography (Chapter 3).

Our approach has been tested by investigating quantum fluctuations of the atomic positions in α-quartz, which serves as a case study for transparent materials. In particular, the quantum proprieties of photo-excited phonon states in quartz have been investigated by both the photon number quantum statistics (Chapter 4) and pump-probe quantum state tomography (Chapter 5).
In the first case (Chapter 4), our novel experimental approach allows for the direct measurement of the photon number quantum fluctuations of the probing light in the shot-noise regime. The comparison of the experimental results with the predictions of the model allows us to unveil non classical vibrational states (squeezed states) produced by photo-excitation.
In the second case (Chapter 5), the experiment allows not only to investigate the photon number quantum distribution, but also to have access to the maximum information about the scattered probing light, *i. e.* its quantum state, which is completely characterized in the time domain. Chapter 5 should be seen as a report of some preliminary results demonstrating that quantum state reconstruction in time domain experiments is feasible. The data analysis is representative of a summary of a work in progress.

We stress once more that this thesis had the main aim to test the proposed approach by studying simple materials and simple excitations. However, our approach can be in principle generalized to the study of any collective excitation both in simple and in complex systems.

There are indeed imminent steps in the perspectives of the project.

- The addition of a second pump pulse in the experimental set up. The idea is to configure the second pump in order to excite the phononic mode in anti-phase with the respect to the first photo-excitation. This will in principle repress the average atomic oscillation allowing the study of the intrinsic atomic quantum fluctuations without the artifacts due to the average displacements.

- The application of our experimental approach to study atomic quantum fluctuations in systems where they are particulary relevant for some material proprieties as quantum para-electricity in systems like $SrTiO_3$. In this material indeed the quantum fluctuations of Ti atoms along the $Ti-O$ direction are strictly connected to the anomalous behaviour of the dielectric susceptibility in the quantum para-electric phase (Section 1.2). The characterization of the quantum state of such vibrational states could be of great interest in a deeper comprehension of the quantum para-electricity phenomena.

Further, we stress that the techniques is applicable to any excitation obeying Raman selection rules. This open the new avenue, which will be explored in the

near future, of studying by this techniques fluctuations of electronic origin such as superconducting gaps[3].

References

[1] Berlinger W. Müller, K. A. and E. Tosatti. Indication for a novel phase in the quantum paraelectric regime of $SrTiO_3$. *Z. Phys. B: Condens. Matter*, 84: 277–283, 1991.

[2] Gil Refael Ivar Martin Michael Knap, Mehrtash Babadi and Eugene Demler. Dynamical cooper pairing in non-equilibrium electron-phonon systems. 2015. URL http://arxiv.org/abs/1511.07874.

[3] Thomas P. Devereaux and Rudi Hackl. Inelastic light scattering from correlated electrons. *Rev. Mod. Phys.*, 79:175–233, Jan 2007. doi: 10.1103/RevModPhys.79.175. URL http://link.aps.org/doi/10.1103/RevModPhys.79.175.

A

Low noise acquisition - detection system

In this appendix we present the characteristics of the detection-acquisition system realized and improved in the course of the whole PhD period and adopted for the experiments presented both in Chapter 4 and in Chapter 5.

We substantially improved the detection system presented in section 3.4.1 by designing and realizing a custom highly efficient differential detector. The latter is adapted to detect laser pulses generated by a 250 kHz mode-locked amplified Ti:Sapphire system*. A block representation of the complete laser system used in our experiments is given in Fig A.1. We also made faster the acquisition system by

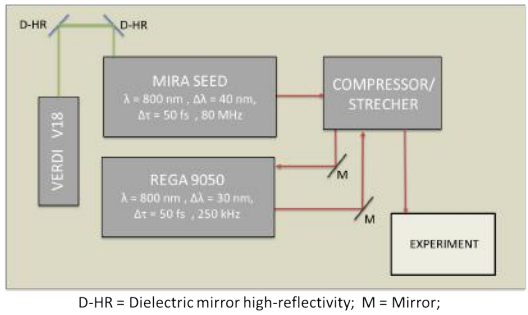

Figure A.1: Block diagram of the laser sources system.

*While for the homodyne detection experiments in section 3.4.1 we used a laser source composed of only an oscillator (Fig 3.3), for the composite experiments reported in in Chapter 4 and in Chapter 5 (pump-probe and homodyne detection combined experiments) an amplified laser source is needed.

substituting the oscilloscope in Fig 3.5 with high speed digitizer PC plug-in card (*Spectrum* M3i.2132-exp) with 8 bit resolution and 1 GS/s sampling rate[1]. A block diagram of the acquisition system is shown in Fig A.2.

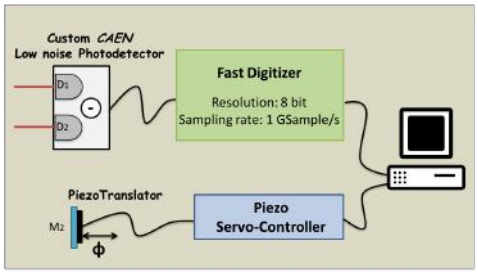

Figure A.2: Block diagram of the acquisition system

In the following we report the details of the custom differential photodetector.

A.1 Highly efficient time domain balanced homodyne detector

The custom differential photodetector has been realized in collaboration with the *CAEN* company and with the fundamental help of dr. Giovanni Franchi with whom it has been really a pleasure to work. This detector has been adopted for the experiments presented both in Chapter 4 and in Chapter 5.

The detector consists of two *Hamamatsu S3883* Silicon PIN photodiodes with 0.94 quantum efficiency at 800 nm connected in reverse bias and followed by a low-noise charge amplifier. The photo-currents generated by the two photodiodes in response to a single optical pulse impinging on them are physically subtracted and the resulting charge is amplified using *CAEN* custom designed electronic components. The preamplifier sensitivity is 5.2 mV/fC with a linear response up to about 2 V of pulse peak voltage. The output voltage of the photodetector for each single pulse is digitize at 1 GS/s, the sampling rate of the *Spectrum* digitizer.

The first test we performed on the photodetector is to verify the linear response of the two photodiodes. In order to do this we block the entrance of one of the diodes per time and we acquire several consecutive pulses. Note that we use the convention of expressing the voltage acquired for every single differential pulse, V_i, as the sum of the voltages digitized for 500 points at 1 GS/s (pulse integral). For reference, the digitized measurement of a pulse with a 1 V voltage peak ($V_i^{\text{peak}} = 1\text{V}$) corresponds to a value of the pulse integral $V_i = 300$ V. We then repeat the procedure for different intensities of the local oscillator beam. The results are shown in Fig A.3. The pulse integral is shown as a function of the pulse peak displaying a linear behaviour. Each point is obtained averaging the values of $N = 2000$ subsequent pulses ($V_{\text{mean}} = \sum_i^N V_i$, $V_{\text{mean}}^{\text{peak}} = \sum_i^N V_i^{\text{peak}}$). Since the amplification specifics are known one can calculate how many photons for each pulse correspond to a

given voltage peak intensity. For reference, 1V of peak value correspond to about 1.38×10^6 photons per pulse on the single photodiode.

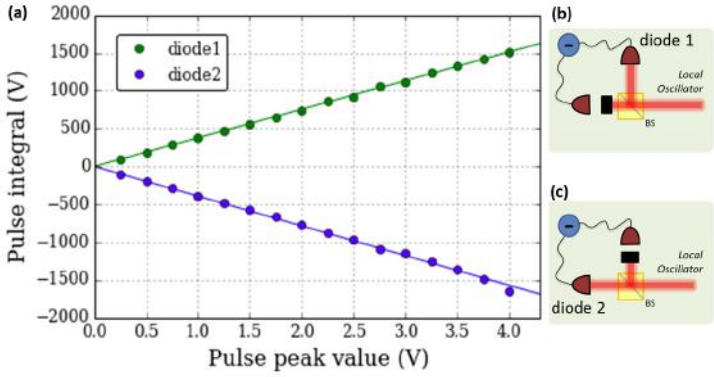

Figure A.3: Photodiodes linearity test. (a) Measured pulse integral vs pulse peak for the two photodiodes. in (b) and (c) the two experimental configurations are sketched.

Once verified the range of linearity of the photodiodes, we performed the shot-noise linearity test. In this case both the entrance of the photodiodes are open and the two input beams are perfectly balanced in order to have the difference signal averaged at zero voltage. The experimental configuration for such a test is reported in Fig A.4 (b). The results are shown in Fig A.4 (a).

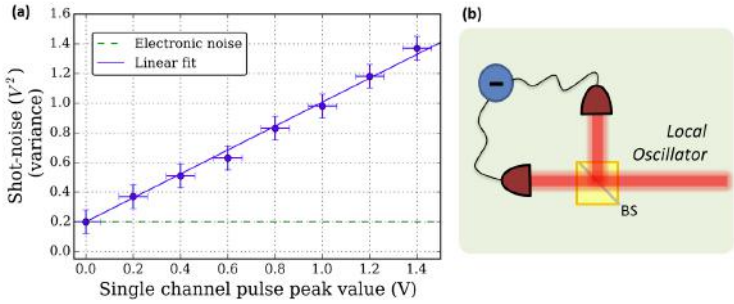

Figure A.4: Shot-noise linearity test. (a) Noise of 4000 consecutive pulses vs the average voltage peak value. (b) Sketch of the experimental configuration.

For each intensity of the local oscillator beam $N = 4000$ consecutive pulses are acquired and the variance of the pulse integrals is measured, $V_{\text{var}} = \sum_i^N (V_i - V_{\text{mean}})^2$, this corresponds to what we call homodyne detection noise. In order to distinguish the intrinsic quantum noise (shot-noise) from other classical noise contributions to the homodyne detection noise, we repeated the measurement for different intensities of the local oscillator. In Fig A.4 (a) the homodyne detection noise is reported versus the voltage peak absolute value detected if one of the

photodiode is obscured, the latter is proportional to the local oscillator intensity. The noise result linear with a constant offset representing the electronic noise. This behavior is characteristic of the shot-noise regime[2].

The detector shot-noise linearity test demonstrates that we are sensible to quantum fluctuations of the photon number. In particular, the shot-to-electronic noise ration at the maximum local oscillator intensity in the linear regime is approximately 8 *dB*. This correspond to an equivalent efficiency, defined in (3.35), $\eta_{\mathrm{eq}} \approx 0.85$. This result represents a relevant improvement with respect to the performance of the commercial photodetector used in the experiment reported in section 3.4.1, whose shot-to-electronic noise ratio was approximately 2 *dB*.

A.2 Detector noise characterization

In the experiments reported in Section 4.3 (shot-noise limited pump-probe experiments), we adopt a differential acquisition scheme where each probe pulse transmitted through the sample is referenced with a second pulse which has not interacted with the sample (see Fig 4.9). Adopting the notation of Section 4.3, the differential photo-voltage for a single pulse acquisition is indicated with ΔT_i. In this case, the shot-noise characterization test consists in the measurement of the variance ΔT_{var} of 4000 differential pulses for different powers of the probe. The shot-noise test as a function of the probe power is shown in Fig A.5.

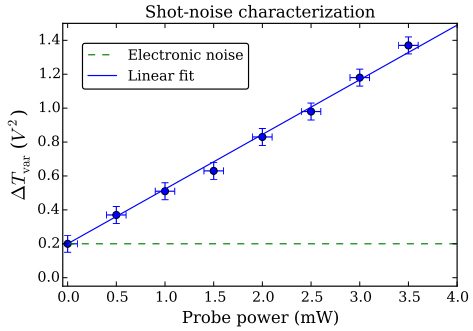

Figure A.5: Shot-noise characterization of the detection apparatus in Fig 4.9. Variance of 4000 acquired differential pulses as a function of the probe power. The vertical error bars indicate the standard deviation over 10 repeated measurements, the horizontal error bars indicate the instrumental error of the power-meter[3].

For the experiments in Section 4.3 we chose a probe power within the linearity interval (2.5 mW on the sample). Note that this corresponds roughly to 10^6 photons per pulse scattered in cross polarization on the detector (see Fig 4.9).

In the following we report two further characterization measurements performed in order to select a work configuration in which classical noise sources are negligible allowing for the measurement of the intrinsic optical shot noise.

- The first characterization consists in the measure of the variance, ΔT_{var}, in absence of the pump, as a function of the number of acquired pulses. The results are shown in Fig A.6. We observe that the variance increases when

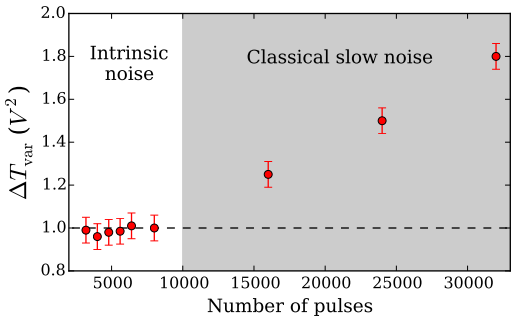

Figure A.6: Noise characterization as a function of the number of acquired pulses. Variance, ΔT_{var}, in absence of the pump, as a function of the number of acquired successive pulses. The dashed line indicates the shot-noise level. The grey area represents the region in which classical slow noise sources contributes to the variance. The error bars indicate the standard deviation over 10 repeated measurements[3].

the number of acquired successive pulses increases, this means that for long acquisitions a slow noise contribution makes higher the measured variance (grey area in Fig A.6). Thus, we chose to acquire $N = 4000$ successive pulses per step in order to guarantee the statistical meaningfulness of the data but at the same time avoiding contributions of classical slow noises. Note that the time to time noise in the mean number of photons reported in the main text is larger than the value of the variance. This is explained by considering that the fluctuations in the mean values are made large by slow noise of classical nature (the differences between the measurements scan by scan). On the contrary the variance is dominated by intrinsic fluctuations and, as discussed in the main text, it is calculated for every scan separately and then averaged. The results reported in Supplementary Fig A.6 show that acquiring up to about 10^4 pulses guarantees that classical slow noise contributions are excluded.

- Moreover we measured the obtained variance ΔT_{var} for a fixed number of pulses ($N = 800$) in absence of the pump as a function of the unbalance between the transmitted probe pulse and the reference pulse, that is as a function of the acquired mean voltage ΔT_{mean}. The results of such characterization measurement are shown in Fig A.7. One can notice that the noise randomly fluctuates in a range of minimal values (grey area) for small positive or negative unbalance (yellow area). For larger unbalance the noise starts to increase due to artifacts in the amplification process. All the time domain experiments reported here have been performed within the region of small detector unbalancing (green area) in order to be sure of working in shot noise limited conditions.

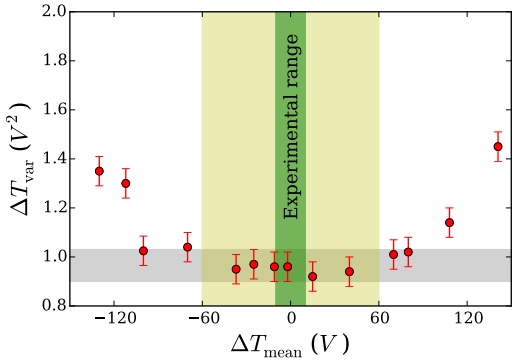

Figure A.7: Noise characterization as a function of the unbalance. Variance, ΔT_{var}, in absence of the pump for a fixed number of pulses ($N = 800$), as a function of the unbalance between the transmitted probe pulse and the reference pulse, expressed as acquired mean voltage ΔT_{mean}. Grey area: range of minimal noise; yellow area: unbalance region in which the noise randomly fluctuates in a range of minimal values; green area: unbalance region in which the experiments have been performed. Notice that we use the convention of expressing the voltage acquired for every single pulse acquisition as the sum of the voltages digitized for 500 points at 1 GS s^{-1}. For reference, the digitized measurement of a differential pulse with a 1 V (-1 V) voltage peak corresponds to a value of 300 V (-300 V). The error bars indicate the standard deviation over 10 repeated measurements[3].

References

[1] F. Randi. Pulsed homodyne detection for quantum state reconstruction applied to ultrafast non-equilibrium spectroscopy, 2013. URL https://sites.google.com/site/danielefausti/educational-materials.

[2] Hans A. Bachor and Timothy C. Ralph. *A Guide to experiments in Quantum Optics*. WILEY-VCH, 2004.

[3] M. Esposito, K. Titimbo, K. Zimmermann, F. Giusti, F. Randi, D. Boschetto, F. Parmigiani, R. Floreanini, F. Benatti, and Fausti D. Photon number statisctics uncover the fluctuations in non-equilibrium lattice dynamics. *Nature Communication*, 6(10249). doi: 10.1038/ncomms10249. URL http://dx.doi.org/10.1038/ncomms10249.

B

Wigner function reconstruction error

In this appendix we report the derivation of an upper bound to the mean square error of the reconstructed Wigner function in equation (3.58) in Section 3.5.

B.1 Upper bound error derivation

This analysis is necessary in order to find an optimal functional relation between the free parameters in the reconstruction algorithm such to minimise the reconstruction error. For this purpose we follow the techniques developed in[1] adapting them to the case on a linear superposition of coherent states. Using (3.29) and (3.31), one starts by rewriting the error in (3.32) as the sum of three contributions:

$$\Delta^{\eta,r}_{h,n}(\hat{\rho}) = \int_{C_r(0)} \mathrm{d}q\mathrm{d}p \left(E\left[\left| W^{\eta}_{h,n}(q,p) \right|^2 \right] - \left| E\left[W^{\eta}_{h,n}(q,p) \right] \right|^2 \right) \tag{B.1}$$

$$+ \int_{C^c_r(0)} \mathrm{d}q\mathrm{d}p \, |W_\rho(q,p)|^2 \tag{B.2}$$

$$+ \int_{C_r(0)} \mathrm{d}q\mathrm{d}p \left| E\left[W^{\eta}_{h,n}(q,p) \right] - W_\rho(q,p) \right|^2, \tag{B.3}$$

$C^c_r(0)$ denoting the region outside the circle $C_r(0)$, where $q^2 + p^2 > r^2$. The first and the third term correspond to the variance and bias of the reconstructed Wigner function respectively, while the second term is the error due to restricting the reconstruction to the circle $C_r(0)$.
Given a density matrix $\hat{\rho}$, the second term can be directly calculated. This is true also of the bias; indeed, because of the hypothesis that the pairs (X_ℓ, Φ_ℓ) are

independent identically distributed stochastic variables, it turns out that

$$\begin{aligned} E\left[W^{\eta}_{h,n}(q,p)\right] &= \frac{1}{\pi\, n}\sum_{\ell=1}^{n} E\left[K^{\eta}_{h}\left([(q,p);\Phi_{\ell}]-\frac{X_{\ell}}{\sqrt{\eta}}\right)\right] \\ &= \frac{1}{\pi}\, E\left[K^{\eta}_{h}\left([(q,p);\Phi]-\frac{X}{\sqrt{\eta}}\right)\right] \\ &= \int_{0}^{\pi}\mathrm{d}\phi\int_{-1/h}^{1/h}\mathrm{d}\xi\,\frac{|\xi|}{(2\pi)^2}\int_{-\infty}^{+\infty}\mathrm{d}x\,\mathrm{e}^{i\xi(q\cos\phi+p\sin\phi-x/\sqrt{\eta})}\,\mathrm{e}^{\gamma\xi^2}\,p_{\rho}(x,\phi) \end{aligned} \tag{B.4}$$

differs from the true Wigner function $W_{\rho}(q,p)$ in (3.28) by the integration over ξ being restricted to the interval $[-1/h, 1/h]$. Moreover, its Fourier transform reads

$$\begin{aligned} F\left[E\left[W^{\eta}_{h,n}\right]\right](w) &= \int_{-\infty}^{+\infty}\mathrm{d}q\int_{-\infty}^{+\infty}\mathrm{d}p\,\mathrm{e}^{-i(qw_1+pw_2)}\,E\left[W^{\eta}_{h,n}(q,p)\right] \\ &= \chi_{[-1/h,1/h]}(\|w\|)\,F\left[W_{\rho}\right](w), \quad w=(w_1,w_2)\,, \end{aligned} \tag{B.5}$$

where $\chi_{[-1/h,1/h]}(\|w\|)$ is the characteristic function of the interval $[-1/h, 1/h]$. Then, by means of Plancherel equality, one gets

$$\begin{aligned} &\int_{C_r(0)}\mathrm{d}q\mathrm{d}p\,\left|E\left[W^{\eta}_{h,n}(q,p)\right]-W_{\rho}(q,p)\right|^2 \leq \\ &\int_{\mathbb{R}^2}\mathrm{d}q\mathrm{d}p\,\left|E\left[W^{\eta}_{h,n}(q,p)\right]-W_{\rho}(q,p)\right|^2, \end{aligned} \tag{B.6}$$

where the second term in the inequality can be expressed as follows

$$\begin{aligned} \left\|E\left[W^{\eta}_{h,n}\right]-W_{\rho}\right\|_2^2 &= \frac{1}{4\pi^2}\left\|F\left[E\left[W^{\eta}_{h,n}\right]\right]-F\left[W_{\rho}\right]\right\|_2^2 \\ &= \frac{1}{4\pi^2}\left\|F\left[W_{\rho}\right]\,\chi_{[-1/h,1/h]}-F\left[W_{\rho}\right]\right\|_2^2 \\ &= \frac{1}{4\pi^2}\int_{\|w\|\geq 1/h}\mathrm{d}w\,\left|F\left[W_{\rho}\right](w)\right|^2. \end{aligned} \tag{B.7}$$

The variance contribution can be estimated as follows: firstly, by using (3.29) and (3.31), one recasts it as

$$\begin{aligned} &\int_{C_r(0)}\mathrm{d}q\mathrm{d}p\,\left(E\left[\left|W^{\eta}_{h,n}(q,p)\right|^2\right]-\left|E\left[W^{\eta}_{h,n}(q,p)\right]\right|^2\right)= \\ &\quad=\frac{1}{\pi^2\, n}\left\{E\left[\left\|K^{\eta}_{h}\left([\,(q,p)\,;\Phi]-\frac{X}{\sqrt{\eta}}\right)\,\chi_r(q,p)\right\|^2\right]+\right. \\ &\quad\quad\left.-\left\|E\left[K^{\eta}_{h}\left([\,(q,p)\,;\Phi]-\frac{X}{\sqrt{\eta}}\right)\,\chi_r(q,p)\right]\right\|^2\right\}. \end{aligned} \tag{B.8}$$

Then, a direct computation of the first contribution yields the upper bound

$$E\left[\left\|K_h^\eta\left(\left[\,(q,p)\,;\Phi\right]-\frac{X}{\sqrt{\eta}}\right)\,\chi_r(q,p)\right\|^2\right] \;\leq\; \sqrt{\frac{\pi}{\gamma}}\,\frac{r^2}{16\,h}\,\mathrm{e}^{\frac{2\gamma}{h^2}}\,(1+o(1))\;,$$
$$\gamma \;=\; \frac{1-\eta}{4\eta}\;, \tag{B.9}$$

with $o(1)$ denoting a quantity which vanishes as h when $h\to 0$. On the other hand, the second contribution can be estimated by extending the integration over the whole plane $(q,p)\in\mathbb{R}^2$ and using (B.5):

$$\left\|E\left[K_h^\eta\left(\left[\,(q,p)\,;\Phi\right]-\frac{X}{\sqrt{\eta}}\right)\,\chi_r(q,p)\right]\right\|^2 \leq \frac{1}{4\pi^2}\left\|F\left[W_\rho\right]\right\|^2=\left\|W_\rho\right\|^2\leq\frac{1}{2\pi}\;. \tag{B.10}$$

Let us consider now the specific case of $\hat\rho=\hat\rho_\alpha$, the superposition of coherent states defined in (3.52). The auxiliary parameter β labelling the class of density matrices $\mathcal{A}_{\beta,s,L}$ in (3.33) with $s=2$ can be used to further optimize the reconstruction error $\Delta_{h,n}^{\eta,r}(\hat\rho_\alpha)$. In particular, since $\left|\sum_{j=1}^M z_j\right|^2\leq M\,\sum_{j=1}^M|z_j|^2$, we get the upper bounds

$$|W_\alpha(q,p)| \;\leq\; \frac{2}{\pi},\qquad \left|F\left[W_\alpha\right](w_1,w_2)\right|\leq 2 \tag{B.11}$$

$$|W_\alpha(q,p)|^2 \;\leq\; \frac{3}{4\pi^2}\left(\mathrm{e}^{-2(q-\sqrt{2}\alpha_1)^2-2(p-\sqrt{2}\alpha_2)^2}+\mathrm{e}^{-2(q+\sqrt{2}\alpha_1)^2-2(p+\sqrt{2}\alpha_2)^2}\right.$$
$$\left.+4\,\mathrm{e}^{-2(q^2+p^2)}\right)\leq\frac{3}{2\pi^2}\left(\mathrm{e}^{-(\sqrt{2}R-|\alpha|)^2}+2\mathrm{e}^{-2R^2}\right) \tag{B.12}$$

$$\left|F\left[W_\alpha\right](w_1,w_2)\right|^2 \;\leq\; \frac{3}{4}\left(\mathrm{e}^{-\frac{(w_1+2\sqrt{2}\alpha_2)^2+(w_2-2\sqrt{2}\alpha_1)^2)}{2}}+\mathrm{e}^{-\frac{(w_1-2\sqrt{2}\alpha_2)^2+(w_2+2\sqrt{2}\alpha_1)^2)}{2}}\right.$$
$$\left.+4\,\mathrm{e}^{-\frac{w_1^2+w_2^2}{2}}\right)\leq\frac{3}{2}\left(\mathrm{e}^{-(R/\sqrt{2}-2|\alpha|)^2}+2\mathrm{e}^{-R^2/2}\right)\;, \tag{B.13}$$

where $R^2=q^2+p^2$ in (B.12) and $R^2=w_1^2+w_2^2$ in (B.13) . Then, one derives the upper bounds

$$\int_{\mathbb{R}^2}\mathrm{d}q\mathrm{d}p\,|W_\alpha(q,p)|^2\;\mathrm{e}^{2\beta(q^2+p^2)}$$
$$\leq\frac{3\left(1+\mathrm{e}^{4\beta|\alpha|^2/(1-\beta)}\left(1+\frac{2\sqrt{\pi}|\alpha|}{\sqrt{1-\beta}}-\mathrm{e}^{-4|\alpha|^2/(1-\beta)}\right)\right)}{2\pi(1-\beta)} \tag{B.14}$$

$$\int_{\mathbb{R}^2}\mathrm{d}w_1\mathrm{d}w_2\,\left|F\left[W_\alpha\right](w_1,w_2)\right|^2\;\mathrm{e}^{2\beta(w_1^2+w_2^2)}$$
$$\leq\frac{6\pi\left(1+\mathrm{e}^{16\beta|\alpha|^2/(1-4\beta)}\left(1+\frac{2\sqrt{\pi}|\alpha|}{\sqrt{1-4\beta}}-\mathrm{e}^{-4|\alpha|^2/(1-4\beta)}\right)\right)}{1-4\beta} \tag{B.15}$$

which simultaneously hold for $0 < \beta < 1/4$.

Then, by means of the Cauchy-Schwartz inequality, one can estimate the contribution (B.2) to the error,

$$\begin{aligned}
&\int_{C_r^c(0)} \mathrm{d}q\mathrm{d}p \; |W_\alpha(q,p)|^2 = \int_{\mathbb{R}^2} \mathrm{d}q\mathrm{d}p \; |W_\alpha(q,p)|^2 \; \mathrm{e}^{\beta(q^2+p^2)} \, \mathrm{e}^{-\beta(q^2+p^2)} \, \Theta(q^2+p^2-r^2) \\
&\leq \sqrt{\int_{\mathbb{R}^2} \mathrm{d}q\mathrm{d}p \; |W_\alpha(q,p)|^2 \; \mathrm{e}^{2\beta(q^2+p^2)}} \sqrt{\int_{\mathbb{R}^2} \mathrm{d}q\mathrm{d}p \; |W_\alpha(q,p)|^2 \; \mathrm{e}^{-2\beta(q^2+p^2)} \, \Theta(q^2+p^2-r^2)} \\
&\leq \mathrm{e}^{-\beta\, r^2} \, \Delta_2(\beta) \,, \qquad \text{(B.16)}
\end{aligned}$$

and similary for (B.7),

$$\frac{1}{4\pi^2} \int_{\|w\| \geq 1/h} \mathrm{d}w_1 \mathrm{d}w_2 \; |F\left[W_\alpha\right](w_1,w_2)|^2 \leq \mathrm{e}^{-\beta/h^2} \, \Delta_3(h) \;, \qquad \text{(B.17)}$$

where $\Theta(x) = 0$ if $x \leq 0$, $\Theta(x) = 1$ otherwise, and

$$\Delta_2(\beta) = \sqrt{\frac{3\left(1 + \mathrm{e}^{4\beta|\alpha|^2/(1-\beta)}\left(1 + \frac{2\sqrt{\pi}|\alpha|}{\sqrt{1-\beta}} - \mathrm{e}^{-4|\alpha|^2/(1-\beta)}\right)\right)}{4\pi^2\pi(1-\beta)}} \qquad \text{(B.18)}$$

$$\Delta_3(\beta) = \sqrt{\frac{3\left(1 + \mathrm{e}^{16\beta|\alpha|^2/(1-4\beta)}\left(1 + \frac{2\sqrt{\pi}|\alpha|}{\sqrt{1-4\beta}} - \mathrm{e}^{-4|\alpha|^2/(1-4\beta)}\right)\right)}{4\pi^2\pi(1-4\beta)}} \,. \qquad \text{(B.19)}$$

Altogether, the previous estimates provide the following upper bound to the mean square error in (B.1)-(B.3):

$$\Delta_{h,n}^{\eta,r}(\hat{\rho}_\alpha) \leq \Delta \,, \qquad \Delta = \frac{r^2}{n\,h} \, \mathrm{e}^{2\gamma/h^2} \, \Delta_1(\gamma) + \mathrm{e}^{-\beta r^2} \, \Delta_2(\beta) + \mathrm{e}^{-\beta/h^2} \, \Delta_3(\beta) \,, \qquad \text{(B.20)}$$

where $\Delta_{1,2,3}$ do not depend on h, r and n and $\Delta_1(\gamma) = \sqrt{\pi}/(16\pi^2\sqrt{\gamma})$ is the leading order term in (B.9). By setting the derivatives with respect r and h of the right hand side equal to 0, one finds

$$\frac{2\gamma}{h^2} + \beta r^2 = \log n \, + \, \log\left(\beta h \frac{\Delta_2(\beta)}{\Delta_1(\gamma)}\right) \qquad \text{(B.21)}$$

$$\frac{2\gamma+\beta}{h^2} = \log n \, + \, \log\left(\frac{2\beta h}{r^2(h^2+4\gamma)} \frac{\Delta_3(\beta)}{\Delta_1(\gamma)}\right) \,. \qquad \text{(B.22)}$$

Whenever β is such that the arguments of the logarithms are much smaller than the number of data n, to leading order in n the upper bound to the mean square deviation is minimised by

$$r = \frac{1}{h} = \sqrt{\frac{\log n}{\beta + 2\gamma}} \,. \qquad \text{(B.23)}$$

The range of possible values of β is $0 \leq \beta \leq 1/4$: however, the upper bound Δ

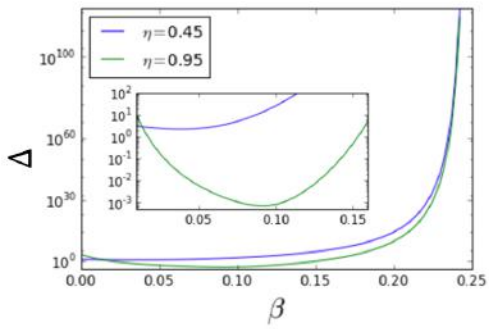

Figure B.1: Upper bound reconstruction error Δ as a function of the parameter β. Two efficiencies η are considered.

becomes loose when $\beta \to 1/4$ and $\beta \to 0$. In the first case, it is the quantity $\Delta_3(\beta)$ which diverges, in the second one, it is the variance contribution which diverges as the logarithm of the number of data. It thus follows that the range of values $\beta \in [\beta_0, \beta_1]$ where the numerical errors $\Delta_{h,n}^{\eta,r}(\hat{\rho}_\alpha)$ are comparable with their upper bounds Δ is roughly between $\beta_0 = 0.04$ and $\beta_1 = 0.10$ for $\eta = 0.45$ as indicated in Fig B.1.

References

[1] C. Butucea J.-M. Aubry and K. Meziani. State estimation in quantum homodyne tomography with noisy data. *Inv. Problems*, 25:015003, 2009.

List of publications

- "Pulsed homodyne Gaussian quantum tomography with low detection efficiency"

  Martina Esposito, Fabio Benatti, Roberto Floreanini, Stefano Olivares, Francesco Randi, Kelvin Titimbo, Marco Pividori, Fabio Novelli, Federico Cilento, Fulvio Parmigiani, and Daniele Fausti

  New Journal of Physics, **16**, 043004 (2014)

  Published 7 April 2014

  http://stacks.iop.org/1367-2630/16/i=4/a=043004

- "Photon number statisctics uncover the fluctuations in non-equilibrium lattice dynamics"

  Martina Esposito, Kelvin Titimbo, Klaus Zimmermann, Francesca Giusti, Francesco Randi, Davide Boschetto, Fulvio Parmigiani, Roberto Floreanini, Fabio Benatti and Daniele Fausti

  Nature Communication, **6**, 10249 (2015)

  Published 22 Dec 2015

  http://dx.doi.org/10.1038/ncomms10249

- "Quantum Optics for Studying Ultrafast Processes in Condensed Matter"

  Martina Esposito, Francesco Randi, Francesca Giusti, Davide Boschetto, Fulvio Parmigiani and Daniele Fausti

  Conference paper, CLEO 2015, FTu2B.2

  San Jose (CA) USA, 12 May 2015

  http://www.osapublishing.org/abstract.cfm?URI=CLEO_QELS-2015-FTu2B.2

- "Quantum interferences reconstruction with low homodyne detection efficiency"

  Martina Esposito, Francesco Randi, Kelvin Titimbo, Klaus Zimmermann, Georgios Kourousias, Alessio Curri, Roberto Floreanini, Fulvio Parmigiani, Daniele Fausti and Fabio Benatti

  preprint 31 Aug 2015

  http://arxiv.org/abs/1508.07799